QuadWire: An extended one dimensional model for efficient mechanical simulations of bead-based additive manufacturing processes

Laurane Preumont, Rafaël Viano, Daniel Weisz-Patrault, Pierre Margerit, Grégoire Allaire

QuadWire: an extended one dimensional model for efficient mechanical simulations of bead-based additive manufacturing processes

Laurane Preumont[a], Rafaël Viano[a,b], Daniel Weisz-Patrault[a,*], Pierre Margerit[c], Grégoire Allaire[d]

[a]*LMS, CNRS, École Polytechnique, Institut Polytechnique de Paris, F-91128 Palaiseau, France*
[b]*Lab Navier, Univ Gustave Eiffel, ENPC, CNRS, F-77447 Marne la Vallée, France*
[c]*PIMM, CNRS, Arts et Métiers, F-75013 Paris, France*
[d]*CMAP, CNRS, École Polytechnique, Institut Polytechnique de Paris, F-91128 Palaiseau, France*

Abstract

This paper presents the basis of a new mechanical model named *QuadWire* dedicated to efficient simulations of bead-based additive manufacturing processes in which elongated beads undergoing significant cooling and eigenstrain are assembled to form 3D parts. The key contribution is to use a multi-particular approach containing 4 particles per material point to develop an extended 1D model capable of capturing complex 3D mechanical states, while significantly reducing computation time with respect to conventional approaches. Indeed, 3D models usually require at least 3 to 4 elements across the bead section, which results in fine discretization along the tangential direction to avoid conditioning issues, and therefore very fine mesh of the entire 3D part. In the *QuadWire* model, the bead height and thickness are internal dimensions, enabling a significantly coarser mesh along the tangential direction. Thus, although the *QuadWire* has 12 degrees of freedom per material point instead of 3 for classical models, the total number of degrees of freedom is reduced by several orders of magnitude for large parts. The proposed model is classically developed within the framework of the principle of virtual power and standard generalized hyperelastic media (i.e., finite strain theory), which necessitates a thermodynamic analysis. Furthermore, the proposed approach includes native and manageable kinematic constraints between successive beads so that the stress state properly evolves during fabrication. Finite element analysis is used for numerical implementation under infinitesimal strain assumption for the sake of simplicity, and the *QuadWire* stiffness parameters are optimized so that the mechanical response fit conventional 3D approaches. To validate and demonstrate the capabilities of the proposed strategy, the evolution of displacements and stresses in fused deposition modeling of polylactide is simulated.

Keywords: Additive Manufacturing ; Fast Thermo-Mechanical Analysis ; Model reduction ; Multi-particular Model ; *QuadWire* Model

*Corresponding author e-mail: daniel.weisz-patrault@cnrs.fr

1. Introduction

Additive Manufacturing (AM) encompasses the iterative fabrication of components by sequentially depositing various feedstock materials (e.g., polymers, metals, ceramics, and biomaterials) provided in the form of filaments, wires, powders, or liquids. These materials are shaped through processes including melting, binding, photo-polymerization, and extrusion. Some processes deal with complete layers at a time (e.g., vat photo-polymerization, sheet lamination, binder jetting, and material jetting), but the majority of processes rely on the deposition of successive beads. These bead-based additive manufacturing (BBAM) techniques encompass metal AM (e.g., Laser Powder Bed Fusion (LPBF) and Direct Energy Deposition (DED)), Stereolithography (SLA) and Fused Deposition Modeling (FDM) for polymers, as well as extrusion of concrete (3DCP) and clay. BBAM thus primarily involves the stacking of 1D elongated beads, placed adjacently, to ultimately form a complete 3D part with complex geometry.

To investigate the influence of process parameters on residual stresses and distortions, design of experiments methods are standard practice but are both costly and time-consuming [1]. Numerical simulations of various processes have therefore been developed over the past decade. Various physical phenomena arising during AM of different feedstock materials result in significant volume variation and/or deviatoric strain, leading to significant stresses and distortions. Thus, a considerable amount of studies has focused on modeling temperature kinetics [2], solid state phase transformations in metals [3], polymerization shrinkage in polymers [4], concrete shrinkage due to hydration or clay shrinkage due to water evaporation [5] that act as the most significant mechanical loads to consider. Indeed, such imposed strains, usually referred to as eigenstrains, appear as successive beads are kinematically constrained to one another during the fabrication process and are therefore responsible for kinematic incompatibilities resulting in progressive stress evolution. Thus, during fabrication, the accumulation of stress can lead to cracks, buckling, and other fabrication defects. Efficient simulations of the evolution of stresses during processes would therefore enable easier optimizations of process parameters and scanning strategies for each part geometry in order to reduce residual stresses and improve product quality.

However, the numerical simulation of mechanics in BBAM raises a major difficulty if parametric studies or optimization loops on the entire process are considered. Indeed, extensive computation costs are usually reported in the literature, as very large amounts of degrees of freedom (DoF) are necessary to model the 3D part at bead-scale using conventional approaches. Indeed, 3D finite element analysis (FEA) usually requires at least 3 to 4 elements across the bead section, resulting in fine discretization along the tangential direction to avoid conditioning issues, and therefore very fine mesh of the entire 3D part. For instance, among many other examples high-fidelity thermo-mechanical simulations have been developed for LPBF [6] and for DED [7] with restrictive computational cost. Therefore, even though some attempts to optimize scanning paths have been published (see. e.g., [8] including constraints on the maximum temperature, [9] including constraints on thermal stress, or [10] directly minimizing residual stresses and final deformation), optimization strategies remain limited due to high computation cost.

A key strategy to reduce computation time relies on decoupling mechanics from the computation of eigenstrains. Indeed, determining *eigenstrains* requires to solve the heat equation, phase transitions, and other physical phenomena with very fine time and space discretization, whereas

the computation of stresses and displacements can be carried out with much coarser time discretization at the part scale [11]. This decoupling enables to use specific and fast approaches for the eigenstrain computation relying on simplifying assumptions according to the studied process and material e.g., fast thermal and phase transition analysis has been proposed for DED (see. [2] for thermal analysis, and [3] for diffusional phase transition). The present work relies on this strategy, as temperature kinetics and other eigenstrains are assumed to be known from previous computations.

Nevertheless, the computation of mechanics alone (i.e., provided that eigenstrains are already known) is computationally costly as it necessitates to simulate the entire part since the overall geometry and boundary conditions play a major role. Of course, various attempts have been proposed to reduce computation time. Some approaches rely on meshing techniques [12], which include adaptive mesh refinement and parallelization [13], higher order discretization [14], and mortar approaches to deal with layer-wise non-matching meshes [15]. Fully 3D FEA can also be replaced by 2D FEA (see. [11] for a 2D computation validated by digital image correlation, and [16] for a 2D computation validated by X-ray synchrotron measurements), which is faster due to less DoF but only applies to thin-walled structures. Comprehensive 3D simulations have been used as basis to develop model reduction strategies within the framework of inherent strain method (ISM) which has emerged as a popular approach to attempt replacing fully 3D and computationally intensive numerical simulations, which take into account the detailed matter deposition history, by fast linear part-scale elastic simulations. The key feature of such approaches lies in the estimation, from a reference comprehensive computation, of a so-called *inherent strain* field, which is used as a mechanical loading in a simple part-scale elastic simulation to mimic the mechanical response of the reference computation [17]. Related methods include so-called applied plastic strains [18], mechanical layer equivalent method [19], or modified inherent strain method [20]. However, determining the appropriate inherent strain or shrinkage load to accurately capture the mechanical response of the fabricated component still requires that new reference computations be carried out for each set of tested process parameters. To avoid such issues, various techniques have been employed to determine inherent strains, including multiscale modeling [19], empirical methods [21]. Other attempts based on ISM include solution base reduction with proper generalized decomposition (PGD) approaches [22]. However, the reliability of ISM is not always guaranteed, so the inherent strain rate method (ISRM) is proposed as an alternative approach to offer improved accuracy, though significantly mitigating computation time reduction [23].

Nevertheless, previous model reduction strategies remain limited. In this paper, beads are modeled as extended 1D components, rather than employing conventional methods, which holds substantial potential for computation cost reduction while ensuring sufficiently detailed mechanical fields and satisfying accuracy. To achieve this goal, we adopt a multi-particular approach (see e.g., [24] for porous mechanics, and [25] for multilayer composites) to derive a new mechanical 1D model called *QuadWire* (where "quad" refers to 4 and "wire" to a 1D model). More precisely, 4 particles are assigned to each material point resulting in 4 displacement fields, hence 12 DoF per material point instead of 3 for conventional 3D models. Hence, within the framework of FEA, the bead height and thickness are internal dimensions of the proposed approach so that the mesh along the tangential direction can be much coarser than in 3D. Thus, although the extended model has more DoF per node than classical 3D models, the total number of DoF is reduced by several

orders of magnitude for large parts. Furthermore, this extended kinetics enables to define several generalized forces enabling to capture complex stress distributions arising in AM. In addition, unlike other classical 1D models such as the well-known Timoshenko beam theory, the model enables to easily assemble different beads together by imposing kinematics relations between them (see. figure 1) in order to obtain fully 3D printed parts.

A few comments should be added to compare the proposed model to the existing literature and justify the proposed approach. 1) One could think that within the framework of linear FEA, a *QuadWire* element is equivalent to a single 3D hexahedron element for a classical Cauchy model as both contain 24 DoF. But as already mentioned, unlike the conventional 3D model, the *QuadWire* model can be discretized without size constraint along its tangential direction as there are no conditioning issues. In addition, as shown in the following, the elastic behavior of the *QuadWire* model involves several stiffness tensors, which are sufficiently rich to satisfyingly capture the complex behavior of real beads, whereas a single hexahedron element poorly reproduces such a behavior. 2) Even though the *QuadWire* model is a first gradient theory with respect to the curvilinear abscissa of the bead, it corresponds to a third order gradient theory with respect to 3D representation. The main differences with classical higher order theories [26] is that (i) the gradient is defined as a proper derivative along the continuous curvilinear abscissa, and as discrete finite differences across the bead cross-section, and (ii) only a few components of higher order gradients naturally arises in the model derivation. 3) One could think that the number of particles is arbitrary. But in fact, the number of particles is a compromise between the level of detail and the number of DoF. Indeed, 4 particles enable us to impose 4 kinematic relations with neighboring beads (i.e., above, below, left and right) in order to bind the beads together and therefore consider fully 3D bodies. A higher number of particles would be possible but would involve more DoF. 4) Higher order continuum models, multi-particular models, and also enriched models in which each material point is defined as a material element that can be oriented or even deformed (e.g, Cosserat models, or deformable-section beam theory) are highly connected. As shown in the following, the proposed 4-particles model is similar to a 3D 3rd order model (with a single hexahedron elements over the bead width and height). But as already mentioned, 1D models present the advantage to allow using significantly coarser meshes along the tangential direction without conditioning issues. In addition, a general 3rd order 3D model would involve a very large number of generalized strain components as there are 3 components for the displacement field hence 9 for the 1st gradient, 27 for the 2nd gradient and 81 for the 3rd order gradient, leading to extensive behavior identification. On the opposite, only a few components of the 2nd and 3rd order gradients naturally arise in the derivation of the 4-particles model, which greatly facilitates the identification of the behavior and is sufficient to capture the complex behavior of the beads. The 4-particles strategy therefore appears to be a simple way of imposing minimal geometrical constraints to the model (in line with the need to easily connect each bead to its 4 neighbors i.e., top, bottom, left and right), and then applying a systematic method without assuming which components of the successive gradients should be neglected.

The paper is organized as follows. Theoretical foundations of the *QuadWire* model are detailed in Section 2. In particular, kinematics are defined and the power of internal forces and the consistency conditions are exploited to define generalized stresses. The virtual power principle is used as a weak form of the balance equation with boundary conditions. Thermodynamics analysis

is broached in Section 3 in order to derive the thermodynamics balance equation based on free energy and dissipated power. The material behavior is then derived within the framework of generalized standard media (GSM) [27, 28]. Even though many materials used in AM involve non-linear behavior, a thermo-hyperelastic behavior is derived in Section 4 within the framework of finite strain theory. In addition, numerical implementation has been performed under infinitesimal strain assumption for the sake of conciseness. Nevertheless, subsequent contributions will focus on specific non-linear behaviors according to different materials. An optimization procedure is then detailed in Section 5 in order to identify stiffness tensors to correctly capture the mechanical response of the actual bead. Moreover, a complete simulation in FDM of polylactide (PLA) is carried out to demonstrate the model capabilities in Section 6. Conclusive remarks are provided in Section 7.

2. *QuadWire* model theoretical foundations

Throughout the paper, tensors are denoted by bold symbols, while matrices are denoted by capital non-bold letters. In the following developments, since rate-independent behavior and quasi-static analysis are considered, time is omitted for the sake of clarity. However, a general formulation is derived through the principle of virtual power, involving generalized strain rates, and hence time derivatives. The time derivative of a function g is classically denoted by $\dot{g}$, while the derivation with respect to the curvilinear abscissa s of a function $g(s)$ is denoted by $g'(s)$.

2.1. Transformation gradient

The *QuadWire* model is derived within the general framework of finite strain theory. A unique deformed configuration denoted by $\mathcal{C}$ is classically defined. But strictly speaking, multi-particular models necessitate multiple reference configurations because several particles coincide at each material point of the deformed configuration, although they were at different locations before deformation. This is of course a major drawback because as many transformation mapping functions should be defined as there are particles. To avoid this issue, the model is derived under the assumption that the relative motion between particles is small, while the average response of the *QuadWire* is derived at finite strain. This means that the bead may be severely deformed as a line, while undergoing infinitesimal deformation of its cross-section. Therefore a single reference configuration $\mathcal{C}_0$ is defined as well as a single transformation mapping function. In addition, the bead thickness and height denoted by δn and δb defined in the reference configuration are also used in the deformed configuration.

The manifolds $\mathcal{C}_0$ and $\mathcal{C}$ immersed in $\mathbb{R}^3$ supporting the *QuadWire* model in the reference and deformed configurations respectively may be defined as the images of smooth mappings $s_0 \in [0, l_0] \mapsto \boldsymbol{X}(s_0) \in \mathcal{C}_0$ and $s \in [0, l] \mapsto \boldsymbol{x}(s) \in \mathcal{C}$ where s_0 and s are the curvilinear abscissas and where l_0 (m) and l (m) are the bead lengths in the reference and deformed configurations. The transformation mapping function is denoted by $s_0 \in [0, l_0] \mapsto \boldsymbol{\Phi}(s_0) = \boldsymbol{x}(s) \in \mathcal{C}$. Hence, the tangent unit vectors in the reference and deformed configurations are denoted by $\boldsymbol{t}_0(s_0)$ and $\boldsymbol{t}(s)$ and read:

$$\boldsymbol{t}_0(s_0) = \frac{\mathrm{d}\boldsymbol{X}(s_0)}{\mathrm{d}s_0} \quad \text{and} \quad \boldsymbol{t}(s) = \boldsymbol{x}'(s) \tag{1}$$

where the curvilinear abscissas s_0 and s are chosen so that the tangent vector has a unit norm. One can define a 2nd order rotation tensor $\boldsymbol{O}_0(s_0) \in \mathrm{SO}(3)$ such as:

$$\left\{ \begin{array}{l} \boldsymbol{t}_0(s_0) = \boldsymbol{O}_0(s_0).\boldsymbol{i} \\ \boldsymbol{n}_0(s_0) = \boldsymbol{O}_0(s_0).\boldsymbol{j} \\ \boldsymbol{b}_0(s_0) = \boldsymbol{O}_0(s_0).\boldsymbol{k} \end{array} \right. \tag{2}$$

where $\boldsymbol{i}, \boldsymbol{j}, \boldsymbol{k}$ is a fixed direct orthonormal coordinate system of $\mathbb{R}^3$ and $\boldsymbol{t}_0(s_0), \boldsymbol{n}_0(s_0), \boldsymbol{b}_0(s_0)$ is a local direct orthonormal coordinate system in the reference configuration. Given that there is no uniqueness of such a base, the direction $\boldsymbol{b}_0$ is aligned with the build direction (i.e., usually the vertical direction). The initial curvature of the domain is defined as an anti-symmetric second order tensor denoted by $\boldsymbol{\omega}_0(s) = \frac{\mathrm{d}\boldsymbol{O}_0(s_0)}{\mathrm{d}s_0}.\boldsymbol{O}_0{}^{\top}(s_0) \in \mathcal{T}_{\mathrm{A}}^2$ such that:

$$\frac{\mathrm{d}\boldsymbol{t}_0(s_0)}{\mathrm{d}s_0} = \boldsymbol{\omega}_0(s_0).\boldsymbol{t}_0(s_0) \;\Big|\; \frac{\mathrm{d}\boldsymbol{n}_0(s_0)}{\mathrm{d}s_0} = \boldsymbol{\omega}_0(s_0).\boldsymbol{n}_0(s_0) \;\Big|\; \frac{\mathrm{d}\boldsymbol{b}_0(s_0)}{\mathrm{d}s_0} = \boldsymbol{\omega}_0(s_0).\boldsymbol{b}_0(s_0) \tag{3}$$

where $\mathcal{T}_{\mathrm{A}}^2$ is the space of second order anti-symmetric tensors.

In addition to the transformation mapping $\boldsymbol{\Phi}$, an orientation mapping is defined as a rotation 2nd order tensor and denoted by $s_0 \in [0, l_0] \mapsto \boldsymbol{R}(s_0) \in \mathrm{SO}(3)$ such as:

$$\boldsymbol{t}(s) = \boldsymbol{R}(s_0).\boldsymbol{t}_0(s_0) \quad \text{and} \quad \boldsymbol{n}(s) = \boldsymbol{R}(s_0).\boldsymbol{n}_0(s_0) \quad \text{and} \quad \boldsymbol{b}(s) = \boldsymbol{R}(s_0).\boldsymbol{b}_0(s_0) \tag{4}$$

and where $\boldsymbol{t}(s), \boldsymbol{n}(s), \boldsymbol{b}(s)$ is a local direct orthonormal coordinate system in the deformed configuration. Consider the rotation 2nd order tensor $\boldsymbol{O}(s) = \boldsymbol{R}(s_0).\boldsymbol{O}_0(s_0) \in \mathrm{SO}(3)$ and the anti-symmetric 2nd order tensor $\boldsymbol{\omega}(s) = \boldsymbol{O}'(s).\boldsymbol{O}^{\top}(s) \in \mathcal{T}_{\mathrm{A}}^2$, hence:

$$\boldsymbol{t}'(s) = \boldsymbol{\omega}(s).\boldsymbol{t}(s) \;\big|\; \boldsymbol{n}'(s) = \boldsymbol{\omega}(s).\boldsymbol{n}(s) \;\big|\; \boldsymbol{b}'(s) = \boldsymbol{\omega}(s).\boldsymbol{b}(s) \tag{5}$$

Consider the gradient vector $\boldsymbol{G}(s_0)$ and its norm $J(s_0)$ defined by:

$$\boldsymbol{G}(s_0) = \frac{\mathrm{d}\boldsymbol{\Phi}(s_0)}{\mathrm{d}s_0} \quad \text{and} \quad J(s_0) = \sqrt{\boldsymbol{G}(s_0).\boldsymbol{G}(s_0)} \tag{6}$$

A simple differentiation gives:

$$\mathrm{d}s = J(s_0)\,\mathrm{d}s_0 \tag{7}$$

2.2. Kinetics

As mentioned in the introduction, a 4-particular model is derived, which means that 4 kinematic fields are assigned to each material point $\boldsymbol{x}(s)$ belonging to the domain $\mathcal{C}$ as depicted in figure 1. Thus, the space of generalized kinematically admissible motions reads:

$$\begin{array}{rl} \mathcal{V} = & \Big\{ \overrightarrow{\boldsymbol{v}} : s \mapsto (\boldsymbol{v}_1(s), \boldsymbol{v}_2(s), \boldsymbol{v}_3(s), \boldsymbol{v}_4(s)) \in \mathbb{R}^{12}, \\ & \forall k \in \{1,2,3,4\}\,,\ \forall s_k \in \mathcal{C}_k,\ \boldsymbol{v}_k(s_k) = \boldsymbol{v}_k^0(s_k) \Big\} \end{array} \tag{8}$$

where $\boldsymbol{v}_k^0$ are the imposed motions on known subsets $\mathcal{C}_k \subset \mathcal{C}$ (where $1 \leq k \leq 4$). Thus, the space of virtual motions reads:

$$\begin{aligned} \mathcal{V}^* = \; & \Big\{ \overrightarrow{\boldsymbol{v}}^* : s \mapsto (\boldsymbol{v}_1^*(s), \boldsymbol{v}_2^*(s), \boldsymbol{v}_3^*(s), \boldsymbol{v}_4^*(s)) \in \mathbb{R}^{12}, \\ & \forall k \in \{1,2,3,4\} \; \forall s_k \in \mathcal{C}_k, \; \boldsymbol{v}_k(s_k) = 0 \} \end{aligned} \tag{9}$$

each element of $\mathcal{V}^*$ contains 4 functions $(\boldsymbol{v}_1^*, \boldsymbol{v}_2^*, \boldsymbol{v}_3^*, \boldsymbol{v}_4^*)$ corresponding to the 4 particles. The main difference between the sets of generalized and virtual motions $\mathcal{V}$ and $\mathcal{V}^*$ is that kinematic boundary conditions are replaced by zero boundary conditions for the virtual motions in $\mathcal{V}^*$, as is usual for test functions which vanish on the boundary.

Rigid body motions involve a single anti-symmetric tensor for the 4 particles, which therefore move at different speeds but with the same rotation rate around the same point. This emphasizes the role of internal dimensions (i.e., bead thickness δn and height δb). The space of rigid body motions therefore reads:

$$\mathcal{V}_R^* = \Big\{ \overrightarrow{\boldsymbol{v}}^* \in \mathcal{V}^*, \; \exists \, \boldsymbol{v}_R^* \in \mathbb{R}^3, \; \exists \, \boldsymbol{\omega}^* \in \mathcal{T}_{\mathrm{A}}^2, \; \forall k \in \{1,2,3,4\} \, , \; \boldsymbol{v}_k^*(s) = \boldsymbol{v}_R^* + \boldsymbol{\omega}^* . \boldsymbol{x}_k(s) \Big\} \tag{10}$$

where the following local positions of the 4 particles denoted by $(\boldsymbol{x}_1(s), \boldsymbol{x}_2(s), \boldsymbol{x}_3(s), \boldsymbol{x}_4(s))$ have been considered:

$$\left\{ \begin{aligned} \boldsymbol{x}_1(s) &= \boldsymbol{x}(s) + \frac{\delta n}{2} \, \boldsymbol{n}(s) + \frac{\delta b}{2} \, \boldsymbol{b}(s) \\ \boldsymbol{x}_2(s) &= \boldsymbol{x}(s) + \frac{\delta n}{2} \, \boldsymbol{n}(s) - \frac{\delta b}{2} \, \boldsymbol{b}(s) \\ \boldsymbol{x}_3(s) &= \boldsymbol{x}(s) - \frac{\delta n}{2} \, \boldsymbol{n}(s) + \frac{\delta b}{2} \, \boldsymbol{b}(s) \\ \boldsymbol{x}_4(s) &= \boldsymbol{x}(s) - \frac{\delta n}{2} \, \boldsymbol{n}(s) - \frac{\delta b}{2} \, \boldsymbol{b}(s) \end{aligned} \right. \tag{11}$$

where δn and δb are defined in figure 1 as internal dimensions of the *QuadWire* model corresponding to the bead width and height respectively. Hence, the position $\boldsymbol{x}(s)$ of each material point reads as the average position of the 4 particles:

$$\boldsymbol{x}(s) = \frac{\boldsymbol{x}_1(s) + \boldsymbol{x}_2(s) + \boldsymbol{x}_3(s) + \boldsymbol{x}_4(s)}{4} \tag{12}$$

2.3. Generalized forces

Generalized forces are defined in the deformed configuration by introducing the virtual power of internal forces, which is defined as a linear form of $\overrightarrow{\boldsymbol{v}}^* = (\boldsymbol{v}_1^*, \boldsymbol{v}_2^*, \boldsymbol{v}_3^*, \boldsymbol{v}_4^*) \in \mathcal{V}^*$. The *QuadWire* model is derived at the first gradient with respect to s, thus:

$$\mathrm{PVI}(\overrightarrow{\boldsymbol{v}}^*) = \int_0^l \sum_{k=1}^{4} \left(\boldsymbol{f}_k(s) . \boldsymbol{v}_k^*(s) - \boldsymbol{F}_k(s) . \boldsymbol{v}_k^{*\prime}(s) \right) \mathrm{d}s \tag{13}$$

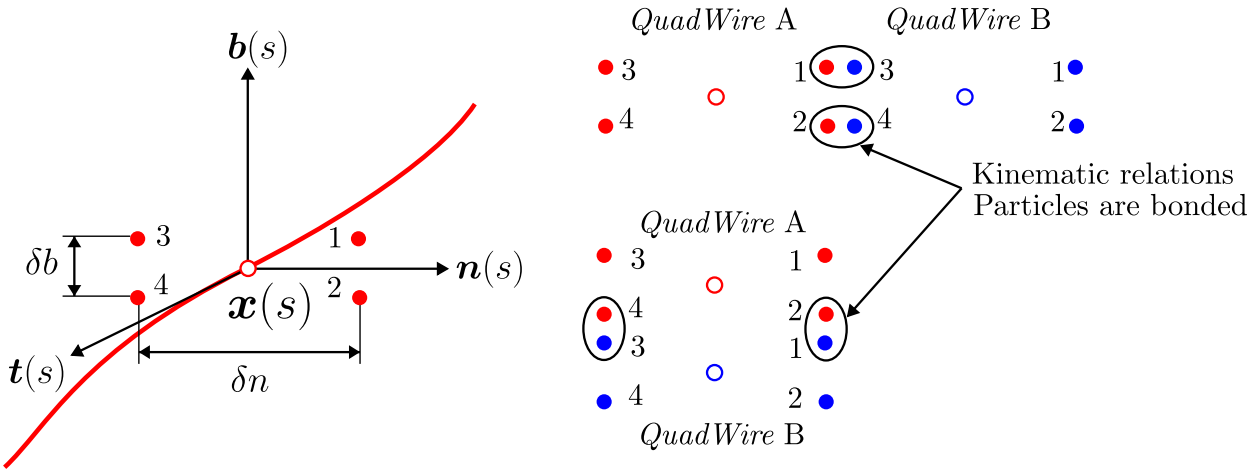

Figure 1: Left: *QuadWire* model with 4 particles indexed from 1 to 4. Right: kinematic relations between different beads. For instance, two different beads denoted by *QuadWire* A and *QuadWire* B are bonded in two different ways. When beads are next to each other, particles 1 and 2 of *QuadWire* A are respectively bonded with particles 3 and 4 of *QuadWire* B, and when beads are on top of each other, particles 2 and 4 of *QuadWire* A are respectively bonded with particles 1 and 3 of *QuadWire* B.

where linear coefficients have been introduced as internal forces per unit length $\boldsymbol{f}_k$ (N.m^{-1}) and internal forces $\boldsymbol{F}_k$ (N) and where $v_k^{*\prime}(s)$ refers to the derivative of $v_k^*(s)$ with respect to s. Note that the minus sign affecting the second term in the integral is purely conventional.

The consistency condition consists in ensuring that the space of rigid body motions $\mathcal{V}_R^*$ is the kernel of virtual power of internal forces i.e., , $\forall \overrightarrow{\boldsymbol{v}}^* \in \mathcal{V}_R^*$, PVI$(\overrightarrow{\boldsymbol{v}}^*) = 0$, hence:

$$\begin{cases} \forall \boldsymbol{v}_R^* \in \mathbb{R}^3, \int_0^l \sum_{k=1}^4 \boldsymbol{f}_k(s).\boldsymbol{v}_R^* \, \mathrm{d}s = 0 \\ \forall \boldsymbol{\omega}^* \in \mathcal{T}_{\mathrm{A}}^2, \int_0^l \sum_{k=1}^4 \left(\boldsymbol{f}_k(s).\boldsymbol{\omega}^*.\boldsymbol{x}_k(s) - \boldsymbol{F}_k(s).\boldsymbol{\omega}^*.\boldsymbol{x}_k'(s)\right) \mathrm{d}s = 0 \end{cases} \tag{14}$$

From the first equation of (14) one obtains:

$$\sum_{k=1}^4 \boldsymbol{f}_k(s) = 0 \tag{15}$$

One can note that the relation (15) is consistent with the definition of internal forces per unit length from the particle i over the particle j (with $(i,j) \in \{1,2,3,4\}^2$) denoted by $\boldsymbol{f}_{i\to j}(s)$ such as:

$$\begin{cases} \forall k \in \{1,2,3,4\}\,, \; \boldsymbol{f}_k(s) = \sum_{\substack{i=1 \\ i\neq k}}^4 \boldsymbol{f}_{i\to k}(s) \\ \forall (i,j) \in \{1,2,3,4\}^2\,, \; \boldsymbol{f}_{i\to j}(s) = -\boldsymbol{f}_{j\to i}(s) \end{cases} \tag{16}$$

Indeed, (16) implies (15).

Following internal force vectors naturally arise when using the consistency condition (15):

$$\begin{cases} \boldsymbol{f} = \sum_{k=1}^{4} \boldsymbol{f}_k = 0 \\ \boldsymbol{m}_n = \dfrac{\delta n}{2}\,(\boldsymbol{f}_1 + \boldsymbol{f}_2 - \boldsymbol{f}_3 - \boldsymbol{f}_4) \\ \boldsymbol{m}_b = \dfrac{\delta b}{2}\,(\boldsymbol{f}_1 - \boldsymbol{f}_2 + \boldsymbol{f}_3 - \boldsymbol{f}_4) \\ \boldsymbol{m}_\times = \dfrac{\delta n\,\delta b}{4}\,(\boldsymbol{f}_1 - \boldsymbol{f}_2 - \boldsymbol{f}_3 + \boldsymbol{f}_4) \end{cases} \quad \begin{cases} \boldsymbol{F} = \sum_{k=1}^{4} \boldsymbol{F}_k \\ \boldsymbol{M}_n = \dfrac{\delta n}{2}\,(\boldsymbol{F}_1 + \boldsymbol{F}_2 - \boldsymbol{F}_3 - \boldsymbol{F}_4) \\ \boldsymbol{M}_b = \dfrac{\delta b}{2}\,(\boldsymbol{F}_1 - \boldsymbol{F}_2 + \boldsymbol{F}_3 - \boldsymbol{F}_4) \\ \boldsymbol{M}_\times = \dfrac{\delta n\,\delta b}{4}\,(\boldsymbol{F}_1 - \boldsymbol{F}_2 - \boldsymbol{F}_3 + \boldsymbol{F}_4) \end{cases} \tag{17}$$

where $\boldsymbol{F}$ (N) (resp. $\boldsymbol{f}$ (N.m^{-1})) is the resultant force (resp. resultant force per unit length) applying to a material point. According to the definition (17), $\boldsymbol{M}_\times$ (N.m^2) (and $\boldsymbol{m}_\times$ (N.m)) tends to deform the bead cross-section as a saddle point for the $\boldsymbol{t}$ component, and as a trapezoid for the $\boldsymbol{n}$ and $\boldsymbol{b}$ components (see figure 2.e). Bending moments (resp. bending moments per unit length) correspond to the $\boldsymbol{t}$ component of $\boldsymbol{M}_n$ (N.m) and $\boldsymbol{M}_b$ (N.m) (resp. $\boldsymbol{m}_n$ (N) and $\boldsymbol{m}_b$ (N)) (see first column of figure 2.c and figure 2.d). Torsion (resp. torsion per unit length) corresponds to the $\boldsymbol{b}$ component of $\boldsymbol{M}_n$ (resp. $\boldsymbol{m}_n$) and to the $\boldsymbol{n}$ component of $\boldsymbol{M}_b$ (resp. $\boldsymbol{m}_b$) (see second column of figure 2.d and third column of figure 2.c). Furthermore, in equation (17) the index n in $\boldsymbol{m}_n$ and $\boldsymbol{M}_n$ refers to right particles minus left particles, which aligns with $\boldsymbol{n}$. Similarly, the index b refers to top particles minus bottom particles, which aligns with $\boldsymbol{b}$. Moreover, the index $\times$ refers to a "cross" as one diagonal (i.e., particles 1 and 4) is subtracted to the other diagonal (i.e., particles 2 and 3).

The consistency condition (15) reads $\boldsymbol{f} = 0$, while the second equation of (14) reads:

$$\forall \boldsymbol{\omega}^* \in \mathcal{T}^2_{\mathrm{A}},\ \int_0^l \boldsymbol{\Sigma}^\top : \boldsymbol{\omega}^*\,\mathrm{d}s = 0 \tag{18}$$

where the following second order generalized stress tensor has been introduced by using (5):

$$\begin{aligned} \boldsymbol{\Sigma}(s) = \ & \boldsymbol{t}(s) \otimes \boldsymbol{F}(s) - \boldsymbol{n}(s) \otimes \boldsymbol{m}_n(s) - \boldsymbol{b}(s) \otimes \boldsymbol{m}_b(s) \\ & + \boldsymbol{\omega}(s).\,(\boldsymbol{n}(s) \otimes \boldsymbol{M}_n(s) + \boldsymbol{b}(s) \otimes \boldsymbol{M}_b(s)) \end{aligned} \tag{19}$$

Equation (18) implies that the generalized stress $\boldsymbol{\Sigma}(s)$ must be symmetrical, as the orthogonal space of anti-symmetric second-order tensors $\mathcal{T}^2_{\mathrm{A}}$ is orthogonal to the space of symmetric second-order tensors $\mathcal{T}^2_{\mathrm{S}}$. Since (19) is not intrinsically symmetric, the consistency condition imposes relationships between internal forces $\boldsymbol{F}, \boldsymbol{m}_n, \boldsymbol{m}_b, \boldsymbol{M}_n, \boldsymbol{M}_b$.

In the following, the generalized stresses naturally arise as (i) the symmetric tensor $\boldsymbol{\Sigma}$ (N), which is analogous to the Cauchy stress tensor in conventional 3D models, (ii) a first order tensor $\boldsymbol{M}_\times$ (N.m^2), and (iii) an additional third order tensor denoted by $\boldsymbol{M}$ (N.m) defined as follows :

$$\begin{aligned} \boldsymbol{M}(s) = \ & \boldsymbol{t}(s) \otimes \boldsymbol{n}(s) \otimes \boldsymbol{M}_n(s) + \boldsymbol{t}(s) \otimes \boldsymbol{b}(s) \otimes \boldsymbol{M}_b(s) \\ & - \frac{1}{2}\,(\boldsymbol{b}(s) \otimes \boldsymbol{n}(s) + \boldsymbol{n}(s) \otimes \boldsymbol{b}(s)) \otimes \boldsymbol{m}_\times(s) \end{aligned} \tag{20}$$

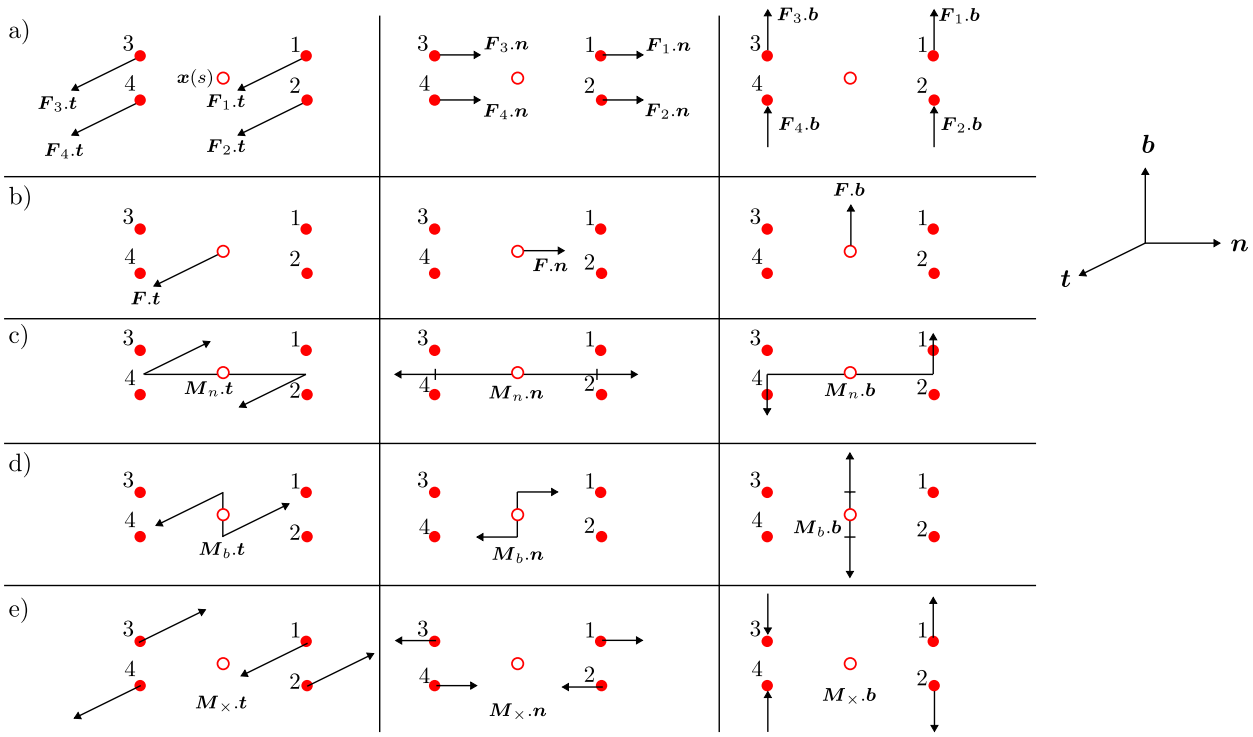

Figure 2: Interpretation of internal forces (similar interpretation also holds for internal forces per unit length). a) components of forces defined at each particle, b) components of the resultant force $\boldsymbol{F}$, c) mechanism for $\boldsymbol{M}_n$, d) mechanism for $\boldsymbol{M}_b$ and e) mechanism for $\boldsymbol{M}_\times$.

2.4. Generalized strains

Consider any observable function of the curvilinear abscissa s (e.g., displacement, velocity, temperature, etc.) denoted by $\overrightarrow{a} = (a_1, a_2, a_3, a_4)$, and the operator P giving the average a and differences $\delta^n a, \delta^b a, \delta^\times a$ defined as follows :

$$P : \overrightarrow{a} = (a_1, a_2, a_3, a_4) \mapsto \overrightarrow{a}_\delta = (a, \delta^n a, \delta^b a, \delta^\times a) \tag{21}$$

Where :

$$\begin{aligned} a &= \frac{a_1 + a_2 + a_3 + a_4}{4} \qquad \delta^n a = \frac{a_1 + a_2 - a_3 - a_4}{2} \\ \delta^b a &= \frac{a_1 - a_2 + a_3 - a_4}{2} \qquad \delta^\times a = a_1 - a_2 - a_3 + a_4 \end{aligned} \tag{22}$$

One can notice that P is bijective and $\overrightarrow{a} = P^{-1}(\overrightarrow{a}_\delta)$.

Thus, using (15) and (19), the virtual power of internal forces (13) reads:

$$\begin{aligned} \mathrm{PVI}(\overrightarrow{\boldsymbol{v}}^*) = \int_0^l \Bigg(& \boldsymbol{m}_n(s).\frac{\delta^n \boldsymbol{v}^*(s)}{\delta n} + \boldsymbol{m}_b(s).\frac{\delta^b \boldsymbol{v}^*(s)}{\delta b} + \boldsymbol{m}_\times(s).\frac{\delta^\times \boldsymbol{v}^*(s)}{\delta n\, \delta b} - \boldsymbol{F}(s).\boldsymbol{v}^{*\prime}(s) \\ & - \boldsymbol{M}_n(s).\frac{\delta^n \boldsymbol{v}^{*\prime}(s)}{\delta n} - \boldsymbol{M}_b(s).\frac{\delta^b \boldsymbol{v}^{*\prime}(s)}{\delta b} - \boldsymbol{M}_\times(s).\frac{\delta^\times \boldsymbol{v}^{*\prime}(s)}{\delta n\, \delta b} \Bigg) \mathrm{d}s \end{aligned} \tag{23}$$

On the one hand, the first order gradient defined in Appendix A is introduced as the following second order tensor:

$$\overrightarrow{\boldsymbol{\nabla}}\,\overrightarrow{\boldsymbol{v}}^*(s) = \boldsymbol{v}^{*\prime}(s)\otimes\boldsymbol{t}(s) + \frac{\delta^n\boldsymbol{v}^*(s)}{\delta n}\otimes\boldsymbol{n}(s) + \frac{\delta^b\boldsymbol{v}^*(s)}{\delta b}\otimes\boldsymbol{b}(s) \tag{24}$$

And the (virtual) Eulerian tangential rate of deformation tensor as the symmetric part of the first gradient (24):

$$\boldsymbol{d}^*_\xi(s) = \frac{1}{2}\left(\overrightarrow{\boldsymbol{\nabla}}\,\overrightarrow{\boldsymbol{v}}^*(s) + \overrightarrow{\boldsymbol{\nabla}}\,\overrightarrow{\boldsymbol{v}}^*(s)^\top\right) \tag{25}$$

On the other hand, a complementary generalized rate of deformation tensor is defined from the second gradient obtained in Appendix A, which reads as the following third order tensor:

$$\begin{aligned}\boldsymbol{d}^*_\chi(s) \;&= \frac{\delta^n\boldsymbol{v}^{*\prime}(s)}{\delta n}\otimes\boldsymbol{n}(s)\otimes\boldsymbol{t}(s) + \frac{\delta^b\boldsymbol{v}^{*\prime}(s)}{\delta b}\otimes\boldsymbol{b}(s)\otimes\boldsymbol{t}(s)\\ &+\frac{\delta^\times\boldsymbol{v}^*(s)}{\delta n\delta b}\otimes(\boldsymbol{n}(s)\otimes\boldsymbol{b}(s)+\boldsymbol{b}(s)\otimes\boldsymbol{n}(s)) + \boldsymbol{v}^{*\prime}(s)\otimes\boldsymbol{t}'(s)\otimes\boldsymbol{t}(s)\\ &+(\boldsymbol{b}(s).\boldsymbol{\omega}(s).\boldsymbol{n}(s))\left(\frac{\delta^n\boldsymbol{v}^*(s)}{\delta n}\otimes\boldsymbol{b}(s)\otimes\boldsymbol{t}(s) - \frac{\delta^b\boldsymbol{v}^*(s)}{\delta b}\otimes\boldsymbol{n}(s)\otimes\boldsymbol{t}(s)\right)\end{aligned} \tag{26}$$

Moreover, the following vector is a contribution of the third order gradient that will arise in the virtual power of internal forces:

$$\boldsymbol{d}^*_\gamma(s) = \frac{\delta^\times\boldsymbol{v}^{*\prime}(s)}{\delta n\delta b} \tag{27}$$

Consequently, using the fact that $\boldsymbol{\Sigma}$ is symmetric, (23) reads:

$$\mathrm{PVI}(\overrightarrow{\boldsymbol{v}}^*) = -\int_0^l\left(\boldsymbol{d}^*_\xi(s):\boldsymbol{\Sigma}(s) + \boldsymbol{d}^*_\chi(s)\vdots\boldsymbol{M}(s) + \boldsymbol{d}^*_\gamma(s).\boldsymbol{M}_\times(s)\right)\mathrm{d}s \tag{28}$$

It should be noted that interestingly, although the 2nd gradient component involving $\boldsymbol{v}^{*\prime\prime}$ is not activated in the *QuadWire* model (see. Appendix A), a 3rd gradient component naturally arises in the derivation. This means that the geometrical constraints associated with the choice of using 4 particles are automatically translated into a selection of components of higher-order gradients, which significantly reduces the number of DoF with respect to a complete 3rd order 3D continuum model.

Since the second order tensor $\boldsymbol{d}^*_\xi$ (s^{-1}) is symmetric, there are 6 independent components, while there are only 9 additional independent components in $\boldsymbol{d}^*_\chi$ ($\mathrm{m}^{-1}.\mathrm{s}^{-1}$) (since the last three terms in (26) already appear in $\boldsymbol{d}^*_\xi$) and 3 additional components for $\boldsymbol{d}^*_\gamma$ ($\mathrm{m}^{-2}.\mathrm{s}^{-1}$). So there is a total of 18 generalized strain components. Similarly, the model involves 18 generalized force components –namely 6 components for the symmetric second order tensor $\boldsymbol{\Sigma}$, and 9 components for the third order tensor $\boldsymbol{M}$ and 3 for $\boldsymbol{M}_\times$. In addition, as already mentioned, there are 12 kinematic DoF (i.e., 4 displacements with 3 components each).

2.5. *Virtual power principle*

The virtual power principle is used to derive a weak form of the balance equations along with boundary conditions. To do so, consider the following linear form of $\overrightarrow{\boldsymbol{v}}^*$ as the power of external forces:

$$\mathrm{PVE}(\overrightarrow{\boldsymbol{v}}^*) = \sum_{k=1}^{4} \int_0^l \boldsymbol{f}_k^{\mathrm{ext}}(s).\boldsymbol{v}_k^*(s)\,\mathrm{d}s + \boldsymbol{F}_k^{\mathrm{ext}}(0).\boldsymbol{v}_k^*(0) + \boldsymbol{F}_k^{\mathrm{ext}}(l).\boldsymbol{v}_k^*(l) \tag{29}$$

where $\boldsymbol{f}_k^{\mathrm{ext}}$ (N.m^{-1}) are external forces per unit length, and $\boldsymbol{F}_k^{\mathrm{ext}}$ (N) are external forces applied to both ends of the domain $\mathcal{C}$ (i.e., $s = 0$ and $s = l$) with $1 \leq k \leq 4$. Using the same notations as in (17), the power of external forces reads:

$$\begin{aligned}
\mathrm{PVE}(\overrightarrow{\boldsymbol{v}}^*) \;=& \int_0^l \left(\boldsymbol{f}^{\mathrm{ext}}(s).\boldsymbol{v}^*(s) + \boldsymbol{m}_n^{\mathrm{ext}}(s).\frac{\delta^n \boldsymbol{v}^*(s)}{\delta n} + \boldsymbol{m}_b^{\mathrm{ext}}(s).\frac{\delta^b \boldsymbol{v}^*(s)}{\delta b} + \boldsymbol{m}_\times^{\mathrm{ext}}(s).\frac{\delta^\times \boldsymbol{v}^*(s)}{\delta n\,\delta b} \right) \mathrm{d}s \\
&+ \boldsymbol{F}^{\mathrm{ext}}(0).\boldsymbol{v}^*(0) + \boldsymbol{M}_n^{\mathrm{ext}}(0).\frac{\delta^n \boldsymbol{v}^*(0)}{\delta n} + \boldsymbol{M}_b^{\mathrm{ext}}(0).\frac{\delta^b \boldsymbol{v}^*(0)}{\delta b} + \boldsymbol{M}_\times^{\mathrm{ext}}(0).\frac{\delta^\times \boldsymbol{v}^*(0)}{\delta n \delta b} \\
&+ \boldsymbol{F}^{\mathrm{ext}}(l).\boldsymbol{v}^*(l) + \boldsymbol{M}_n^{\mathrm{ext}}(l).\frac{\delta^n \boldsymbol{v}^*(l)}{\delta n} + \boldsymbol{M}_b^{\mathrm{ext}}(l).\frac{\delta^b \boldsymbol{v}^*(l)}{\delta b} + \boldsymbol{M}_\times^{\mathrm{ext}}(l).\frac{\delta^\times \boldsymbol{v}^*(l)}{\delta n \delta b}
\end{aligned} \tag{30}$$

The power of acceleration forces is neglected, so that the virtual power principle reduces to:

$$\forall\, \overrightarrow{\boldsymbol{v}}^* \in \mathcal{V}^*, \quad \mathrm{PVI}\left(\overrightarrow{\boldsymbol{v}}^*\right) + \mathrm{PVE}\left(\overrightarrow{\boldsymbol{v}}^*\right) = 0 \tag{31}$$

From the weak form (31) one can derive the balance equations and boundary conditions of the *QuadWire* model (see. Appendix B). Nevertheless, the weak form (31) is directly discretized within the framework of FEA to obtain numerical results (see. Appendix D).

3. Thermodynamic analysis of deformation processes

The thermodynamic analysis of a deformation process is conducted to derive a hyperelastic behavior for the *QuadWire* model. The first and second laws of thermodynamics are applied, enabling the derivation of energy balance equations as well as the Clausius-Duhem inequality, which are essential to derive the material behavior within the framework of GSM.

Consider a real motion $\overrightarrow{\boldsymbol{v}} \in \mathcal{V}$, and the total energy E_{tot} (J) composed of the kinetic energy C (J) and the internal energy U (J), i.e., $E_{\mathrm{tot}} = C + U$. In virtue of the first law of thermodynamics, there is no production of total energy, hence the total energy variation $\dot{E}_{\mathrm{tot}}$ is balanced by the power brought to the domain $\mathcal{C}$, which reads as the power of external forces, denoted as $\mathrm{P}_{\mathrm{EXT}} = \mathrm{PVE}(\overrightarrow{\boldsymbol{v}})$ (W) and heat input denoted by Q (W):

$$\dot{E}_{\mathrm{tot}} = \dot{C} + \dot{U} = Q + \mathrm{P}_{\mathrm{EXT}} \tag{32}$$

Hence, considering the power of internal forces $\mathrm{P}_{\mathrm{INT}} = \mathrm{PVI}(\overrightarrow{\boldsymbol{v}})$ and acceleration forces which read as time derivative of the kinetic energy $\dot{C}$, and using the virtual power principle $\mathrm{P}_{\mathrm{EXT}} + \mathrm{P}_{\mathrm{INT}} = \dot{C}$ (where $\dot{C}$ has been neglected in previous sections), one obtains the balance equation on internal energy:

$$\dot{U} = Q - \mathrm{P}_{\mathrm{INT}} \tag{33}$$

where the deformation power $-\mathrm{P}_{\mathrm{INT}}$ reads as a production of internal energy. Consider the internal energy density per unit mass e_U (J.kg^{-1}) so that :

$$U = \int_{\mathcal{C}} \rho(s)\, e_U(s)\ \mathrm{d}s \tag{34}$$

where ρ (kg.m^{-1}) is the density defined as the mass per unit length. Since no mass transport is considered one simply obtains:

$$\dot{U} = \int_{\mathcal{C}} \rho(s)\, \dot{e}_U(s)\ \mathrm{d}s \tag{35}$$

The heat input Q is composed of two local contributions. The first heat density is the heat per unit length $r(s)$ (W.m^{-1}) – accounting for two contributions from the 3D point of view (see. figure 3), namely the heat input per unit volume integrated over the bead section and the heat input per unit surface from external surface of the bead integrated over the contour of the bead cross-section. The second heat density is the tangential heat q (W) – accounting from the 3D point of view (see. figure 3) for the tangential heat input per unit surface integrated over the bead section. Hence:

$$Q = \int_{\mathcal{C}} r(s)\ \mathrm{d}s - (q(l) - q(0)) \tag{36}$$

Which leads to:

$$Q = \int_{\mathcal{C}} (r(s) - q'(s))\ \mathrm{d}s \tag{37}$$

Using (33) along with (35), (37) and (28) the local internal energy balance equation in the deformed

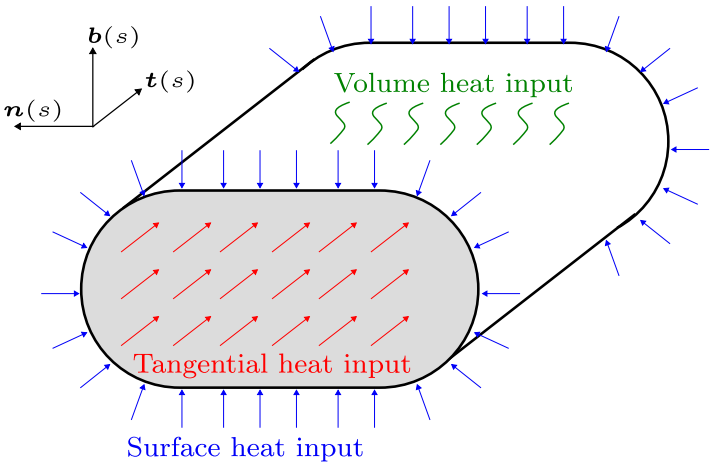

Figure 3: Heat input from the 3D point of view.

configuration therefore reads :

$$\rho(s)\, \dot{e}_U(s) = \boldsymbol{\Sigma}(s) : \dot{\boldsymbol{\xi}}(s) + \boldsymbol{M}(s) \vdots \dot{\boldsymbol{\chi}}(s) + \boldsymbol{M}_{\times}(s).\dot{\boldsymbol{\gamma}}(s) + r(s) - q'(s) \tag{38}$$

Consider the entropy of the system S (J.K^{-1}). The second law of thermodynamics states that the entropy production P_S (W.K^{-1}) is positive i.e., $P_S \geq 0$. Classically heat inputs contribute to

the entropy balance through the inverse of the absolute temperature. Since the *QuadWire* model contains 4 particles, one can define the absolute temperature as follows:

$$\overrightarrow{T}(s) = (T_1(s), T_2(s), T_3(s), T_4(s)) \tag{39}$$

Only the average temperature $T(s) = 1/4 \sum_{k=1}^{4} T_k(s)$ is considered in the following for the sake of simplicity. Indeed, only the global energy balance equations are derived for the 4 particles considered altogether. Therefore one can write the contribution of heat inputs in the entropy balance such as:

$$\dot{S} = \int_{\mathcal{C}} \frac{r(s)}{T(s)} \, \mathrm{d}s - \left(\frac{q(l)}{T(l)} - \frac{q(0)}{T(0)} \right) + P_S \tag{40}$$

Hence:

$$\dot{S} = \int_{\mathcal{C}} \left(\frac{r(s)}{T(s)} - \frac{q'(s)}{T(s)} + \frac{T'(s)\, q(s)}{T(s)^2} \right) \mathrm{d}s + P_S \tag{41}$$

Consider the entropy density per unit mass denoted by e_S (J.K^{-1}.kg^{-1}) so that:

$$S = \int_{\mathcal{C}} \rho(s)\, e_S(s) \, \mathrm{d}s \tag{42}$$

Since no mass transport is considered one simply obtains:

$$\dot{S} = \int_{\mathcal{C}} \rho(s)\, \dot{e}_S(s) \, \mathrm{d}s \tag{43}$$

It is also assumed that there exists a density of entropy production per unit length denoted by $p_S(s)$ (W.K^{-1}.m^{-1}) so that:

$$P_S = \int_{\mathcal{C}} p_S(s) \, \mathrm{d}s \tag{44}$$

Hence, by using (41) along with (43) and (44) the local entropy balance equation reads :

$$\rho(s)\, T(s)\, \dot{e}_S(s) = r(s) - q'(s) + \frac{T'(s)\, q(s)}{T(s)} + T(s)\, p_S(s) \tag{45}$$

Consider the Helmholtz free energy density per unit mass ψ (J.kg^{-1}) defined by:

$$\psi(s) = e_U(s) - T(s)\, e_S(s) \tag{46}$$

In addition, consider which is positive in virtue of the second law of thermodynamics:

$$D(s) = T(s)\, p_S(s) \geq 0 \tag{47}$$

The thermodynamics balance equation of the *QuadWire* medium (i.e., Clausius-Duhem inequality) is obtained by eliminating the heat inputs in (38) and (45) such as:

$$\boldsymbol{\Sigma}(s) : \dot{\boldsymbol{\xi}}(s) + \boldsymbol{M}(s) \vdots \dot{\boldsymbol{\chi}}(s) + \boldsymbol{M}_{\times}(s) . \dot{\boldsymbol{\gamma}}(s) - \rho(s) \, \left(\dot{\psi}(s) + \dot{T}(s)\, e_S(s) \right) - \frac{T'(s)\, q(s)}{T(s)} = D(s) \tag{48}$$

This thermodynamic balance equation (48) should be verified for any state of the system and all possible time evolution from the considered state.

Since the model is derived within the framework of finite strain theory, the balance equation (48) should be derived in the reference configuration. Generalized stress tensors $\boldsymbol{\Sigma}$, $\boldsymbol{M}$ and $\boldsymbol{M}_{\times}$ are defined in the deformed configuration but can be translated in the reference configuration into $\boldsymbol{\Sigma}_0$, $\boldsymbol{M}_0$ and $\boldsymbol{M}_{\times 0}$. The stress tensor $\boldsymbol{\Sigma}_0$ is classically determined by $\boldsymbol{\Sigma}_0 = J^{-1}\boldsymbol{R}^{\top}.\boldsymbol{\Sigma}.\boldsymbol{R}$, hence using (19):

$$\begin{aligned}\boldsymbol{\Sigma}_0(s_0) = \quad & (\boldsymbol{t}_0(s_0) \otimes \boldsymbol{F}_0(s_0) - \boldsymbol{n}_0(s_0) \otimes \boldsymbol{m}_{n0}(s_0) - \boldsymbol{b}_0(s_0) \otimes \boldsymbol{m}_{b0}(s_0)) \\ & + \widetilde{\boldsymbol{\omega}}_0(s_0).\left(\boldsymbol{n}_0(s_0) \otimes \boldsymbol{M}_{n0}(s_0) + \boldsymbol{b}_0(s_0) \otimes \boldsymbol{M}_{b0}(s_0)\right)\end{aligned} \tag{49}$$

where the following anti-symmetric 2nd order tensor has been introduced:

$$\widetilde{\boldsymbol{\omega}}_0(s_0) = \left(\boldsymbol{\omega}_0(s_0) + \boldsymbol{R}^{\top}(s_0).\frac{\mathrm{d}\boldsymbol{R}(s_0)}{\mathrm{d}s_0}\right) \tag{50}$$

and where internal forces in the reference configuration have been defined as follows:

$$\begin{cases} \boldsymbol{f}_0 = 0 \\ \boldsymbol{m}_{n0} = \boldsymbol{m}_n.\left(J^{-1}\boldsymbol{R}\right) \\ \boldsymbol{m}_{b0} = \boldsymbol{m}_b.\left(J^{-1}\boldsymbol{R}\right) \\ \boldsymbol{m}_{\times 0} = \boldsymbol{m}_{\times}.\left(J^{-1}\boldsymbol{R}\right) \end{cases} \quad \begin{cases} \boldsymbol{F}_0 = \boldsymbol{F}.\left(J^{-1}\boldsymbol{R}\right) \\ \boldsymbol{M}_{n0} = \boldsymbol{M}_n.\left(J^{-1}\boldsymbol{R}\right) \\ \boldsymbol{M}_{b0} = \boldsymbol{M}_b.\left(J^{-1}\boldsymbol{R}\right) \\ \boldsymbol{M}_{\times 0} = \boldsymbol{M}_{\times}.\left(J^{-1}\boldsymbol{R}\right) \end{cases} \tag{51}$$

A similar expression is derived for $\boldsymbol{M}_0$ from (20):

$$\begin{aligned}\boldsymbol{M}_0(s_0) = \quad & \boldsymbol{t}_0(s_0) \otimes \boldsymbol{n}_0(s_0) \otimes \boldsymbol{M}_{n0}(s_0) + \boldsymbol{t}_0(s_0) \otimes \boldsymbol{b}_0(s_0) \otimes \boldsymbol{M}_{b0}(s_0) \\ & -\frac{1}{2}\left(\boldsymbol{b}_0(s_0) \otimes \boldsymbol{n}_0(s_0) + \boldsymbol{n}_0(s_0) \otimes \boldsymbol{b}_0(s_0)\right) \otimes \boldsymbol{m}_{\times 0}(s_0)\end{aligned} \tag{52}$$

The generalized Eulerian rates of deformation $\boldsymbol{d}_{\xi}, \boldsymbol{d}_{\chi}, \boldsymbol{d}_{\gamma}$ are also translated in the reference configuration into $\dot{\boldsymbol{\xi}}, \dot{\boldsymbol{\chi}}, \dot{\boldsymbol{\gamma}}$. Classically $\dot{\boldsymbol{\xi}} = J^2\boldsymbol{R}^{\top}.\boldsymbol{d}_{\xi}.\boldsymbol{R}$, hence:

$$\begin{aligned}\dot{\boldsymbol{\xi}}(s_0) = \quad & \frac{J(s_0)^2}{2}\left(\boldsymbol{R}(s_0)^{\top}.\left(\boldsymbol{v}'(s_0) \otimes \boldsymbol{t}_0(s_0) + \frac{\delta^n \boldsymbol{v}(s_0)}{\delta n} \otimes \boldsymbol{n}_0(s_0) + \frac{\delta^b \boldsymbol{v}(s_0)}{\delta b} \otimes \boldsymbol{b}_0(s_0)\right)\right. \\ & \left. + \left(\boldsymbol{t}_0(s_0) \otimes \boldsymbol{v}'(s_0) + \boldsymbol{n}_0(s_0) \otimes \frac{\delta^n \boldsymbol{v}(s_0)}{\delta n} + \boldsymbol{b}_0(s_0) \otimes \frac{\delta^b \boldsymbol{v}(s_0)}{\delta b}\right).\boldsymbol{R}(s_0)\right)\end{aligned} \tag{53}$$

A similar expression is derived for $\dot{\boldsymbol{\chi}}$ from (26):

$$\begin{aligned}\dot{\boldsymbol{\chi}}(s_0) \quad & = J(s_0)^2\,\boldsymbol{R}(s_0)^{\top}.\left(\frac{\delta^n \boldsymbol{v}'(s_0)}{\delta n} \otimes \boldsymbol{n}_0(s_0) \otimes \boldsymbol{t}_0(s_0) + \frac{\delta^b \boldsymbol{v}'(s_0)}{\delta b} \otimes \boldsymbol{b}_0(s_0) \otimes \boldsymbol{t}_0(s_0)\right. \\ & + \frac{\delta^{\times} \boldsymbol{v}(s_0)}{\delta n \delta b} \otimes \left(\boldsymbol{n}_0(s_0) \otimes \boldsymbol{b}_0(s_0) + \boldsymbol{b}_0(s_0) \otimes \boldsymbol{n}_0(s_0)\right) + \boldsymbol{v}'(s_0) \otimes \left(\widetilde{\boldsymbol{\omega}}_0(s_0).\boldsymbol{t}_0(s_0)\right) \otimes \boldsymbol{t}_0(s_0) \\ & \left. + \left(\boldsymbol{b}_0(s_0).\widetilde{\boldsymbol{\omega}}_0(s_0).\boldsymbol{n}_0(s_0)\right)\left(\frac{\delta^n \boldsymbol{v}(s_0)}{\delta n} \otimes \boldsymbol{b}_0(s_0) \otimes \boldsymbol{t}_0(s_0) - \frac{\delta^b \boldsymbol{v}(s_0)}{\delta b} \otimes \boldsymbol{n}_0(s_0) \otimes \boldsymbol{t}_0(s_0)\right)\right)\end{aligned} \tag{54}$$

and from (27):

$$\dot{\boldsymbol{\gamma}}(s_0) = J(s_0)^2\, \boldsymbol{R}(s_0)^\top . \frac{\delta^\times \boldsymbol{v}'(s_0)}{\delta n \delta b} \tag{55}$$

Thus by multiplying the balance equation (48) by $J(s_0)$ (to account for the fact that $\mathrm{d}s = J(s_0)\mathrm{d}s_0$) the balance equation in the reference configuration reads:

$$\boldsymbol{\Sigma}_0 : \dot{\boldsymbol{\xi}} + \boldsymbol{M}_0 \vdots \dot{\boldsymbol{\chi}} + \boldsymbol{M}_{\times 0} . \dot{\boldsymbol{\gamma}} - \rho_0 \left(\dot{\psi} + \dot{T}\, e_S \right) - T^{-1} \frac{\mathrm{d}T}{\mathrm{d}s_0}\, q = D_0 \tag{56}$$

where the density in the reference configuration reads: $\rho_0 = J\rho$ and where $D_0 = JD$.

4. Thermo-elastic constitutive laws

Local behavior is considered, that is to say, that state variables are defined for each curvilinear abscissa s_0 and not as entire distributions (e.g., $T : s_0 \in [0, l_0] \mapsto T(s_0)$). Thus, for each s_0, the state variables are the generalized strains $\boldsymbol{\xi}(s_0)$, $\boldsymbol{\chi}(s_0)$ and $\boldsymbol{\gamma}(s_0)$, the average temperature $T(s_0)$, and the average temperature gradient $\mathrm{d}T(s_0)/\mathrm{d}s_0$, which is independent of $T(s_0)$ for each fixed s_0. Constitutive laws are obtained by defining two state functions of local state variables, namely the free energy per unit mass denoted by $\Psi(\boldsymbol{\xi}(s_0), \boldsymbol{\chi}(s_0), \boldsymbol{\gamma}(s_0), T(s_0)) = \psi(s_0)$, which is assumed to be independent of $\mathrm{d}T(s_0)/\mathrm{d}s_0$, and the dissipated power per unit length denoted by $\mathcal{D}(T(s_0), \mathrm{d}T(s_0)/\mathrm{d}s_0) = D_0(s_0)$, which is assumed to be independent of $\boldsymbol{\xi}(s_0)$, $\boldsymbol{\chi}(s_0)$ and $\boldsymbol{\gamma}(s_0)$.

The following relationship holds:

$$\dot{\psi} = \frac{\partial \Psi}{\partial \boldsymbol{\xi}} : \dot{\boldsymbol{\xi}} + \frac{\partial \Psi}{\partial \boldsymbol{\chi}} \vdots \dot{\boldsymbol{\chi}} + \frac{\partial \Psi}{\partial \boldsymbol{\gamma}} . \dot{\boldsymbol{\gamma}} + \frac{\partial \Psi}{\partial T}\, \dot{T} \tag{57}$$

The balance equation (56) should be verified for all states. It is possible to consider without loss of generality all states $\boldsymbol{\xi}(s_0), \boldsymbol{\chi}(s_0), \boldsymbol{\gamma}(s_0), T(s_0)$ with $\mathrm{d}T(s_0)/\mathrm{d}s_0 = 0$. Since Ψ does not depend on $\mathrm{d}T(s_0)/\mathrm{d}s_0$, all conclusions drawn on Ψ from $\mathrm{d}T(s_0)/\mathrm{d}s_0 = 0$ remain valid for states such as $\mathrm{d}T(s_0)/\mathrm{d}s_0 \neq 0$. Indeed the function Ψ does not depend on the entire distribution of temperature $s_0 \mapsto T(s_0)$ but only on the value $T(s_0)$ for fixed s_0. For states $\mathrm{d}T(s_0)/\mathrm{d}s_0 = 0$, reversibility of elastic behavior implies that $\mathcal{D}(T(s_0), 0) = 0$. Hence using (57) the balance equation (56) reduces to:

$$\left(\boldsymbol{\Sigma}_0 - \rho_0 \frac{\partial \Psi}{\partial \boldsymbol{\xi}} \right) : \dot{\boldsymbol{\xi}} + \left(\boldsymbol{M}_0 - \rho_0 \frac{\partial \Psi}{\partial \boldsymbol{\chi}} \right) \vdots \dot{\boldsymbol{\chi}} + \left(\boldsymbol{M}_{\times 0} - \rho_0 \frac{\partial \Psi}{\partial \boldsymbol{\gamma}} \right) . \dot{\boldsymbol{\gamma}} - \rho_0 \left(\frac{\partial \Psi}{\partial T} + e_S \right) \dot{T} = 0 \tag{58}$$

Hence (considering the orthogonal subspaces of the spaces to which the generalized strain rates belong):

$$\boldsymbol{\Sigma}_0 = \rho_0 \frac{\partial \Psi}{\partial \boldsymbol{\xi}} \qquad \boldsymbol{M}_0 = \rho_0 \frac{\partial \Psi}{\partial \boldsymbol{\chi}} \qquad \boldsymbol{M}_{\times 0} = \rho_0 \frac{\partial \Psi}{\partial \boldsymbol{\gamma}} \tag{59}$$

All secondary variables involved in the balance equation (56) have been explicitly related to state variables through the energetic potential Ψ. This thermodynamic analysis enables us to easily extend in subsequent contributions the hyperelastic behavior to visco-elasticity or elasto-plasticity

by introducing adequate dissipation potential. To facilitate numerical implementation, numerical examples provided in the following are carried out for linear elasticity under infinitesimal strain assumption. Therefore a quadratic free energy Ψ is considered. The temperature variation $\Delta T(s_0) = T(s_0) - T_{\text{ref}}$ (where T_{ref} is a reference temperature) is used as a state variable instead of $T(s_0)$. In addition, since eigenstrain should be considered in AM, an additional state variable denoted by $\Gamma(s_0)$ representing any physical phenomena such as phase transformation, polymerization, etc., and inducing eigenstrain (e.g., volume variation or deviatoric strain) is considered at this stage. Since the heat equation is not derived one can only consider the following quadratic form:

$$\begin{aligned}\rho_0\,\Psi = \;& \frac{1}{2}\left(\boldsymbol{\xi} : \boldsymbol{R}^{\xi} : \boldsymbol{\xi} + \boldsymbol{\chi} \vdots \boldsymbol{R}^{\chi} \vdots \boldsymbol{\chi} + \boldsymbol{\gamma}.\boldsymbol{R}^{\gamma}.\boldsymbol{\gamma}\right) + \boldsymbol{\xi} : \boldsymbol{R}^{\xi\chi} \vdots \boldsymbol{\chi} + \boldsymbol{\xi} : \boldsymbol{R}^{\xi\gamma}.\boldsymbol{\gamma} + \boldsymbol{\chi} \vdots \boldsymbol{R}^{\chi\gamma}.\boldsymbol{\gamma} \\ & - \left(\boldsymbol{\xi} : \boldsymbol{R}^{\xi} : \boldsymbol{\alpha}^{\xi} + \boldsymbol{\chi} \vdots \boldsymbol{R}^{\chi} \vdots \boldsymbol{\alpha}^{\chi} + \boldsymbol{\gamma} : \boldsymbol{R}^{\gamma}.\boldsymbol{\alpha}^{\gamma}\right) \Delta T \\ & - \left(\boldsymbol{\xi} : \boldsymbol{R}^{\xi} : \boldsymbol{\beta}^{\xi} + \boldsymbol{\chi} \vdots \boldsymbol{R}^{\chi} \vdots \boldsymbol{\beta}^{\chi} + \boldsymbol{\gamma} : \boldsymbol{R}^{\gamma}.\boldsymbol{\beta}^{\gamma}\right) \Gamma\end{aligned} \tag{60}$$

where $\boldsymbol{R}^{\xi}$ (N), $\boldsymbol{R}^{\chi}$ (N.m^2) and $\boldsymbol{R}^{\gamma}$ (N.m^4) are respectively fourth, sixth and second order positive definite stiffness tensors (i.e., 21, 45 and 6 components respectively), $\boldsymbol{R}^{\xi\chi}$ (N.m), $\boldsymbol{R}^{\xi\gamma}$ (N.m^2) and $\boldsymbol{R}^{\chi\gamma}$ (N.m^3) are respectively fifth, third and fourth order coupling stiffness tensors. In addition, $\boldsymbol{\alpha}^{\xi}$ (K^{-1}) and $\boldsymbol{\beta}^{\xi}$ are second order tensors, and $\boldsymbol{\alpha}^{\chi}$ (K^{-1}) and $\boldsymbol{\beta}^{\chi}$ are third order tensors. Using constitutive laws (59) one simply obtains the following thermo-elastic behavior:

$$\left\{\begin{aligned}\boldsymbol{\Sigma}_0 &= \boldsymbol{R}^{\xi} : \left(\boldsymbol{\xi} - \boldsymbol{\alpha}^{\xi}\Delta T - \boldsymbol{\beta}^{\xi}\Gamma\right) + \boldsymbol{R}^{\xi\chi} \vdots \boldsymbol{\chi} + \boldsymbol{R}^{\xi\gamma}.\boldsymbol{\gamma} \\ \boldsymbol{M}_0 &= \boldsymbol{R}^{\chi} \vdots \left(\boldsymbol{\chi} - \boldsymbol{\alpha}^{\chi}\Delta T - \boldsymbol{\beta}^{\chi}\Gamma\right) + \boldsymbol{\xi} : \boldsymbol{R}^{\xi\chi} + \boldsymbol{R}^{\chi\gamma}.\boldsymbol{\gamma} \\ \boldsymbol{M}_{\times 0} &= \boldsymbol{R}^{\gamma}.\left(\boldsymbol{\gamma} - \boldsymbol{\alpha}^{\gamma}\Delta T - \boldsymbol{\beta}^{\gamma}\Gamma\right) + \boldsymbol{\xi} : \boldsymbol{R}^{\xi\gamma} + \boldsymbol{\chi} : \boldsymbol{R}^{\chi\gamma}\end{aligned}\right. \tag{61}$$

Several tensors have been introduced to capture the material behavior and should be identified by fitting the Helmholtz free energy per unit length of the *QuadWire* with a detailed 3D conventional computation. Several stiffness tensors involved in (61) may be neglected without compromising the model accuracy. For instance based on a simple homogenization procedure detailed in Appendix C, the following behavior is considered in the following:

$$\left\{\begin{aligned}\boldsymbol{\Sigma}_0 &= \boldsymbol{R}^{\xi} : \left(\boldsymbol{\xi} - \boldsymbol{\alpha}^{\xi}\Delta T\right) \\ \boldsymbol{M}_0 &= \boldsymbol{R}^{\chi} \vdots \boldsymbol{\chi}\end{aligned}\right. \tag{62}$$

It should be noted that the homogenization procedure simply consists in identifying the *QuadWire* and 3D free energy per unit length by assuming that the Representative Volume Element (RVE) is a simple single hexahedron element in 3D. Of course, this is not the aim of the proposed work, as the *QuadWire* should capture the complex behavior of the real bead. But this homogenization was only meant to a priori reduce the total number of stiffness components to identify.

5. Identification of material parameters

Using the simple behavior (62) a total of 66 components should be identified. However, the crude homogenization procedure derived in Appendix C enables to a priori reduce the number

of non-zero components to 9 for $\boldsymbol{R}^{\xi}$ and 15 for $\boldsymbol{R}^{\chi}$. Therefore only 24 stiffness components are considered and gathered into a column vector denoted by $p \in \mathbb{R}^{24}$. In addition, the thermal expansion is assumed to be $\boldsymbol{\alpha}^{\xi} = \alpha \mathbf{1}$ where α (K^{-1}) is the thermal coefficient of the material.

The identification of stiffness components p is carried out by fitting the Helmholtz free energy per unit length of the *QuadWire* model with the one obtained with a classical isotropic 3D FEA. Hence the solution $p^{\dagger}$ of the following minimization problem is used as the "correct" stiffness components in following sections:

$$\left\{ \begin{array}{ll} p^{\dagger} = & \underset{p \in \mathbb{R}^{24}}{\operatorname{argmin}} \, J(p) + \epsilon \, \|p - p^{0}\|^{2} \\ \text{s.t.} & \text{the principle of virtual power (31) is verified} \end{array} \right. \tag{63}$$

where the objective function $J(p)$ reads:

$$J(p) = \frac{1}{2} \int_{0}^{l} \left(\rho \, \psi(s) - \rho^{\mathrm{3D}} \, \psi^{\mathrm{3D}}(s) \right)^{2} \mathrm{d}s \tag{64}$$

where $\rho \, \psi(s)$ is derived from (60), and where $\rho^{\mathrm{3D}} \, \psi^{\mathrm{3D}}(s)$ is the Helmholtz free energy per unit length of the detailed 3D simulation. The 3D model is discretized using classical linear FEA to compute $\rho^{\mathrm{3D}} \, \psi^{\mathrm{3D}}(s)$ and a simple FEA implementation of the *QuadWire* model detailed in Appendix D, coded in *Python* [29] and accessible in the repository [30] is used to compute $\rho \, \psi(s)$. In addition, $p^{0} \in \mathbb{R}^{24}$ is a reference set of stiffness parameters given in (C.24) and (C.25) and ϵ is a positive regularization coefficient. Indeed as with all inverse problems, the identification of material properties is ill-posed and should be regularized. In this contribution, a simple Tikonov regularization is considered and consists in adding a penalization on the distance between the considered material parameters p and the reference parameters denoted by p^{0}. The same discretization is used along the tangential direction for both the *QuadWire* model and the 3D model, but of course, several elements along $\boldsymbol{n}$ and $\boldsymbol{b}$ directions are necessary for the 3D model.

The optimization problem (63) is solved by using an adaptive-step gradient algorithm. The gradient of the objective function $J(p)$ is derived in Appendix E by using adjoint techniques. We rely on a multiple-load optimization procedure, meaning that a total of 12 independent and identical beads are considered simultaneously with various loading conditions. Instead of summing 12 objective functions, we rather add successively the 12 beads in a single curve, and the length l in the integration of (64) is 12 times the length of a single bead. Each bead length is set to $l = 2$ mm and a square section is considered with $\delta n = 0.1$ mm and $\delta b = 0.1$ mm. The 3D model is meshed using 10 elements along $\boldsymbol{n}$ and $\boldsymbol{b}$ (i.e., 100 elements for the cross-section) and 200 elements along $\boldsymbol{t}$ to obtain cubic elements (i.e., 20000 elements in total for each bead). The *QuadWire* is also discretized with $N_{\mathrm{e}} = 200$ elements for each bead so that no interpolation is necessitated to compare with the 3D simulations. Boundary conditions only consist in clamping displacements at one end of each bead. The 12 loading conditions consist in applying successively one of the 3 components of the 4 external forces per unit length $(\boldsymbol{f}^{\mathrm{ext}}, \boldsymbol{m}_{n}^{\mathrm{ext}}, \boldsymbol{m}_{b}^{\mathrm{ext}}, \boldsymbol{m}_{\times}^{\mathrm{ext}})$ defined in (30). Each bead is loaded with a single, uniform and normalized component of the external forces such that the free energy per unit length is comparable for the 12 beads (i.e., each bead has the same weight in the minimization procedure). The regularization coefficient ϵ has been classically determined by using an L-curve strategy [31]. The Young modulus of the 3D model is

set to $E = 3000$ (MPa) and the Poisson coefficient is $\nu = 0.3$, which corresponds to PLA. On this basis the optimized stiffness parameters $p^\dagger$ is determined and listed in table C.1 and C.2.

The free energy per unit length is presented in figure 4 for the 12 beads to emphasize the effect of the optimization. It is clear that the optimized stiffness parameters $p^\dagger$ enable to satisfyingly fit the free energy per unit length computed with the conventional 3D model. The homogenized stiffness components p^0 led to significantly overestimate (resp. underestimate) the free energy for the components $\boldsymbol{m}_\times^{\text{ext}}.\boldsymbol{t}$, $\boldsymbol{m}_\times^{\text{ext}}.\boldsymbol{n}$ and $\boldsymbol{m}_\times^{\text{ext}}.\boldsymbol{b}$ (resp. $\boldsymbol{m}_n^{\text{ext}}.\boldsymbol{t}, \boldsymbol{m}_b^{\text{ext}}.\boldsymbol{t}, \boldsymbol{f}^{\text{ext}}.\boldsymbol{n}, \boldsymbol{m}_b^{\text{ext}}.\boldsymbol{n}, \boldsymbol{f}^{\text{ext}}.\boldsymbol{b}$, and $\boldsymbol{m}_n^{\text{ext}}.\boldsymbol{b}$) of the applied forces, which demonstrates the necessity of the optimization procedure and the deviation of the real bead from 3D hexahedron elements. However, for the components $\boldsymbol{f}^{\text{ext}}.\boldsymbol{t}, \boldsymbol{m}_n^{\text{ext}}.\boldsymbol{n}, \boldsymbol{m}_b^{\text{ext}}.\boldsymbol{b}$ of the applied stress, the homogenized stiffness parameters p^0 already enabled to perfectly fit the reference free energy (i.e., computed using conventional 3D approach). This is due to the fact that a square cross-section has been considered for the bead, as in the crude homogenization procedure providing p^0. However, it should be emphasized that different shapes can be considered in the optimization procedure according to the real bead geometry.

The optimization validity is addressed by comparing the free energy per unit length of a thin-walled structure undergoing thermal change of the form $\Delta T(s) = a \times (s/l)$ with $a = -60$ K computed with the *QuadWire* approach and a conventional 3D approach. Boundary conditions consist in clamping bottom particles of the first layer (i.e., particles 2 and 4 corresponding to the attachment with the substrate). A sinusoidal geometry is considered to address the effect of varying curvature. The free energy per unit length is presented in figure 5. An excellent fit is observed between the *QuadWire* model and the conventional 3D approach, which validates the optimized stiffness parameters. It should be noted that excellent results are also obtained for different geometries and applied thermal changes.

6. Application to fused deposition modeling

An essential aspect of additive manufacturing (AM) modeling is the addition of matter during fabrication. Elements are either added progressively to extend the initial mesh at every time step (i.e., *element-birth technique* for which implementation requires solver initialization and equation renumbering but can be faster due to smaller mesh at initialization), or future elements are given a nearly null stiffness until they are *activated* with their given stiffness when their respective time-step is reached (i.e., *quiet/active* method which is easier to implement but can be computationally expensive). *Hybrid activation* methods offer a twofold advantage by dealing with the current layer based on *quiet/active* methods, while future layers are added when necessary using *element-birth technique* [11, 12].

In this paper, a *quiet/active* method is used to simulate fused deposition modeling (FDM) of polylactide (PLA) under conditions extracted from [32]. A thermo-elastic behavior is usually considered for this combination of process and material. Glass transition of PLA is set to $T_g = 328.15$ K, and the Young modulus is more or less constant for temperatures lower than T_g and set to $E = 3000$ MPa, and negligible for higher temperatures, while the Poisson coefficient is set to $\nu = 0.3$. It should be noted that the optimized behavior derived in Section 5 corresponds to temperatures lower than T_g. Elements are activated during cooling when their temperature reaches T_g. The build platform temperature is maintained constant during the entire fabrication at

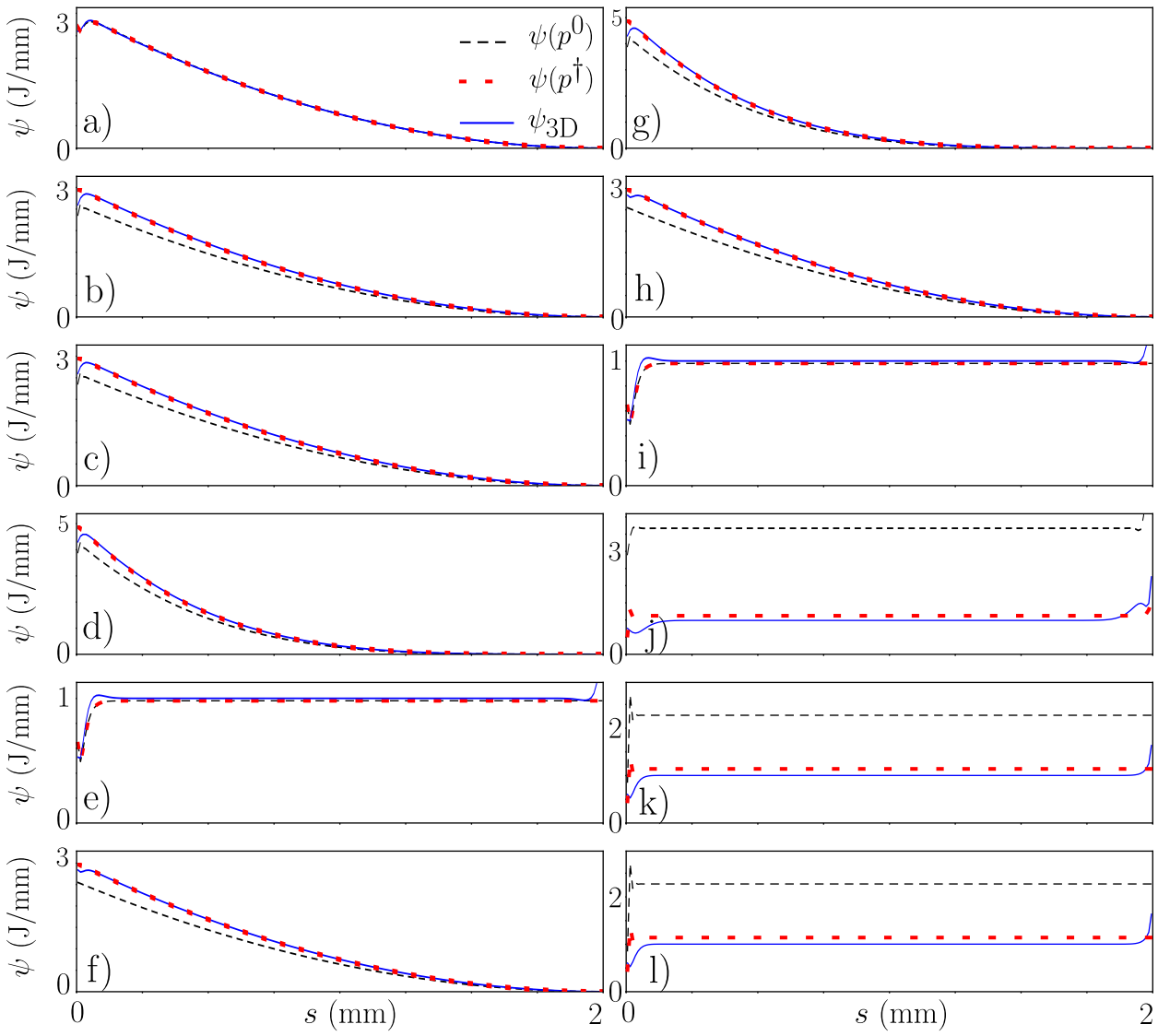

Figure 4: Normalized free energy per unit length along the 12 beads for the reference 3D computation, the initial stiffness parameters p^0, and the optimized stiffness parameters $p^\dagger$. The activated component of external forces are a) $\boldsymbol{f}^{\text{ext}}.\boldsymbol{t}$, b) $\boldsymbol{m}_n^{\text{ext}}.\boldsymbol{t}$, c) $\boldsymbol{m}_b^{\text{ext}}.\boldsymbol{t}$, d) $\boldsymbol{f}^{\text{ext}}\boldsymbol{n}$, e) $\boldsymbol{m}_n^{\text{ext}}.\boldsymbol{n}$, f) $\boldsymbol{m}_b^{\text{ext}}.\boldsymbol{n}$, g) $\boldsymbol{f}^{\text{ext}}.\boldsymbol{b}$, h) $\boldsymbol{m}_n^{\text{ext}}.\boldsymbol{b}$, i) $\boldsymbol{m}_b^{\text{ext}}.\boldsymbol{b}$, j) $\boldsymbol{m}_\times^{\text{ext}}.\boldsymbol{t}$, k) $\boldsymbol{m}_\times^{\text{ext}}.\boldsymbol{n}$, l) $\boldsymbol{m}_\times^{\text{ext}}.\boldsymbol{b}$, where the interpretation of the internal forces is depicted in figure 2.

$T_{\text{pla}} = 323.15$ K, and final cooling of the entire structure (i.e., part+build platform) is considered at the end of fabrication. In addition, the deposition temperature of the filament is $T_{\text{dep}} = 353.15$ K. The filament is cooled down by the surrounding air (resp. the build platform), and the heat transfer coefficient is set to $h_{\text{air}} = 3.96$ W.m^{-2}.K^{-1} (resp. $h_{\text{pla}} = 500$ W.m^{-2}.K^{-1}). Thermal properties are assumed to be temperature independent, and the thermal conductivity is $k = 0.197$ W.m^{-1}.K^{-1} while the specific heat is $c_p = 1590$ J.kg^{-1}.K^{-1}. In addition, the density is $\rho_{3D} = 1250$ kg.m^{-3} and the thermal expansion coefficient is $\alpha = 11.3 \times 10^{-6}$ K^{-1}. A total of 15 beads with a length of $l = 50$ mm are printed with a printing speed set to $v = 25$ mm.s^{-1}. Two different structures are

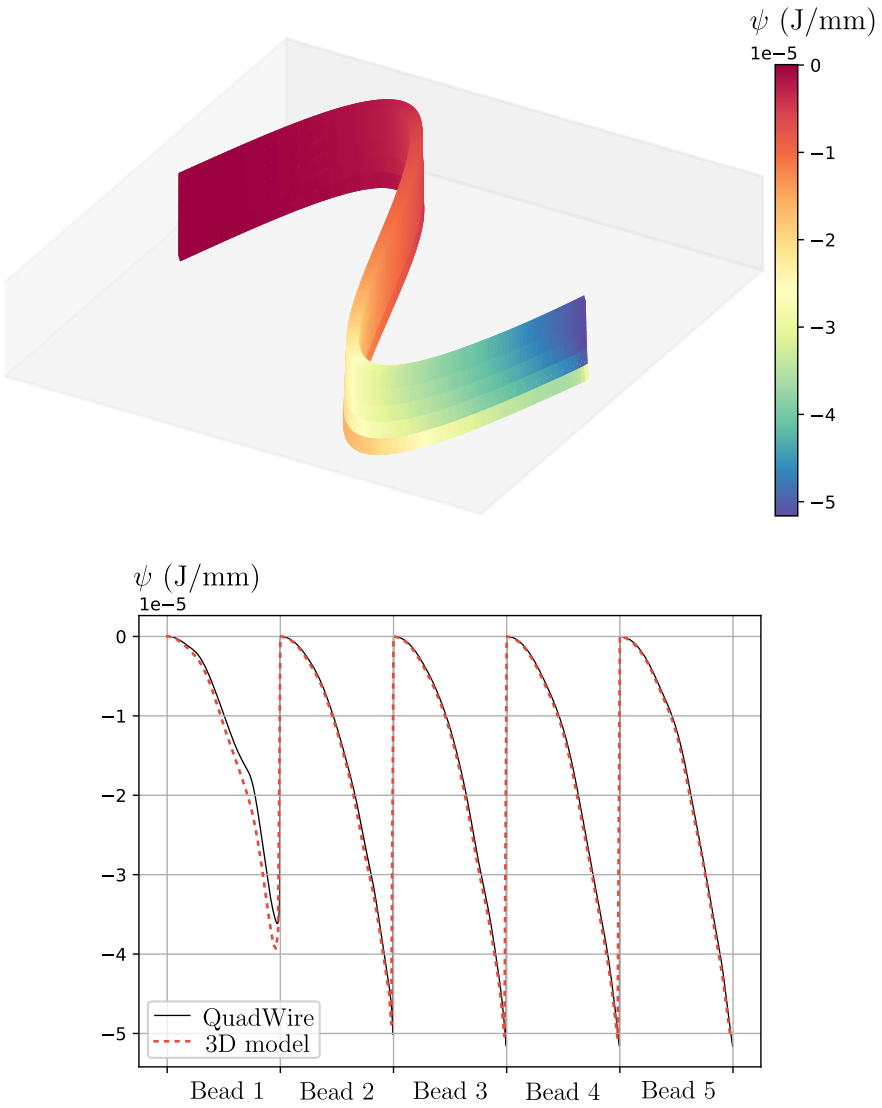

Figure 5: Color map of the free energy per unit length on the sinusoidal structure computed with the *QuadWire* model (top) and comparison for each layer between the *QuadWire* and the 3D model (bottom). Negative values are obtained for ψ as the quadratic term in ΔT has been omitted in its definition.

simulated, 1) a thin-walled structure for which beads are deposited on top of each other, and 2) a "carpet" structure for which all the beads are deposited on the build platform next to each other. A schematic view of the two different structures is presented in figure 6.

Temperature kinetics is computed by using the fast approach [2], and is presented in figure 7 for the thin-walled structure and in figure 8 for the "carpet" structure, which is obtained by switching the role of the surrounding air and the build platform. Results are very consistent with the measurements reported in [32]. Temperature change ΔT is therefore computed by considering the glass transition T_g as the reference temperature (i.e., $\Delta T = T - T_g$). No other eigenstrain is considered as polymerization occurs at higher temperature than T_g.

On this basis, mechanical computations are carried out for both the thin-walled and the "carpet"

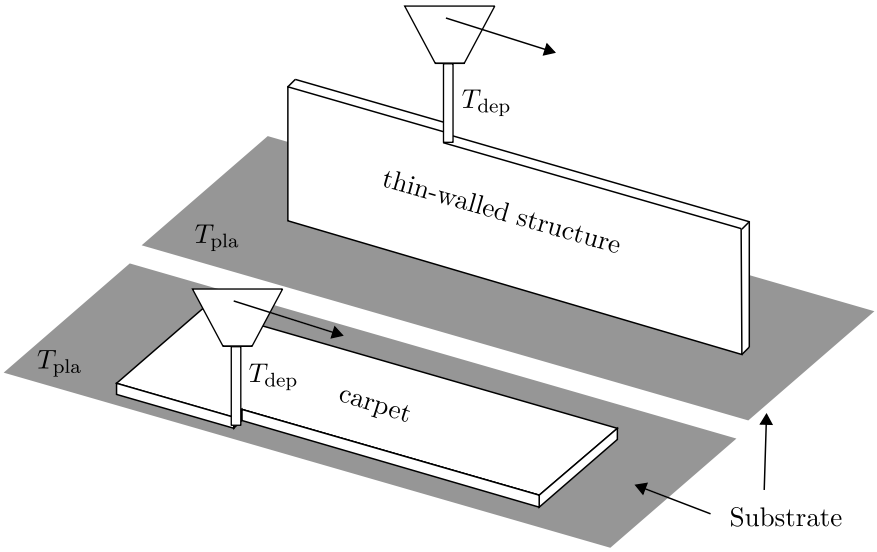

Figure 6: Schematic view of the FDM process for the thin-walled structure and the carpet.

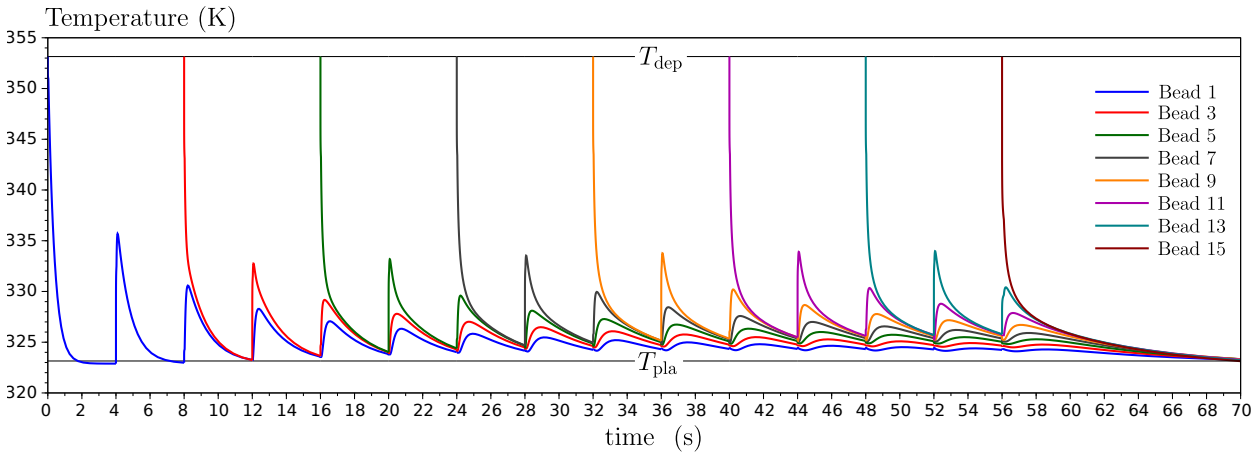

Figure 7: Temperature kinetics for the thin-walled structure, only odd beads are depicted for the sake of readability.

structures, with $N_{\text{e}} = 50$ elements for each bead and by clamping particles 2 and 4 (i.e., bottom particles) for all nodes in contact with the substrate. Computation time is around 3 minutes with a laptop for *QuadWire* simulations, whereas 3.7 hours are reported in [32] for an equivalent conventional 3D computation using the commercial software COMSOL multiphysics.

Generalized stress tensors $\boldsymbol{\Sigma}$ and $\boldsymbol{M}$ are computed, and to facilitate their interpretation internal forces per unit length $\boldsymbol{f}_k$ and internal forces $\boldsymbol{F}_k$ (where $1 \leq k \leq 4$) are also computed using (19), (20) and (17). Even though the model can be derived without any reference to the Cauchy model in 3D, $\boldsymbol{f}_k$ and $\boldsymbol{F}_k$ can be related to a conventional 3D stress tensor denoted by $\boldsymbol{\sigma}$. Indeed, based on the interpretation of internal forces given in (16) and the bead cross-section divided into 4 sectors denoted by S_k ($1 \leq k \leq 4$) as depicted in figure 9, the average of $\sigma_{tt}, \sigma_{tn}, \sigma_{tb}$ over each sector S_k

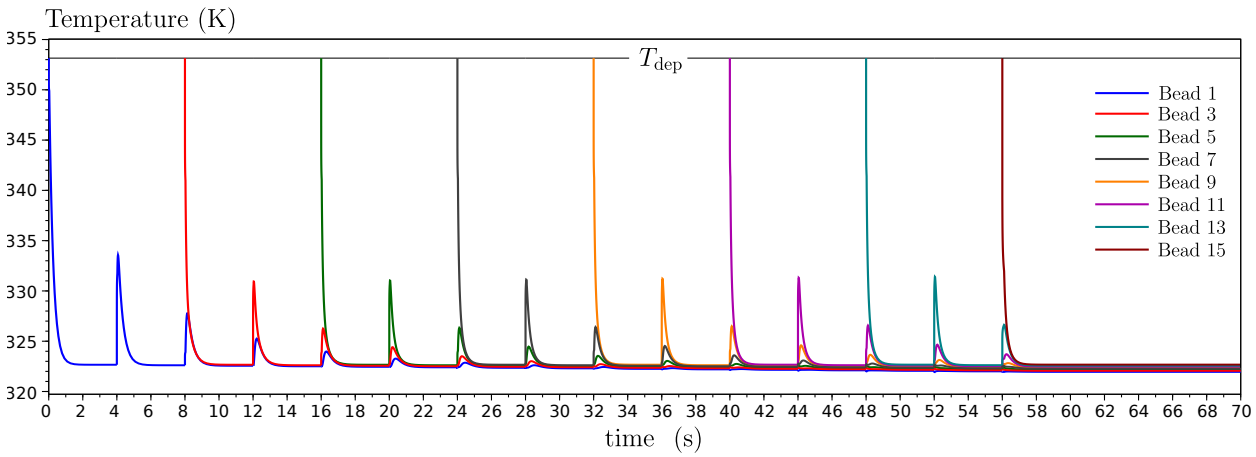

Figure 8: Temperature kinetics for the "carpet" structure, only odd beads are depicted for the sake of readability.

reads:

$$\langle \boldsymbol{\sigma}.\boldsymbol{t} \rangle_{S_k} = \frac{\boldsymbol{F}_k(s)}{|S_k|} \tag{65}$$

And the average of the interface stress $\boldsymbol{\sigma}.\boldsymbol{n}_k$ (where $\boldsymbol{n}_k$ is the outer normal vector) over each sector outer boundary (abusively denoted by ∂S_k) reads:

$$\langle \boldsymbol{\sigma}.\boldsymbol{n}_k \rangle_{\partial S_k} = \frac{\boldsymbol{f}_k(s)}{|\partial S_k|} \tag{66}$$

Tension and shear stress are presented in figure 10 for the thin-walled structure, and in figure 11

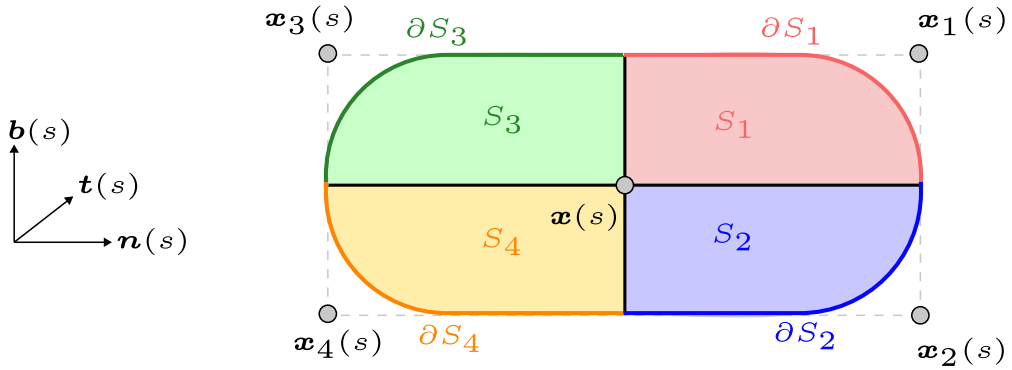

Figure 9: Simplified representation of the bead section to compute a 3D Cauchy stress tensor.

for the "carpet" structure. Stress distribution is similar to numerical results obtained for another material in [11], and quantitatively consistent with [32]. The effect of clamping bottom particles on the substrate is clearly demonstrated as significant tension stress evolution can be noticed for the thin-walled structure due to the edge effect, while more uniform tension stress distribution is observed for the "carpet" structure, which is much more constrained by the substrate. Similarly, significant shear stress is observed for the thin-walled structure in order to accommodate the tension

evolution near the edges (i.e., the equilibrium), whereas the shear stress is lower by several orders of magnitude for the "carpet" structure as the tension stress is almost uniform.

In addition, the *QuadWire* model provides details on stress distribution in the cross-section. For instance for the thin-walled structure, even though the averaged shear stress σ_{tn} over the bead cross-section is 0 for symmetry reasons, one can obtain the stress in each sector S_k by directly using (65). The shear stress σ_{tn} in sector S_1 is presented for different beads in figure 12. Very similar result is obtained for sector S_2 and opposite values are obtained for sectors S_3 and S_4. Therefore by using (65) and (66), the *QuadWire* model provides rather detailed information about the 3D Cauchy stress tensor distribution along both the tangential direction and in the cross-section. Stresses (65) enable to capture defects such as buckling, while interface stresses (66) enable to capture defects associated with delamination between beads.

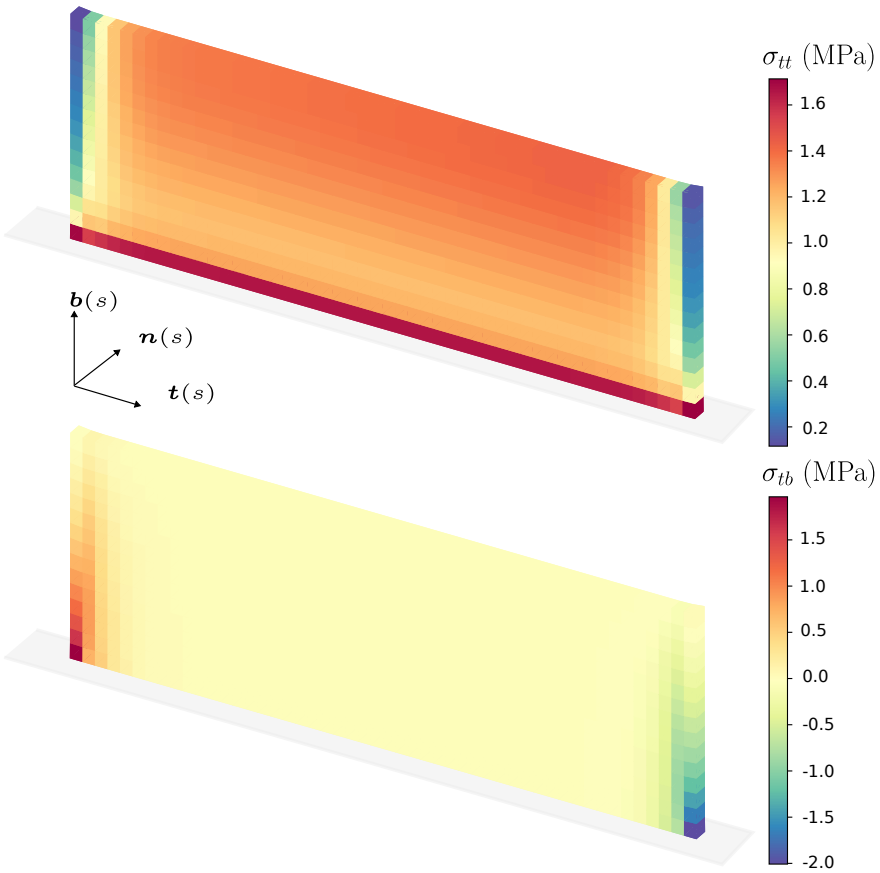

Figure 10: 3D stress computed from (65) averaged over the four sectors S_k $(1 \leq k \leq 4)$ for the thin-walled structure.

7. Conclusion

Most additive manufacturing processes involve the juxtaposition of elongated beads to form 3D solid parts. Conventional simulation tools to capture stress and displacement evolution during and after fabrication are essential but strongly limited by excessive computation cost. The key

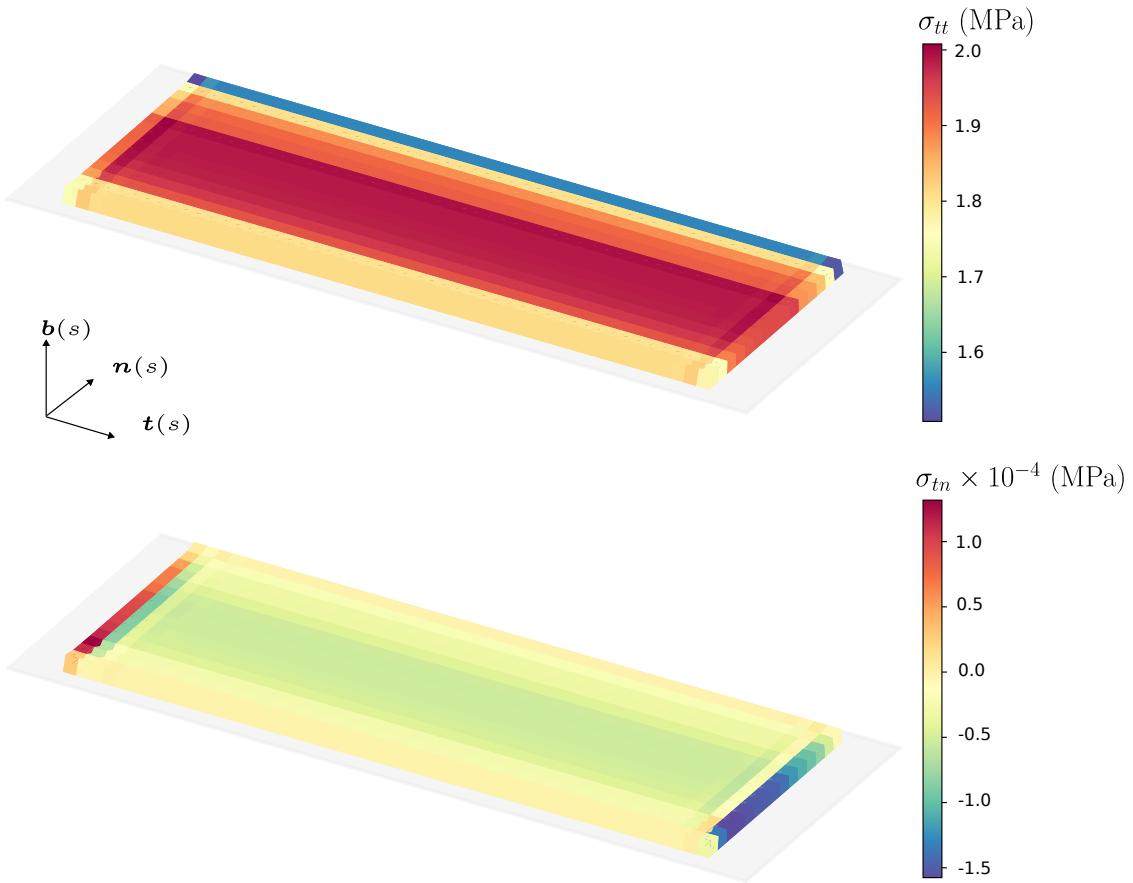

Figure 11: 3D stress computed from (65) averaged over the four sectors S_k ($1 \leq k \leq 4$) for the "carpet" structure.

contribution of this paper is the development of a mechanical model called *QuadWire* enabling to reduce the total number of degrees of freedom by several orders of magnitude for large parts, without compromising accuracy or limiting too much the level of detail that can be obtained from numerical simulations. The *QuadWire* model is one-dimensional with 4 particles (i.e., 12 degrees of freedom per material point), which enables to easily set kinematic relations between different beads and therefore assemble a 3D solid part.

The computation cost reduction relies on the fact that conventional 3D approaches necessitate at least 3 to 4 elements across the bead section, which results in fine discretization along the tangential direction to avoid conditioning issues, and therefore very fine mesh of the entire 3D part; whereas the bead height and thickness are internal dimensions in the *QuadWire* model so that the mesh along the tangential direction can be much coarser. A finite element analysis has been implemented in Python, and numerical results are in excellent agreement with conventional 3D computations with very fine mesh. Fused deposition modeling of polylactide (PLA) has been simulated under different process conditions, and results are very similar to the existing literature while significantly reducing computation time (by a factor of 70 for the studied examples). It should be noted that performances can be further improved by using a compiled language for numerical implementation. It should be noted that unlike *inherent strain* approaches, the proposed work does

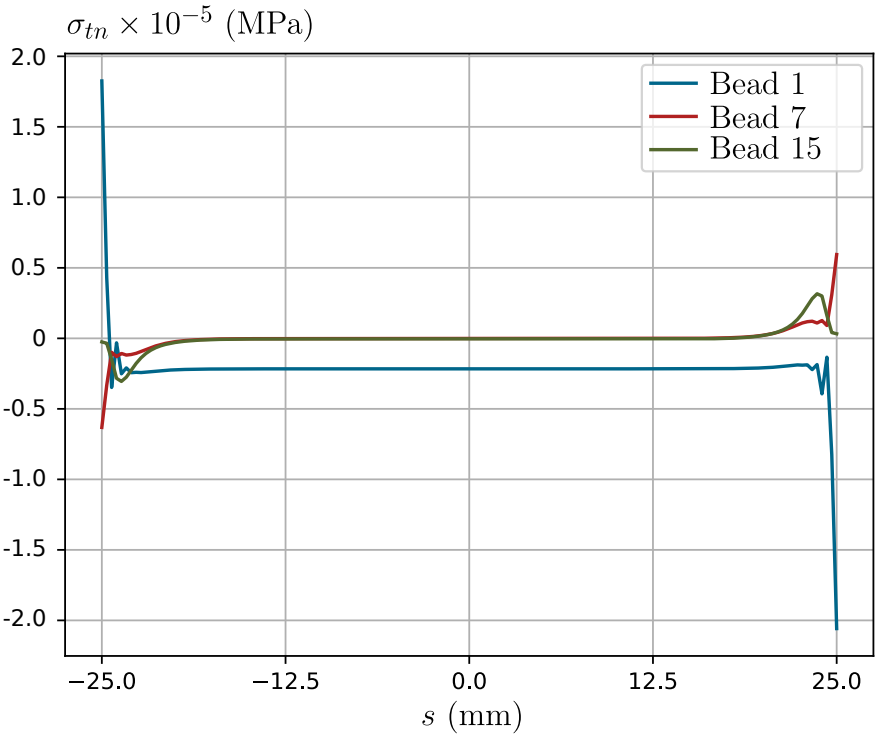

Figure 12: 3D stress computed from (65) in sector S_1 for the thin-walled structure.

not rely on previously detailed 3D computations of the process, and can be directly applied to any set of process parameters and part geometry.

This work opens interesting perspectives for numerical simulations of bead-based fabrication processes such as most additive manufacturing processes, as it holds substantial potential for computation cost reduction. Optimization strategies and real-time control (based on neural networks relying on large databases) are therefore more accessible. Future work will focus on implementing non-linear behavior in the *QuadWire* model.

Funding. : This work was supported by the French National Centre for Scientific Research (CNRS) for project OPAC (MITI 80|PRIME).

Appendix A. First and second gradient definition

In this section, first and second order gradients of the *QuadWire* model are defined in the deformed configuration. It should be emphasized that since there are 4 particles defined along a continuous and differentiable direction (i.e., curvilinear abscissa denoted by s), one should consider a mixture of finite differences to account for relative movements between particles for a given s, and proper differentiation to account for deformation along the s direction.

The generalized velocity field reads $\overrightarrow{\boldsymbol{v}}(s) = (\boldsymbol{v}_1(s), \boldsymbol{v}_2(s), \boldsymbol{v}_3(s), \boldsymbol{v}_4(s))$. The gradient along the $\boldsymbol{t}$ direction corresponds to a differentiation of the average displacement $\boldsymbol{v}(s)$ with respect to s:

$$\overrightarrow{\boldsymbol{\nabla}}\,\overrightarrow{\boldsymbol{v}}(s).\boldsymbol{t}(s) = \boldsymbol{v}'(s) \tag{A.1}$$

In addition, the *QuadWire* gradient along $\boldsymbol{n}$ and $\boldsymbol{b}$ is defined by considering directional finite differences. To do so, consider the 4 midpoints:

$$\begin{cases} \boldsymbol{y}_{12}(s) = \dfrac{1}{2}\left(\boldsymbol{x}_1(s) + \boldsymbol{x}_2(s)\right) = \boldsymbol{x}(s) + \dfrac{\delta n}{2}\,\boldsymbol{n}(s) \\ \boldsymbol{y}_{13}(s) = \dfrac{1}{2}\left(\boldsymbol{x}_1(s) + \boldsymbol{x}_3(s)\right) = \boldsymbol{x}(s) + \dfrac{\delta b}{2}\,\boldsymbol{b}(s) \\ \boldsymbol{y}_{24}(s) = \dfrac{1}{2}\left(\boldsymbol{x}_2(s) + \boldsymbol{x}_4(s)\right) = \boldsymbol{x}(s) - \dfrac{\delta b}{2}\,\boldsymbol{b}(s) \\ \boldsymbol{y}_{34}(s) = \dfrac{1}{2}\left(\boldsymbol{x}_3(s) + \boldsymbol{x}_4(s)\right) = \boldsymbol{x}(s) - \dfrac{\delta n}{2}\,\boldsymbol{n}(s) \end{cases} \tag{A.2}$$

It should be noted that δn and δb characterize the bead size in the reference configuration, but since relative motions between particles are small, δn and δb are also used in the deformed configuration. Using the operator defined in (22), and the average displacements at the midpoint, the directional finite difference along $\boldsymbol{n}$ reads:

$$\overrightarrow{\boldsymbol{\nabla}}\,\overrightarrow{\boldsymbol{v}}(s).\boldsymbol{n}(s) = \frac{\left(\dfrac{\boldsymbol{v}_1(s) + \boldsymbol{v}_2(s)}{2}\right) - \left(\dfrac{\boldsymbol{v}_3(s) + \boldsymbol{v}_4(s)}{2}\right)}{\delta n} = \frac{\delta^n \boldsymbol{v}(s)}{\delta n} \tag{A.3}$$

And the directional finite difference along $\boldsymbol{b}$ reads:

$$\overrightarrow{\boldsymbol{\nabla}}\,\overrightarrow{\boldsymbol{v}}(s).\boldsymbol{b}(s) = \frac{\left(\dfrac{\boldsymbol{v}_1(s) + \boldsymbol{v}_3(s)}{2}\right) - \left(\dfrac{\boldsymbol{v}_2(s) + \boldsymbol{v}_4(s)}{2}\right)}{\delta b} = \frac{\delta^b \boldsymbol{v}(s)}{\delta b} \tag{A.4}$$

Hence the first order gradient definition:

$$\overrightarrow{\boldsymbol{\nabla}}\,\overrightarrow{\boldsymbol{v}}(s) = \boldsymbol{v}'(s) \otimes \boldsymbol{t}(s) + \frac{\delta^n \boldsymbol{v}(s)}{\delta n} \otimes \boldsymbol{n}(s) + \frac{\delta^b \boldsymbol{v}(s)}{\delta b} \otimes \boldsymbol{b}(s) \tag{A.5}$$

The second order gradient along $\boldsymbol{t}$ is obtained by considering the differentiation of the first order gradient (A.5) with respect to s which reads:

$$\begin{aligned} \overrightarrow{\boldsymbol{\nabla}}\left[\overrightarrow{\boldsymbol{\nabla}}\,\overrightarrow{\boldsymbol{v}}\right].\boldsymbol{t}(s) \quad &= \boldsymbol{v}''(s) \otimes \boldsymbol{t}(s) + \frac{\delta^n \boldsymbol{v}'(s)}{\delta n} \otimes \boldsymbol{n}(s) + \frac{\delta^b \boldsymbol{v}'(s)}{\delta b} \otimes \boldsymbol{b}(s) \\ &+ \boldsymbol{v}'(s) \otimes \boldsymbol{t}'(s) + \frac{\delta^n \boldsymbol{v}(s)}{\delta n} \otimes \boldsymbol{n}'(s) + \frac{\delta^b \boldsymbol{v}(s)}{\delta b} \otimes \boldsymbol{b}'(s) \end{aligned} \tag{A.6}$$

In addition local tensors of finite differences are considered at the 4 midpoints $\boldsymbol{y}_{12}, \boldsymbol{y}_{13}, \boldsymbol{y}_{24}, \boldsymbol{y}_{34}$, and using the operator defined in (22), the second order gradient along $\boldsymbol{n}$ and $\boldsymbol{b}$ is therefore defined as the following finite differences:

$$\overrightarrow{\boldsymbol{\nabla}}\left[\overrightarrow{\boldsymbol{\nabla}}\,\overrightarrow{\boldsymbol{v}}\right].\boldsymbol{n}(s) = \frac{\left(\frac{\boldsymbol{v}_1-\boldsymbol{v}_2}{\delta b}\right)\otimes\boldsymbol{b}(s) - \left(\frac{\boldsymbol{v}_3-\boldsymbol{v}_4}{\delta b}\right)\otimes\boldsymbol{b}(s)}{\delta n} = \frac{\delta^{\times}\boldsymbol{u}(s)}{\delta n\delta b}\otimes\boldsymbol{b}(s) \tag{A.7}$$

$$\overrightarrow{\boldsymbol{\nabla}}\left[\overrightarrow{\boldsymbol{\nabla}}\,\overrightarrow{\boldsymbol{v}}\right].\boldsymbol{b}(s) = \frac{\left(\frac{\boldsymbol{v}_1-\boldsymbol{v}_3}{\delta n}\right)\otimes\boldsymbol{n}(s) - \left(\frac{\boldsymbol{v}_2-\boldsymbol{v}_4}{\delta n}\right)\otimes\boldsymbol{n}(s)}{\delta b} = \frac{\delta^{\times}\boldsymbol{v}(s)}{\delta n\delta b}\otimes\boldsymbol{n}(s) \tag{A.8}$$

Hence the second order gradient for the *QuadWire* model is defined as follows:

$$\begin{aligned}\overrightarrow{\boldsymbol{\nabla}}\left[\overrightarrow{\boldsymbol{\nabla}}\,\overrightarrow{\boldsymbol{v}}\right] &= \boldsymbol{v}''(s)\otimes\boldsymbol{t}(s)\otimes\boldsymbol{t}(s) + \frac{\delta^n\boldsymbol{v}'(s)}{\delta n}\otimes\boldsymbol{n}(s)\otimes\boldsymbol{t}(s) + \frac{\delta^b\boldsymbol{v}'(s)}{\delta b}\otimes\boldsymbol{b}(s)\otimes\boldsymbol{t}(s)\\ &+\boldsymbol{v}'(s)\otimes\boldsymbol{t}'(s)\otimes\boldsymbol{t}(s) + \frac{\delta^n\boldsymbol{v}(s)}{\delta n}\otimes\boldsymbol{n}'(s)\otimes\boldsymbol{t}(s) + \frac{\delta^b\boldsymbol{v}(s)}{\delta b}\otimes\boldsymbol{b}'(s)\otimes\boldsymbol{t}(s)\\ &+\frac{\delta^{\times}\boldsymbol{v}(s)}{\delta n\delta b}\otimes(\boldsymbol{b}(s)\otimes\boldsymbol{n}(s)+\boldsymbol{n}(s)\otimes\boldsymbol{b}(s))\end{aligned} \tag{A.9}$$

It should be noted that this definition of the second order gradient (A.9) is too rich when compared to the corresponding dual generalized stress $\boldsymbol{M}$ defined in (20). Therefore, all the components of the second order gradient (A.9) which are vanishing in $\overrightarrow{\boldsymbol{\nabla}}\left[\overrightarrow{\boldsymbol{\nabla}}\,\overrightarrow{\boldsymbol{u}}\right]\vdots\boldsymbol{M}$ are removed to define the rate of deformation $\boldsymbol{d}_{\chi}$ leading to the definition (26).

Appendix B. Balance equations and boundary conditions

The balance and boundary conditions are derived from the weak form (31). Integration by parts leads to the equilibrium equations of the *QuadWire* model:

$$\begin{cases}\boldsymbol{f}^{\text{ext}}(s) + (\boldsymbol{\Sigma}.\boldsymbol{t})'(s) &= 0\\ \boldsymbol{m}_n^{\text{ext}}(s) + (\boldsymbol{n}(s)\otimes\boldsymbol{t}(s)):\boldsymbol{M}'(s) - \boldsymbol{\Sigma}(s).\boldsymbol{n}(s) &= 0\\ \boldsymbol{m}_b^{\text{ext}}(s) + (\boldsymbol{b}(s)\otimes\boldsymbol{t}(s)):\boldsymbol{M}'(s) - \boldsymbol{\Sigma}(s).\boldsymbol{b}(s) &= 0\\ \boldsymbol{m}_{\times}^{\text{ext}}(s) + \boldsymbol{M}'_{\times}(s) - \boldsymbol{M}(s):(\boldsymbol{b}(s)\otimes\boldsymbol{n}(s)+\boldsymbol{n}(s)\otimes\boldsymbol{b}(s)) &= 0\end{cases} \tag{B.1}$$

The boundary conditions are given by:

$$\begin{cases}\boldsymbol{\Sigma}(s).\boldsymbol{N}(s) &= \boldsymbol{F}^{\text{ext}}(s)\\ (\boldsymbol{n}(s)\otimes\boldsymbol{N}(s)):\boldsymbol{M}(s) &= \boldsymbol{M}_n^{\text{ext}}(s)\\ (\boldsymbol{b}(s)\otimes\boldsymbol{N}(s)):\boldsymbol{M}(s) &= \boldsymbol{M}_b^{\text{ext}}(s)\\ (\boldsymbol{t}(s).\boldsymbol{N}(s))\,\boldsymbol{M}_{\times}(s) &= \boldsymbol{M}_{\times}^{\text{ext}}(s)\end{cases} \tag{B.2}$$

where $\boldsymbol{N}(s)$ is the outgoing normal to the domain (i.e., for $s=0, \boldsymbol{N}(s)=-\boldsymbol{t}(s)$ and for $s=l, \boldsymbol{N}(s)=\boldsymbol{t}(s)$).

Appendix C. Crude homogenization procedure to regularize stiffness identification

In the following, the Helmholtz free energy per unit length is simply homogenized by assuming linear interpolation of displacements for a bead with a square cross-section under infinitesimal strain assumption. Of course, this homogenization leads to identifying the *QuadWire* model as a simple single hexahedron element in 3D, which is not the aim of the proposed work. But this homogenization is only meant to reduce the total number of stiffness components involved in the *QuadWire* model and provide a reasonable initial guess for the optimization (63). The initial curvature is neglected (i.e., $\boldsymbol{t}'(s) = \boldsymbol{n}'(s) = \boldsymbol{b}'(s) = 0$), which is consistent with linear FEA. For each material point of *QuadWire* consider the following hexahedron RVE in 3D denoted by Ω_s:

$$\Omega_s = \left\{ (x_t, x_n x_b) \in \left(s - \frac{l_c}{2}, s + \frac{l_c}{2} \right) \times \left(-\frac{\delta n}{2}, \frac{\delta n}{2} \right) \times \left(-\frac{\delta b}{2}, \frac{\delta b}{2} \right) \right\} \tag{C.1}$$

where l_c (m) is a characteristic length, which can be assimilated to the element mesh size in FEA.

The 3D displacement field is depicted for each strain component in figures C.13, C.14 and C.15. For second and third order gradient components, the 3D displacement field is not uniform in Ω_s. Consider the 3D displacement field denoted by $\boldsymbol{U}_{3\mathrm{D}}$ which reads:

$$\begin{aligned}
\boldsymbol{U}_{3\mathrm{D}}(x_t, x_n, x_b) \;=\; & \Big(u_t'\,(x_t - s) + \tfrac{\delta^n u_t}{\delta n}\, x_n + \tfrac{\delta^b u_t}{\delta b}\, x_b + \tfrac{\delta^\times u_t}{\delta n\, \delta b}\, x_n\, x_b \\
& + \tfrac{\delta^n u_t'}{\delta n}\, x_n\,(x_t - s) + \tfrac{\delta^b u_t'}{\delta b}\, x_b\,(x_t - s) + \tfrac{\delta^\times u_t'}{\delta n\, \delta b}(x_t - s)\, x_n\, x_b \Big)\, \boldsymbol{t} \\
& + \Big(u_n'\,(x_t - s) + \tfrac{\delta^n u_n}{\delta n}\, x_n + \tfrac{\delta^b u_n}{\delta b}\, x_b + \tfrac{\delta^\times u_n}{\delta n\, \delta b}\, x_n\, x_b \\
& + \tfrac{\delta^n u_n'}{\delta n}\, x_n\,(x_t - s) + \tfrac{\delta^b u_n'}{\delta b}\, x_b\,(x_t - s) + \tfrac{\delta^\times u_n'}{\delta n\, \delta b}(x_t - s)\, x_n\, x_b \Big)\, \boldsymbol{n} \\
& + \Big(u_b'\,(x_t - s) + \tfrac{\delta^n u_b}{\delta n}\, x_n + \tfrac{\delta^b u_b}{\delta b}\, x_b + \tfrac{\delta^\times u_b}{\delta n\, \delta b}\, x_n\, x_b \\
& + \tfrac{\delta^n u_b'}{\delta n}\, x_n\,(x_t - s) + \tfrac{\delta^b u_b'}{\delta b}\, x_b\,(x_t - s) + \tfrac{\delta^\times u_b'}{\delta n\, \delta b}(x_t - s)\, x_n\, x_b \Big)\, \boldsymbol{b}
\end{aligned} \tag{C.2}$$

Thus, using (24), (26) and (27) the 3D strain denoted by $\boldsymbol{\varepsilon}$ reads:

$$\begin{aligned}
\boldsymbol{\varepsilon}(x_t, x_n, x_b) = \; & (\boldsymbol{t} \otimes \boldsymbol{t})\, (\xi_{tt} + \chi_{tnt}\, x_n + \chi_{tbt}\, x_b + \gamma_t\, x_n\, x_b) \\
& + (\boldsymbol{n} \otimes \boldsymbol{n})\, (\xi_{nn} + \chi_{nnb}\, x_b + \chi_{nnt}\,(x_t - s) + \gamma_n\,(x_t - s)\, x_b) \\
& + (\boldsymbol{b} \otimes \boldsymbol{b})\, (\xi_{bb} + \chi_{bnb}\, x_n + \chi_{bbt}\,(x_t - s) + \gamma_b\,(x_t - s)\, x_n) \\
& + \frac{1}{2}\,(\boldsymbol{t} \otimes \boldsymbol{n} + \boldsymbol{n} \otimes \boldsymbol{t})\, (2\xi_{tn} + (\chi_{nbt} + \chi_{tnb})\, x_b + \chi_{tnt}\,(x_t - s) + \chi_{nnt}\, x_n \\
& + \gamma_t\,(x_t - s)\, x_b + \gamma_n\, x_n\, x_b) \\
& + \frac{1}{2}\,(\boldsymbol{t} \otimes \boldsymbol{b} + \boldsymbol{b} \otimes \boldsymbol{t})\, (2\xi_{tb} + (\chi_{tnb} + \chi_{bnt})\, x_n + \chi_{tbt}\,(x_t - s) + \chi_{bbt}\, x_b \\
& + \gamma_t\,(x_t - s) x_n + \gamma_b\, x_n\, x_b) \\
& + \frac{1}{2}\,(\boldsymbol{n} \otimes \boldsymbol{b} + \boldsymbol{b} \otimes \boldsymbol{n})\, (2\xi_{nb} + \chi_{nnb}\, x_n + (\chi_{nbt} + \chi_{bnt})\,(x_t - s) + \chi_{bnb}\, x_b \\
& + \gamma_n\,(x_t - s)\, x_n + \gamma_b\,(x_t - s)\, x_b)
\end{aligned} \tag{C.3}$$

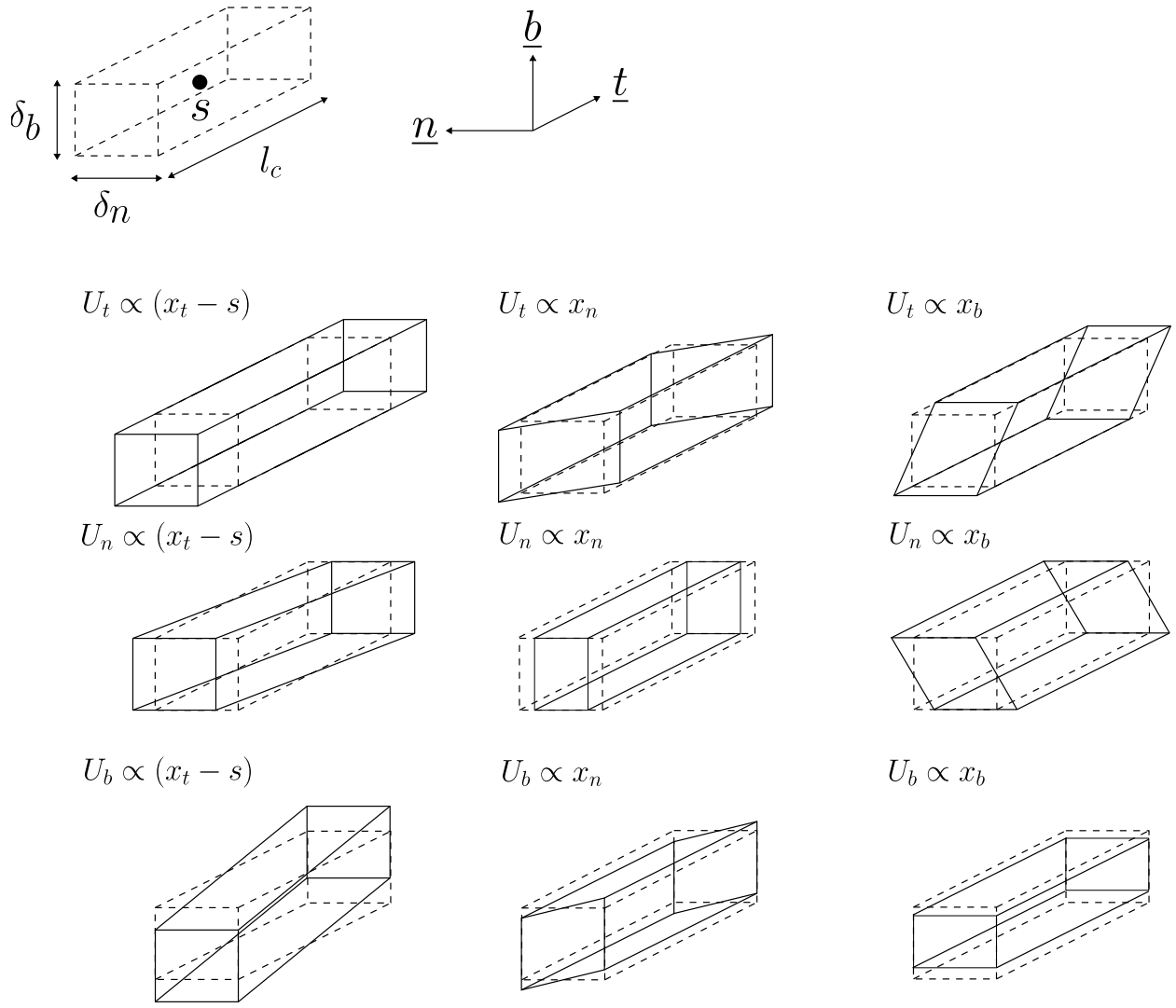

Figure C.13: 3D displacements for the first gradient components.

Which reads:

$$\begin{aligned} \boldsymbol{\varepsilon} \;&= \boldsymbol{\xi} + \left((x_t - s)\, \boldsymbol{L}_t + x_n\, \boldsymbol{L}_n + x_b\, \boldsymbol{L}_b \right) \vdots \boldsymbol{\chi} \\ &\quad + \left((x_t - s)\, x_n\, \boldsymbol{L}_{tn} + (x_t - s)\, x_b\, \boldsymbol{L}_{tb} + x_n\, x_b\, \boldsymbol{L}_{nb} \right) . \boldsymbol{\gamma} \end{aligned} \tag{C.4}$$

where following localization fifth order tensors have been introduced:

$$\begin{aligned} \boldsymbol{L}_t \;&= \boldsymbol{n} \otimes \boldsymbol{n} \otimes \boldsymbol{t} \otimes \boldsymbol{n} \otimes \boldsymbol{n} + \boldsymbol{b} \otimes \boldsymbol{b} \otimes \boldsymbol{t} \otimes \boldsymbol{b} \otimes \boldsymbol{b} \\ &\quad + \tfrac{1}{2} \left(\boldsymbol{t} \otimes \boldsymbol{n} + \boldsymbol{n} \otimes \boldsymbol{t} \right) \otimes \boldsymbol{t} \otimes \boldsymbol{n} \otimes \boldsymbol{t} \\ &\quad + \tfrac{1}{2} \left(\boldsymbol{t} \otimes \boldsymbol{b} + \boldsymbol{b} \otimes \boldsymbol{t} \right) \otimes \boldsymbol{t} \otimes \boldsymbol{b} \otimes \boldsymbol{t} \\ &\quad + \tfrac{1}{2} \left(\boldsymbol{n} \otimes \boldsymbol{b} + \boldsymbol{b} \otimes \boldsymbol{n} \right) \otimes \left(\boldsymbol{t} \otimes \boldsymbol{b} \otimes \boldsymbol{n} + \boldsymbol{t} \otimes \boldsymbol{n} \otimes \boldsymbol{b} \right) \end{aligned} \tag{C.5}$$

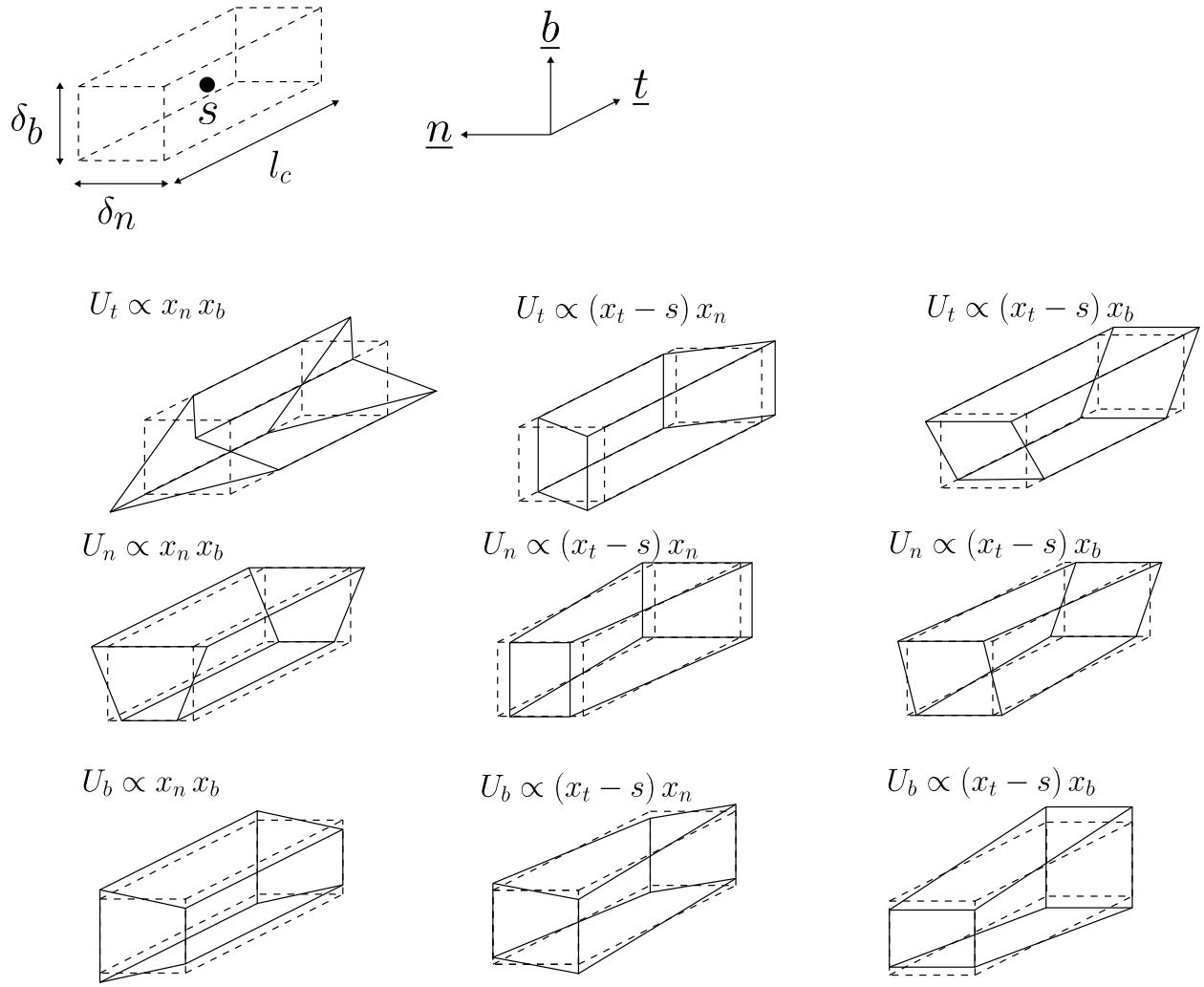

Figure C.14: 3D displacements for the second gradient components.

$$\begin{aligned}\boldsymbol{L}_n \;&= \boldsymbol{t}\otimes\boldsymbol{t}\otimes\boldsymbol{t}\otimes\boldsymbol{n}\otimes\boldsymbol{t} + \boldsymbol{b}\otimes\boldsymbol{b}\otimes\boldsymbol{b}\otimes\boldsymbol{n}\otimes\boldsymbol{b} \\ &\quad + \tfrac{1}{2}\left(\boldsymbol{t}\otimes\boldsymbol{n} + \boldsymbol{n}\otimes\boldsymbol{t}\right)\otimes\boldsymbol{t}\otimes\boldsymbol{n}\otimes\boldsymbol{n} \\ &\quad + \tfrac{1}{2}\left(\boldsymbol{t}\otimes\boldsymbol{b} + \boldsymbol{b}\otimes\boldsymbol{t}\right)\otimes\left(\boldsymbol{b}\otimes\boldsymbol{n}\otimes\boldsymbol{t} + \boldsymbol{t}\otimes\boldsymbol{n}\otimes\boldsymbol{b}\right) \\ &\quad + \tfrac{1}{2}\left(\boldsymbol{n}\otimes\boldsymbol{b} + \boldsymbol{b}\otimes\boldsymbol{n}\right)\otimes\boldsymbol{b}\otimes\boldsymbol{n}\otimes\boldsymbol{n}\end{aligned} \tag{C.6}$$

$$\begin{aligned}\boldsymbol{L}_b \;&= \boldsymbol{t}\otimes\boldsymbol{t}\otimes\boldsymbol{t}\otimes\boldsymbol{b}\otimes\boldsymbol{t} + \boldsymbol{n}\otimes\boldsymbol{n}\otimes\boldsymbol{b}\otimes\boldsymbol{n}\otimes\boldsymbol{n} \\ &\quad + \tfrac{1}{2}\left(\boldsymbol{t}\otimes\boldsymbol{n} + \boldsymbol{n}\otimes\boldsymbol{t}\right)\otimes\left(\boldsymbol{t}\otimes\boldsymbol{b}\otimes\boldsymbol{n} + \boldsymbol{b}\otimes\boldsymbol{n}\otimes\boldsymbol{t}\right) \\ &\quad + \tfrac{1}{2}\left(\boldsymbol{t}\otimes\boldsymbol{b} + \boldsymbol{b}\otimes\boldsymbol{t}\right)\otimes\boldsymbol{t}\otimes\boldsymbol{b}\otimes\boldsymbol{b} \\ &\quad + \tfrac{1}{2}\left(\boldsymbol{n}\otimes\boldsymbol{b} + \boldsymbol{b}\otimes\boldsymbol{n}\right)\otimes\boldsymbol{b}\otimes\boldsymbol{n}\otimes\boldsymbol{b}\end{aligned} \tag{C.7}$$

And where following localization third order tensors have been introduced:

$$\boldsymbol{L}_{tn} = \boldsymbol{b}\otimes\boldsymbol{b}\otimes\boldsymbol{b} + \frac{1}{2}\left(\boldsymbol{t}\otimes\boldsymbol{b} + \boldsymbol{b}\otimes\boldsymbol{t}\right)\otimes\boldsymbol{t} + \frac{1}{2}\left(\boldsymbol{n}\otimes\boldsymbol{b} + \boldsymbol{b}\otimes\boldsymbol{n}\right)\otimes\boldsymbol{n} \tag{C.8}$$

$$\boldsymbol{L}_{tb} = \boldsymbol{n}\otimes\boldsymbol{n}\otimes\boldsymbol{n} + \frac{1}{2}\left(\boldsymbol{t}\otimes\boldsymbol{n} + \boldsymbol{n}\otimes\boldsymbol{t}\right)\otimes\boldsymbol{t} + \frac{1}{2}\left(\boldsymbol{n}\otimes\boldsymbol{b} + \boldsymbol{b}\otimes\boldsymbol{n}\right)\otimes\boldsymbol{b} \tag{C.9}$$

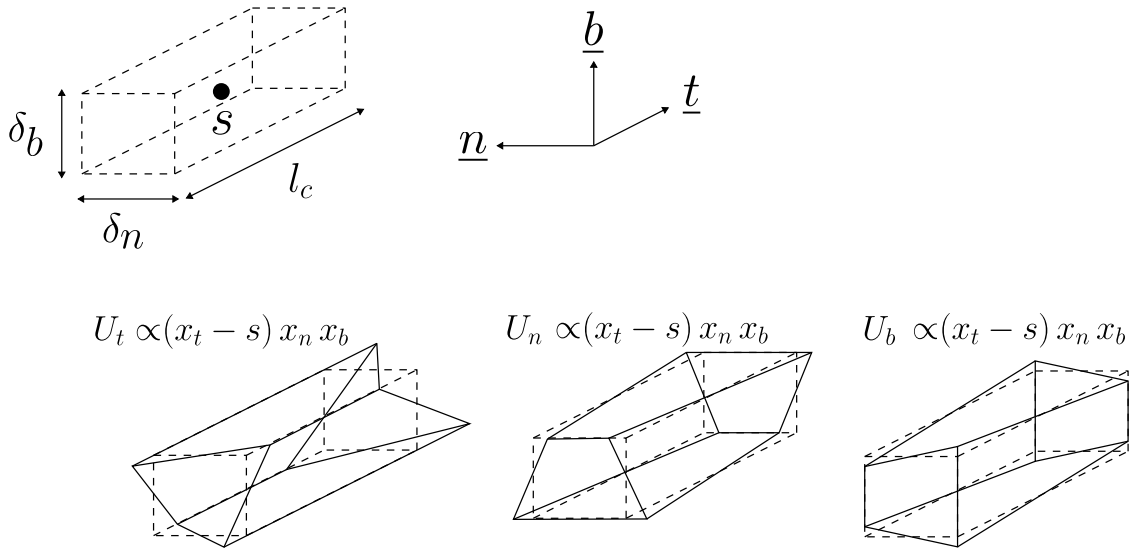

Figure C.15: 3D displacements for the third gradient components.

$$\boldsymbol{L}_{nb} = \boldsymbol{t}\otimes\boldsymbol{t}\otimes\boldsymbol{t} + \frac{1}{2}\left(\boldsymbol{t}\otimes\boldsymbol{n} + \boldsymbol{n}\otimes\boldsymbol{t}\right)\otimes\boldsymbol{n} + \frac{1}{2}\left(\boldsymbol{t}\otimes\boldsymbol{b} + \boldsymbol{b}\otimes\boldsymbol{t}\right)\otimes\boldsymbol{b} \tag{C.10}$$

Furthermore, one can notice that the average volume variation is related to the average trace operator, i.e., $(1/|\Omega_s|)\int_{\Omega_s}\mathrm{tr}\,(\boldsymbol{\varepsilon})\,\mathrm{d}\Omega = \mathrm{tr}(\boldsymbol{\xi})$. The Helmholtz free energy per unit length is defined in (60) and reads for $\Delta T = 0$ and $\Gamma = 0$:

$$\begin{aligned}\rho\,\psi(s) \;&= \frac{1}{2}\,\boldsymbol{\xi}(s) : \underbrace{\left(\boldsymbol{R}^{\xi} : \boldsymbol{\xi}(s) + \boldsymbol{R}^{\xi\chi} \vdots \boldsymbol{\chi}(s) + \boldsymbol{R}^{\xi\gamma}.\boldsymbol{\gamma}(s)\right)}_{\boldsymbol{\Sigma}(s)} \\ &+ \frac{1}{2}\,\boldsymbol{\chi}(s) \vdots \underbrace{\left(\boldsymbol{R}^{\chi} \vdots \boldsymbol{\chi}(s) + \boldsymbol{\xi}(s) : \boldsymbol{R}^{\xi\chi} + \boldsymbol{R}^{\chi\gamma}.\boldsymbol{\gamma}(s)\right)}_{\boldsymbol{M}(s)} \\ &+ \frac{1}{2}\,\boldsymbol{\gamma}(s).\underbrace{\left(\boldsymbol{R}^{\gamma}.\boldsymbol{\gamma}(s) + \boldsymbol{\xi}(s) : \boldsymbol{R}^{\xi\gamma} + \boldsymbol{\chi}(s) \vdots \boldsymbol{R}^{\chi\gamma}\right)}_{\boldsymbol{M}_{\times}(s)}\end{aligned} \tag{C.11}$$

The free energy per unit length denoted by $\rho^{3\mathrm{D}}\,\psi^{3\mathrm{D}}(s)$ (J.m^{-1}) of the 3D model is calculated as the average value along the tangential direction $\boldsymbol{t}$ of the total free energy in the RVE, hence:

$$\rho^{3\mathrm{D}}\,\psi^{3\mathrm{D}}(s) = \frac{1}{2\,l_c}\int_{-\frac{l_c}{2}}^{\frac{l_c}{2}}\int_{-\frac{\delta n}{2}}^{\frac{\delta n}{2}}\int_{-\frac{\delta b}{2}}^{\frac{\delta b}{2}} \boldsymbol{\varepsilon} : \underbrace{\boldsymbol{C} : \boldsymbol{\varepsilon}}_{\boldsymbol{\sigma}}\,\mathrm{d}x_t\,\mathrm{d}x_n\,\mathrm{d}x_b \tag{C.12}$$

where $\boldsymbol{C}$ is the Cauchy stiffness matrix.

Consider an isotropic material with bulk and shear moduli denoted by k_0 (MPa) and μ (MPa) respectively. Hence the Cauchy stress tensor $\boldsymbol{\sigma}$ reads:

$$\boldsymbol{\sigma} = k_0\,\frac{\mathrm{tr}(\boldsymbol{\varepsilon})}{3}\mathbf{1} + 2\mu\,\mathrm{dev}(\boldsymbol{\varepsilon}) \tag{C.13}$$

By decomposing the elastic 3D strain as follows $\boldsymbol{\varepsilon} = \frac{\mathrm{tr}(\boldsymbol{\varepsilon})}{3}\mathbf{1} + \mathrm{dev}(\boldsymbol{\varepsilon})$ we obtain:

$$\rho^{3\mathrm{D}}\psi^{3\mathrm{D}}(s) = \frac{1}{2\,l_c}\int_{-\frac{l_c}{2}}^{\frac{l_c}{2}}\int_{-\frac{\delta n}{2}}^{\frac{\delta n}{2}}\int_{-\frac{\delta b}{2}}^{\frac{\delta b}{2}}\left(k_0\,\frac{\mathrm{tr}(\boldsymbol{\varepsilon})^2}{3} + 2\mu\,\mathrm{dev}(\boldsymbol{\varepsilon}) : \mathrm{dev}(\boldsymbol{\varepsilon})\right)\mathrm{d}x_t\,\mathrm{d}x_n\,\mathrm{d}x_b \tag{C.14}$$

From (C.4) the following expression holds:

$$\begin{aligned}\rho^{3\mathrm{D}}\psi^{3\mathrm{D}}(s) \;&= \tfrac{1}{2}\left(\delta n\delta b\left(\tfrac{k_0}{3}\mathrm{tr}(\boldsymbol{\xi})^2 + 2\mu\,\mathrm{dev}(\boldsymbol{\xi}) : \mathrm{dev}(\boldsymbol{\xi})\right)\right.\\
&+\tfrac{l_c^2\delta n\delta b}{12}\left(\tfrac{k_0}{3}\mathrm{tr}\left(\boldsymbol{L}_t \vdots \boldsymbol{\chi}\right)^2 + 2\mu\,\mathrm{dev}\left(\boldsymbol{L}_t \vdots \boldsymbol{\chi}\right) : \mathrm{dev}\left(\boldsymbol{L}_t \vdots \boldsymbol{\chi}\right)\right)\\
&+\tfrac{\delta n^3\delta b}{12}\left(\tfrac{k_0}{3}\mathrm{tr}\left(\boldsymbol{L}_n \vdots \boldsymbol{\chi}\right)^2 + 2\mu\,\mathrm{dev}\left(\boldsymbol{L}_n \vdots \boldsymbol{\chi}\right) : \mathrm{dev}\left(\boldsymbol{L}_n \vdots \boldsymbol{\chi}\right)\right)\\
&\left.+\tfrac{\delta b^3\delta n}{12}\left(\tfrac{k_0}{3}\mathrm{tr}\left(\boldsymbol{L}_b \vdots \boldsymbol{\chi}\right)^2 + 2\mu\,\mathrm{dev}\left(\boldsymbol{L}_b \vdots \boldsymbol{\chi}\right) : \mathrm{dev}\left(\boldsymbol{L}_b \vdots \boldsymbol{\chi}\right)\right)\right)\end{aligned} \tag{C.15}$$

Which rewrites as follows:

$$\rho^{3\mathrm{D}}\psi^{3\mathrm{D}}(s) = \frac{\delta n\delta b}{2}\left(\boldsymbol{\xi} : \boldsymbol{C} : \boldsymbol{\xi} + \frac{l_c^2}{12}\,\boldsymbol{\chi} \vdots \boldsymbol{C}_t \vdots \boldsymbol{\chi} + \frac{\delta n^2}{12}\,\boldsymbol{\chi} \vdots \boldsymbol{C}_n \vdots \boldsymbol{\chi} + \frac{\delta b^2}{12}\,\boldsymbol{\chi} \vdots \boldsymbol{C}_b \vdots \boldsymbol{\chi}\right) \tag{C.16}$$

where the following sixth order tensors have been defined $\boldsymbol{C}_t = \left({}^{\dagger}\boldsymbol{L}_t : \boldsymbol{C} : \boldsymbol{L}_t\right), \boldsymbol{C}_n = \left({}^{\dagger}\boldsymbol{L}_n : \boldsymbol{C} : \boldsymbol{L}_n\right)$ and $\boldsymbol{C}_b = \left({}^{\dagger}\boldsymbol{L}_b : \boldsymbol{C} : \boldsymbol{L}_b\right)$, and where the pseudo transposition of fifth order tensors has been defined as follows:

$$\begin{aligned}&\forall(\boldsymbol{i},\boldsymbol{j},\boldsymbol{k},\boldsymbol{l},\boldsymbol{m}) \in \{\boldsymbol{t},\boldsymbol{n},\boldsymbol{b}\}^5,\\
&{}^{\dagger}(\boldsymbol{i}\otimes\boldsymbol{j}\otimes\boldsymbol{k}\otimes\boldsymbol{l}\otimes\boldsymbol{m}) = (\boldsymbol{k}\otimes\boldsymbol{l}\otimes\boldsymbol{m}\otimes\boldsymbol{i}\otimes\boldsymbol{j})\end{aligned} \tag{C.17}$$

By identifying (C.11) and (C.16) one obtains the homogenized stiffness tensors:

$$\begin{cases}\boldsymbol{R}^{\xi\chi} = 0 \quad \boldsymbol{R}^{\xi\gamma} = 0 \quad \boldsymbol{R}^{\chi\gamma} = 0 \quad \boldsymbol{R}^{\gamma} = 0\\
\boldsymbol{R}^{\xi} = \delta n\delta b\,\boldsymbol{C}\\
\boldsymbol{R}^{\chi} = \delta n\delta b\left[\left(\frac{l_c^2}{12}\right)\boldsymbol{C}_t + \left(\frac{\delta n^2}{12}\right)\boldsymbol{C}_n + \left(\frac{\delta b^2}{12}\right)\boldsymbol{C}_b\right]\end{cases} \tag{C.18}$$

A direct calculation gives the following component-wise expression:

$$\begin{aligned}\boldsymbol{C}_t = \;&\frac{k_0+4\mu}{3}(\boldsymbol{t}\otimes\boldsymbol{n}\otimes\boldsymbol{n}\otimes\boldsymbol{t}\otimes\boldsymbol{n}\otimes\boldsymbol{n} + \boldsymbol{t}\otimes\boldsymbol{b}\otimes\boldsymbol{b}\otimes\boldsymbol{t}\otimes\boldsymbol{b}\otimes\boldsymbol{b})\\
&+\frac{k_0-2\mu}{3}(\boldsymbol{t}\otimes\boldsymbol{n}\otimes\boldsymbol{n}\otimes\boldsymbol{t}\otimes\boldsymbol{b}\otimes\boldsymbol{b} + \boldsymbol{t}\otimes\boldsymbol{b}\otimes\boldsymbol{b}\otimes\boldsymbol{t}\otimes\boldsymbol{n}\otimes\boldsymbol{n})\\
&+\mu(\boldsymbol{t}\otimes\boldsymbol{n}\otimes\boldsymbol{t}\otimes\boldsymbol{t}\otimes\boldsymbol{n}\otimes\boldsymbol{t} + \boldsymbol{t}\otimes\boldsymbol{b}\otimes\boldsymbol{t}\otimes\boldsymbol{t}\otimes\boldsymbol{b}\otimes\boldsymbol{t})\\
&+\mu(\boldsymbol{t}\otimes\boldsymbol{n}\otimes\boldsymbol{b} + \boldsymbol{t}\otimes\boldsymbol{b}\otimes\boldsymbol{n})\otimes(\boldsymbol{t}\otimes\boldsymbol{n}\otimes\boldsymbol{b} + \boldsymbol{t}\otimes\boldsymbol{b}\otimes\boldsymbol{n}))\end{aligned} \tag{C.19}$$

$$\begin{aligned}\boldsymbol{C}_n = \;&\frac{k_0+4\mu}{3}(\boldsymbol{t}\otimes\boldsymbol{n}\otimes\boldsymbol{t}\otimes\boldsymbol{t}\otimes\boldsymbol{n}\otimes\boldsymbol{t} + \boldsymbol{b}\otimes\boldsymbol{n}\otimes\boldsymbol{b}\otimes\boldsymbol{b}\otimes\boldsymbol{n}\otimes\boldsymbol{b})\\
&+\frac{k_0-2\mu}{3}(\boldsymbol{t}\otimes\boldsymbol{n}\otimes\boldsymbol{t}\otimes\boldsymbol{b}\otimes\boldsymbol{n}\otimes\boldsymbol{b} + \boldsymbol{b}\otimes\boldsymbol{n}\otimes\boldsymbol{b}\otimes\boldsymbol{t}\otimes\boldsymbol{n}\otimes\boldsymbol{t})\\
&+\mu(\boldsymbol{t}\otimes\boldsymbol{n}\otimes\boldsymbol{n}\otimes\boldsymbol{t}\otimes\boldsymbol{n}\otimes\boldsymbol{n} + \boldsymbol{b}\otimes\boldsymbol{n}\otimes\boldsymbol{n}\otimes\boldsymbol{b}\otimes\boldsymbol{n}\otimes\boldsymbol{n})\\
&+\mu(\boldsymbol{b}\otimes\boldsymbol{n}\otimes\boldsymbol{t} + \boldsymbol{t}\otimes\boldsymbol{n}\otimes\boldsymbol{b})\otimes(\boldsymbol{b}\otimes\boldsymbol{n}\otimes\boldsymbol{t} + \boldsymbol{t}\otimes\boldsymbol{n}\otimes\boldsymbol{b}))\end{aligned} \tag{C.20}$$

$$
\begin{aligned}
\boldsymbol{C}_b = \quad & \frac{k_0+4\mu}{3}(\boldsymbol{t}\otimes\boldsymbol{b}\otimes\boldsymbol{t}\otimes\boldsymbol{t}\otimes\boldsymbol{b}\otimes\boldsymbol{t}+\boldsymbol{b}\otimes\boldsymbol{n}\otimes\boldsymbol{n}\otimes\boldsymbol{b}\otimes\boldsymbol{n}\otimes\boldsymbol{n}) \\
& +\frac{k_0-2\mu}{3}(\boldsymbol{t}\otimes\boldsymbol{b}\otimes\boldsymbol{t}\otimes\boldsymbol{b}\otimes\boldsymbol{n}\otimes\boldsymbol{n}+\boldsymbol{b}\otimes\boldsymbol{n}\otimes\boldsymbol{n}\otimes\boldsymbol{t}\otimes\boldsymbol{b}\otimes\boldsymbol{t}) \\
& +\mu(\boldsymbol{t}\otimes\boldsymbol{b}\otimes\boldsymbol{b}\otimes\boldsymbol{t}\otimes\boldsymbol{b}\otimes\boldsymbol{b}+\boldsymbol{b}\otimes\boldsymbol{n}\otimes\boldsymbol{b}\otimes\boldsymbol{b}\otimes\boldsymbol{n}\otimes\boldsymbol{b}) \\
& +\mu(\boldsymbol{b}\otimes\boldsymbol{n}\otimes\boldsymbol{t}+\boldsymbol{t}\otimes\boldsymbol{b}\otimes\boldsymbol{n})\otimes(\boldsymbol{b}\otimes\boldsymbol{n}\otimes\boldsymbol{t}+\boldsymbol{t}\otimes\boldsymbol{b}\otimes\boldsymbol{n}))
\end{aligned}
\tag{C.21}
$$

Therefore the 6×6 matrix R^{ξ} and the 9×9 matrix R^{χ} defined Appendix D reduce to:

$$
R^{\xi} = \begin{pmatrix}
p_1 & p_7 & p_8 & 0 & 0 & 0 \\
p_7 & p_2 & p_9 & 0 & 0 & 0 \\
p_8 & p_9 & p_3 & 0 & 0 & 0 \\
0 & 0 & 0 & p_4 & 0 & 0 \\
0 & 0 & 0 & 0 & p_5 & 0 \\
0 & 0 & 0 & 0 & 0 & p_6
\end{pmatrix}
\tag{C.22}
$$

$$
R^{\chi} = \begin{pmatrix}
p_{10} & 0 & 0 & 0 & 0 & 0 & 0 & 0 & p_{21} \\
0 & p_{11} & 0 & 0 & 0 & p_{19} & 0 & 0 & 0 \\
0 & 0 & p_{12} & 0 & p_{20} & 0 & p_{22} & 0 & 0 \\
0 & 0 & 0 & p_{13} & 0 & 0 & 0 & p_{23} & 0 \\
0 & 0 & p_{20} & 0 & p_{14} & 0 & p_{24} & 0 & 0 \\
0 & p_{19} & 0 & 0 & 0 & p_{15} & 0 & 0 & 0 \\
0 & 0 & p_{22} & 0 & p_{24} & 0 & p_{16} & 0 & 0 \\
0 & 0 & 0 & p_{23} & 0 & 0 & 0 & p_{17} & 0 \\
p_{21} & 0 & 0 & 0 & 0 & 0 & 0 & 0 & p_{18}
\end{pmatrix}
\tag{C.23}
$$

And the initial guess denoted by p^0 used in the minimization (63) reads:

$$
p_1^0 = p_2^0 = p_3^0 = A_1 \;\big|\; p_4^0 = p_5^0 = p_6^0 = 4\,A_2 \;\big|\; p_7^0 = p_8^0 = p_9^0 = A_3
\tag{C.24}
$$

$$
\begin{array}{lll}
p_{10}^0 = \dfrac{l_c^2}{12}A_2 + \dfrac{\delta n^2}{12}A_1 & p_{11}^0 = \dfrac{l_c^2}{12}A_1 + \dfrac{\delta n^2}{12}A_2 & p_{12}^0 = \left(\dfrac{l_c^2}{12} + \dfrac{\delta n^2}{12}\right)A_2 \\
p_{13}^0 = \dfrac{l_c^2}{12}A_2 + \dfrac{\delta b^2}{12}A_1 & p_{14}^0 = \left(\dfrac{l_c^2}{12} + \dfrac{\delta b^2}{12}\right)A_2 & p_{15}^0 = \dfrac{l_c^2}{12}A_1 + \dfrac{\delta b^2}{12}A_2 \\
p_{16}^0 = \left(\dfrac{\delta n^2}{12} + \dfrac{\delta b^2}{12}\right)A_2 & p_{17}^0 = \dfrac{\delta n^2}{12}A_2 + \dfrac{\delta b^2}{12}A_1 & p_{18}^0 = \dfrac{\delta n^2}{12}A_1 + \dfrac{\delta b^2}{12}A_2 \\
p_{19}^0 = \dfrac{l_c^2}{12}A_3 & p_{20}^0 = \dfrac{l_c^2}{12}A_2 & p_{21}^0 = \dfrac{\delta n^2}{12}A_3 \\
p_{22}^0 = \dfrac{\delta n^2}{12}A_2 & p_{23}^0 = \dfrac{\delta b^2}{12}A_3 & p_{24}^0 = \dfrac{\delta b^2}{12}A_2
\end{array}
\tag{C.25}
$$

where:

$$
A_1 = \delta n\,\delta b\left(\frac{k_0+4\mu}{3}\right) \;\Big|\; A_2 = \delta n\,\delta b\,\mu \;\Big|\; A_3 = \delta n\,\delta b\left(\frac{k_0-2\mu}{3}\right)
\tag{C.26}
$$

In addition, the optimized stiffness parameter $p^{\dagger}$ reads:

Table C.1: Optimized stiffness parameters $p^\dagger$ in (N).

$$p_1^\dagger = p_2^\dagger = p_3^\dagger = 40.38 \;\big|\; p_4^\dagger = p_5^\dagger = p_6^\dagger = 46.15 \;\big|\; p_7^\dagger = p_8^\dagger = p_9^\dagger = 17.31$$

Table C.2: Optimized stiffness parameters $p^\dagger$ in ($\times 10^{-4}$ N.mm^2).

$p_{10}^\dagger = 259$	$p_{11}^\dagger = 97.7$	$p_{12}^\dagger = 93.9$	$p_{13}^\dagger = 259$	$p_{14}^\dagger = 93.9$
$p_{15}^\dagger = 97.7$	$p_{16}^\dagger = 559$	$p_{17}^\dagger = 730$	$p_{18}^\dagger = 730$	$p_{19}^\dagger = 2.77$
$p_{20}^\dagger = 11.5$	$p_{21}^\dagger = 40.7$	$p_{22}^\dagger = 92.1$	$p_{23}^\dagger = 40.7$	$p_{24}^\dagger = 92.1$

It should be noted that isotropic material was considered to simplify the calculations, but in practice, a similar result with vanishing coupling stiffness tensors is obtained with orthotropic behavior. A similar situation is observed in plate theory, where orthotropic behavior leads to the decoupling between membrane and bending forces.

Appendix D. Finite elements discretization

In this section, a first order FEA is derived, where the initial curvature of each element is neglected. The general thermo-elastic behavior including eigenstrain derived in Section 4 is considered. The generalized displacements are determined by discretizing the virtual power principle (31), which rewrites as follows:

$$\begin{aligned}
&\int_{\mathcal{C}} \Big(\dot{\boldsymbol{\xi}}^*(s) : \boldsymbol{R}^\xi : \boldsymbol{\xi}(s) + \dot{\boldsymbol{\chi}}^*(s) \vdots \boldsymbol{R}^\chi \vdots \boldsymbol{\chi}(s) + \dot{\boldsymbol{\gamma}}^*(s).\boldsymbol{R}^\gamma.\boldsymbol{\gamma}(s) \\
&+\dot{\boldsymbol{\xi}}^*(s) : \boldsymbol{R}^{\xi\chi} \vdots \boldsymbol{\chi}(s) + \boldsymbol{\xi}(s) : \boldsymbol{R}^{\xi\chi} \vdots \dot{\boldsymbol{\chi}}^*(s) + \dot{\boldsymbol{\xi}}^*(s) : \boldsymbol{R}^{\xi\gamma}.\boldsymbol{\gamma}(s) + \boldsymbol{\xi}(s) : \boldsymbol{R}^{\xi\gamma}.\dot{\boldsymbol{\gamma}}^*(s) \\
&+\dot{\boldsymbol{\chi}}^*(s) \vdots \boldsymbol{R}^{\chi\gamma}.\boldsymbol{\gamma}(s) + \boldsymbol{\chi}(s) \vdots \boldsymbol{R}^{\chi\gamma}.\dot{\boldsymbol{\gamma}}^*(s) \Big)\, \mathrm{d}s \\
&= \int_{\mathcal{C}} \Big(\dot{\boldsymbol{\xi}}^*(s) : \boldsymbol{R}^\xi : \big(\boldsymbol{\alpha}^\xi\, \Delta T(s) + \boldsymbol{\beta}^\xi\, \Gamma(s) \big) + \dot{\boldsymbol{\chi}}^*(s) \vdots \boldsymbol{R}^\chi \vdots \left(\boldsymbol{\alpha}^\chi\, \Delta T(s) + \boldsymbol{\beta}^\chi\, \Gamma(s) \right) \\
&+\dot{\boldsymbol{\gamma}}^*(s).\boldsymbol{R}^\gamma.\left(\boldsymbol{\alpha}^\gamma\, \Delta T(s) + \boldsymbol{\beta}^\gamma\, \Gamma(s) \right) \Big)\, \mathrm{d}s \\
&+\int_{\mathcal{C}} \left(\boldsymbol{f}^{\mathrm{ext}}(s).\boldsymbol{v}^*(s) + \boldsymbol{m}_n^{\mathrm{ext}}(s).\frac{\delta^n \overrightarrow{\boldsymbol{v}}^*(s)}{\delta n} + \boldsymbol{m}_b^{\mathrm{ext}}(s).\frac{\delta^b \overrightarrow{\boldsymbol{v}}^*(s)}{\delta b} + \boldsymbol{m}_\times^{\mathrm{ext}}(s).\frac{\delta^\times \overrightarrow{\boldsymbol{v}}^*(s)}{\delta n\, \delta b} \right) \mathrm{d}s \\
&+\sum_{k=1}^{K} \boldsymbol{F}^{\mathrm{ext}}(s_k).\boldsymbol{v}^*(s_k) + \boldsymbol{M}_n^{\mathrm{ext}}(s_k).\frac{\delta^n \overrightarrow{\boldsymbol{v}}^*(s_k)}{\delta n} + \boldsymbol{M}_b^{\mathrm{ext}}(s_k).\frac{\delta^b \overrightarrow{\boldsymbol{v}}^*(s_k)}{\delta b}
\end{aligned} \tag{D.1}$$

where $\boldsymbol{\xi}, \boldsymbol{\chi}, \boldsymbol{\gamma}$ are the solution generalized strains being defined as in (24), (26) and (27) but using generalized displacements denoted by $\overrightarrow{\boldsymbol{u}} \in \mathcal{U}$, where $\mathcal{U}$ is the set of kinematically admissible generalized displacements defined as in (8) but replacing velocities by displacements. In addition, (D.1) should be verified for all $\overrightarrow{\boldsymbol{v}}^* \in \mathcal{V}^*$ defined in (9) from which $\dot{\boldsymbol{\xi}}^*, \dot{\boldsymbol{\chi}}^*$ and $\dot{\boldsymbol{\gamma}}^*$ are obtained by using (24), (26) and (27). In addition, the domain $\mathcal{C}$ is not necessarily composed of a unique line but can involve several disconnected parts, where K is the number of ending points denoted by s_k with $1 \leq k \leq K$.

Consider a mesh denoted by $\mathcal{C}_{\mathrm{mesh}}$ containing N_{e} elements denoted by $\mathcal{C}_j = (\boldsymbol{x}(s_{j0}), \boldsymbol{x}(s_{j1}))$ where $\boldsymbol{x}(s_{j0})$ and $\boldsymbol{x}(s_{j1})$ both belong to $\mathcal{C}$, with $s_{j0} < s_{j1}$ ($1 \leq j \leq N_{\mathrm{e}}$), and $\mathcal{C}_{\mathrm{mesh}} = \bigcup_{j=1}^{N_{\mathrm{e}}} \mathcal{C}_j$.

Consider a reference element defined by virtual abscissa $\eta \in (0,1)$, and linear shape functions denoted by $\eta \mapsto N_0(\eta)$ and $\eta \mapsto N_1(\eta)$ such as:

$$\eta \in (0,1) \mapsto N_0(\eta) = 1 - \eta \quad \text{and} \quad \eta \in (0,1) \mapsto N_1(\eta) = \eta \tag{D.2}$$

Thus, for each element $j \in \{1, \cdots, N_{\rm e}\}$, any curvilinear abscissa $s \in (s_{j0}, s_{j1})$ is written as follows:

$$s(\eta) = s_{j0}\, N_0(\eta) + s_{j1}\, N_1(\eta) \Rightarrow {\rm d}s = l_j\ {\rm d}\eta \tag{D.3}$$

where $l_j = s_{j1} - s_{j0}$ is the element length.

The solution displacement denoted by $\overrightarrow{\boldsymbol{u}}(s) = (\boldsymbol{u}_1(s), \boldsymbol{u}_2(s), \boldsymbol{u}_3(s), \boldsymbol{u}_4(s))$ is represented as a 12×1 matrix denoted by $U(s)$ where components are arranged as follows:

$$U(s) = \left(\begin{array}{cccccccccccc} u_{1t} & u_{2t} & u_{3t} & u_{4t} & u_{1n} & u_{2n} & u_{3n} & u_{4n} & u_{1b} & u_{2b} & u_{3b} & u_{4b} \end{array} \right)^{\top} \tag{D.4}$$

It should be noted that similar definitions hold for virtual motions. The displacement $U(s)$ is approximated as a function of nodal displacements in the global coordinate system denoted by U_{j0} and U_{j1} of size 12×1. Hence for each element $j \in \{1, \cdots, N_{\rm e}\}$:

$$U(s) \approx N(\eta)\, P_j\, U_j \tag{D.5}$$

where U_j and P_j are the following 24×1 and 24×24 matrices (where dots stand for 12×12 zero matrices):

$$U_j = \left(\begin{array}{c} U_{j0} \\ U_{j1} \end{array} \right) \quad \text{and} \quad P_j = \left(\begin{array}{cc} \mathring{P}_j & \cdot \\ \cdot & \mathring{P}_j \end{array} \right) \tag{D.6}$$

where $\mathring{P}_j$ is the 12×12 transition matrix between local and global coordinate systems of the j-th element. In addition $N(\eta)$ is the following 12×24 matrix:

$$N(\eta) = \left(\begin{array}{cc} N_0(\eta) I_{12} & N_1(\eta) I_{12} \end{array} \right) \tag{D.7}$$

where I_{12} is the 12×12 identity matrix. Furthermore:

$$U'(s) \approx N'(\eta)\, P_j\, U_j \tag{D.8}$$

where the derivation is considered with respect to the curvilinear abscissa s, hence $N'(\eta)$ reads as the following 12×24 matrix for each element $j \in \{1, \cdots, N_{\rm e}\}$:

$$N'(\eta) = \frac{1}{l_j} \left(\begin{array}{cc} -I_{12} & I_{12} \end{array} \right) \tag{D.9}$$

Consider $\mathring{P}$ the following 4×4 transition matrix and P the 24×24 block matrix (where dots stand for 4×4 zero matrices):

$$\mathring{P} = \begin{pmatrix} \frac{1}{4} & \frac{1}{4} & \frac{1}{4} & \frac{1}{4} \\ \frac{1}{2} & \frac{1}{2} & -\frac{1}{2} & -\frac{1}{2} \\ \frac{1}{2} & -\frac{1}{2} & \frac{1}{2} & -\frac{1}{2} \\ 1 & -1 & -1 & 1 \end{pmatrix} \tag{D.10}$$

$$P = \begin{pmatrix} \mathring{P} & \cdot & \cdot & \cdot & \cdot & \cdot \\ \cdot & \mathring{P} & \cdot & \cdot & \cdot & \cdot \\ \cdot & \cdot & \mathring{P} & \cdot & \cdot & \cdot \\ \cdot & \cdot & \cdot & \mathring{P} & \cdot & \cdot \\ \cdot & \cdot & \cdot & \cdot & \mathring{P} & \cdot \\ \cdot & \cdot & \cdot & \cdot & \cdot & \mathring{P} \end{pmatrix} \tag{D.11}$$

In addition, applying the operator (21) consider the 12×1 matrix:

$$\delta U(s) = \begin{pmatrix} u_t & \delta^n u_t & \delta^b u_t & \delta^\times u_t & u_n & \delta^n u_n & \delta^b u_n & \delta^\times u_n & u_b & \delta^n u_b & \delta^b u_b & \delta^\times u_b \end{pmatrix}^\top \tag{D.12}$$

Hence $\delta U(s)$ is written as follows:

$$\delta U(s) \approx N(\eta)\, P\, P_j\, U_j \tag{D.13}$$

The second order symmetric tensor $\boldsymbol{\xi}(s)$ is represented by a 6×1 matrix, which reads according to the definition (24):

$$\xi(s) = \begin{pmatrix} u'_t & \frac{\delta^n u_n}{\delta n} & \frac{\delta^b u_b}{\delta b} & \frac{1}{2}\left(u'_n + \frac{\delta^n u_t}{\delta n}\right) & \frac{1}{2}\left(u'_b + \frac{\delta^b u_t}{\delta b}\right) & \frac{1}{2}\left(\frac{\delta^n u_b}{\delta n} + \frac{\delta^b u_n}{\delta b}\right) \end{pmatrix}^\top \tag{D.14}$$

Therefore the generalized strain is approximated in the j-th element as follows:

$$\xi(s) \approx B_j(\eta)\, U_j \tag{D.15}$$

where the following 6×24 matrix has been introduced:

$$B_j(\eta) = \left(B_0 N(\eta) + B_1 N'(\eta)\right)\, P\, P_j \tag{D.16}$$

where B_0 and B_1 are 6×12 matrices determined by using the first gradient definition (24) and (25), which read (where dots stand for 0):

$$B_0 = \begin{pmatrix} \cdot & \cdot & \cdot & \cdot & \cdot & \cdot & \cdot & \cdot & \cdot & \cdot & \cdot & \cdot \\ \cdot & \cdot & \cdot & \cdot & \cdot & \frac{1}{\delta n} & \cdot & \cdot & \cdot & \cdot & \cdot & \cdot \\ \cdot & \cdot & \cdot & \cdot & \cdot & \cdot & \cdot & \cdot & \cdot & \cdot & \frac{1}{\delta b} & \cdot \\ \cdot & \frac{1}{2\delta n} & \cdot & \cdot & \cdot & \cdot & \cdot & \cdot & \cdot & \cdot & \cdot & \cdot \\ \cdot & \cdot & \frac{1}{2\delta b} & \cdot & \cdot & \cdot & \cdot & \cdot & \cdot & \cdot & \cdot & \cdot \\ \cdot & \cdot & \cdot & \cdot & \cdot & \cdot & \frac{1}{2\delta b} & \cdot & \cdot & \frac{1}{2\delta n} & \cdot & \cdot \end{pmatrix} \quad B_1 = \begin{pmatrix} 1 & \cdot & \cdot & \cdot & \cdot & \cdot & \cdot & \cdot & \cdot & \cdot & \cdot & \cdot \\ \cdot & \cdot & \cdot & \cdot & \cdot & \cdot & \cdot & \cdot & \cdot & \cdot & \cdot & \cdot \\ \cdot & \cdot & \cdot & \cdot & \cdot & \cdot & \cdot & \cdot & \cdot & \cdot & \cdot & \cdot \\ \cdot & \cdot & \cdot & \cdot & \frac{1}{2} & \cdot & \cdot & \cdot & \cdot & \cdot & \cdot & \cdot \\ \cdot & \cdot & \cdot & \cdot & \cdot & \cdot & \cdot & \cdot & \frac{1}{2} & \cdot & \cdot & \cdot \\ \cdot & \cdot & \cdot & \cdot & \cdot & \cdot & \cdot & \cdot & \cdot & \cdot & \cdot & \cdot \end{pmatrix} \tag{D.17}$$

In addition, the first generalized strain tensor $\boldsymbol{\chi}(s) \in \mathcal{T}^3_\chi$ is represented by a 9×1 matrix, which reads according to the definition (26):

$$\chi(s) = \begin{pmatrix} \frac{\delta^n u'_t}{\delta n} & \frac{\delta^n u'_n}{\delta n} & \frac{\delta^n u'_b}{\delta n} & \frac{\delta^b u'_t}{\delta b} & \frac{\delta^b u'_n}{\delta b} & \frac{\delta^b u'_b}{\delta b} & \frac{\delta^\times u_t}{\delta n \delta b} & \frac{\delta^\times u_n}{\delta n \delta b} & \frac{\delta^\times u_b}{\delta n \delta b} \end{pmatrix}^\top \tag{D.18}$$

Therefore the second generalized strain is approximated in the j-th element as follows:

$$\chi(s) \approx C_j(\eta)\, U_j \tag{D.19}$$

where the following 9×24 matrix has been introduced:

$$C_j(\eta) = \left(C_0 N(\eta) + C_1 N'(\eta)\right)\, P\, P_j \tag{D.20}$$

where C_0 and C_1 are 9×12 matrices determined by using the second order gradient definition (26), which read (where dots stand for 0):

$$C_0 = \begin{pmatrix} \cdot & \cdot & \cdot & \cdot & \cdot & \cdot & \cdot & \cdot & \cdot & \cdot & \cdot & \cdot \\ \cdot & \cdot & \cdot & \cdot & \cdot & \cdot & \cdot & \cdot & \cdot & \cdot & \cdot & \cdot \\ \cdot & \cdot & \cdot & \cdot & \cdot & \cdot & \cdot & \cdot & \cdot & \cdot & \cdot & \cdot \\ \cdot & \cdot & \cdot & \cdot & \cdot & \cdot & \cdot & \cdot & \cdot & \cdot & \cdot & \cdot \\ \cdot & \cdot & \cdot & \cdot & \cdot & \cdot & \cdot & \cdot & \cdot & \cdot & \cdot & \cdot \\ \cdot & \cdot & \cdot & \cdot & \cdot & \cdot & \cdot & \cdot & \cdot & \cdot & \cdot & \cdot \\ \cdot & \cdot & \cdot & \frac{1}{\delta n\, \delta b} & \cdot & \cdot & \cdot & \cdot & \cdot & \cdot & \cdot & \cdot \\ \cdot & \cdot & \cdot & \cdot & \cdot & \cdot & \cdot & \frac{1}{\delta n\, \delta b} & \cdot & \cdot & \cdot & \cdot \\ \cdot & \cdot & \cdot & \cdot & \cdot & \cdot & \cdot & \cdot & \cdot & \cdot & \cdot & \frac{1}{\delta n\, \delta b} \end{pmatrix} \quad C_1 = \begin{pmatrix} \cdot & \frac{1}{\delta n} & \cdot & \cdot & \cdot & \cdot & \cdot & \cdot & \cdot & \cdot & \cdot & \cdot \\ \cdot & \cdot & \cdot & \cdot & \cdot & \frac{1}{\delta n} & \cdot & \cdot & \cdot & \cdot & \cdot & \cdot \\ \cdot & \cdot & \cdot & \cdot & \cdot & \cdot & \cdot & \cdot & \cdot & \frac{1}{\delta n} & \cdot & \cdot \\ \cdot & \cdot & \frac{1}{\delta b} & \cdot & \cdot & \cdot & \cdot & \cdot & \cdot & \cdot & \cdot & \cdot \\ \cdot & \cdot & \cdot & \cdot & \cdot & \cdot & \frac{1}{\delta b} & \cdot & \cdot & \cdot & \cdot & \cdot \\ \cdot & \cdot & \cdot & \cdot & \cdot & \cdot & \cdot & \cdot & \cdot & \cdot & \frac{1}{\delta b} & \cdot \\ \cdot & \cdot & \cdot & \cdot & \cdot & \cdot & \cdot & \cdot & \cdot & \cdot & \cdot & \cdot \\ \cdot & \cdot & \cdot & \cdot & \cdot & \cdot & \cdot & \cdot & \cdot & \cdot & \cdot & \cdot \\ \cdot & \cdot & \cdot & \cdot & \cdot & \cdot & \cdot & \cdot & \cdot & \cdot & \cdot & \cdot \end{pmatrix} \tag{D.21}$$

In addition the, the strain $\boldsymbol{\gamma}(s) \in \mathbb{R}^3$ is represented by a 3×1 matrix, which reads according to the definition (27):

$$\gamma(s) = \begin{pmatrix} \frac{\delta^\times u'_t}{\delta n \delta b} & \frac{\delta^\times u'_n}{\delta n \delta b} & \frac{\delta^\times u'_b}{\delta n \delta b} \end{pmatrix}^\top \tag{D.22}$$

Therefore the third generalized strain is approximated in the j-th element as follows:

$$\gamma(s) \approx D_j(\eta)\, U_j \tag{D.23}$$

where the following 3×24 matrix has been introduced:

$$D_j(\eta) = D_1\, N'(\eta)\, P\, P_j \tag{D.24}$$

where D_1 is the following 3×12 matrices:

$$D_1 = \begin{pmatrix} \cdot & \cdot & \cdot & \frac{1}{\delta n \delta b} & \cdot & \cdot & \cdot & \cdot & \cdot & \cdot & \cdot & \cdot \\ \cdot & \cdot & \cdot & \cdot & \cdot & \cdot & \cdot & \frac{1}{\delta n \delta b} & \cdot & \cdot & \cdot & \cdot \\ \cdot & \cdot & \cdot & \cdot & \cdot & \cdot & \cdot & \cdot & \cdot & \cdot & \cdot & \frac{1}{\delta n \delta b} \end{pmatrix} \tag{D.25}$$

Thus, the left-hand side of (D.1) is approximated as follows:

$$\int_{\mathcal{C}} \left(\dot{\boldsymbol{\xi}}^*(s) : \boldsymbol{R}^\xi : \boldsymbol{\xi}(s) + \dot{\boldsymbol{\chi}}^*(s) \vdots \boldsymbol{R}^\chi \vdots \boldsymbol{\chi}(s) + \dot{\boldsymbol{\gamma}}^*(s) . \boldsymbol{R}^\gamma . \boldsymbol{\gamma}(s) + \cdots \right) \mathrm{d}s \approx \sum_{j=1}^{J} V_j^{*\top}\, K_j\, U_j \tag{D.26}$$

where V_j^* is the virtual nodal motion defined similarly as U_j, in addition K_j is a 24×24 matrix called element stiffness, which reads:

$$\begin{aligned} K_j = \; & \int_0^1 l_j \Big(B_j(\eta)^\top R^\xi B_j(\eta) + C_j(\eta)^\top R^\chi C_j(\eta) + D_j(\eta)^\top R^\gamma D_j(\eta) \\ & + B_j(\eta)^\top R^{\xi\chi} C_j(\eta) + C_j(\eta)^\top R^{\xi\chi\top} B_j(\eta) \\ & + B_j(\eta)^\top R^{\xi\gamma} D_j(\eta) + D_j(\eta)^\top R^{\xi\gamma\top} B_j(\eta) \\ & + C_j(\eta)^\top R^{\chi\gamma} D_j(\eta) + D_j(\eta)^\top R^{\chi\gamma\top} C_j(\eta) \Big)\, \mathrm{d}\eta \end{aligned} \tag{D.27}$$

where R^{ξ}, R^{χ} and R^{γ} are respectively 6×6, 9×9 and 3×3 positive-definite matrices. Moreover $R^{\xi\chi}$, $R^{\xi\gamma}$ and $R^{\chi\gamma}$ are respectively 6×9, 6×3 and 9×3 matrices. The integral (D.27) is computed using classical Gauss-Legendre quadrature of order $N_G = 2$, where Gauss points are defined as $\eta_1^G = \left(1 - 1/\sqrt{3}\right)/2$ and $\eta_2^G = \left(1 + 1/\sqrt{3}\right)/2$ and weights $w_1^G = w_2^G = 0.5$, hence:

$$\begin{aligned} K_j = \sum_{i=1}^{N_G} w_i^G\, l_j \Big(& B_j(\eta_i^G)^\top R^{\xi} B_j(\eta_i^G) + C_j(\eta_i^G)^\top R^{\chi} C_j(\eta_i^G) + D_j(\eta_i^G)^\top R^{\gamma} D_j(\eta_i^G) \\ & + B_j(\eta_i^G)^\top R^{\xi\chi} C_j(\eta_i^G) + C_j(\eta_i^G)^\top R^{\xi\chi\top} B_j(\eta_i^G) \\ & + B_j(\eta_i^G)^\top R^{\xi\gamma} D_j(\eta_i^G) + D_j(\eta_i^G)^\top R^{\xi\gamma\top} B_j(\eta_i^G) \\ & + C_j(\eta_i^G)^\top R^{\chi\gamma} D_j(\eta_i^G) + D_j(\eta_i^G)^\top R^{\chi\gamma\top} C_j(\eta_i^G) \Big) \end{aligned} \tag{D.28}$$

The temperature variation $\Delta T(s)$ and the state variable $\Gamma(s)$ are approximated by using nodal values ΔT_{j0} and ΔT_{j1} (resp. Γ_{j0} and Γ_{j1}) as follows:

$$\Delta T(s) \approx \widetilde{N}(\eta)\, \Delta T_j \quad \text{and} \quad \Gamma(s) \approx \widetilde{N}(\eta)\, \Gamma_j \tag{D.29}$$

where ΔT_j and Γ_j are the following 2×1 matrices $\Delta T_j = \begin{pmatrix} \Delta T_{j0} & \Delta T_{j1} \end{pmatrix}^\top$ and $\Gamma_j = \begin{pmatrix} \Gamma_{j0} & \Gamma_{j1} \end{pmatrix}^\top$ and $\widetilde{N}(\eta)$ is the following 1×2 matrix $\widetilde{N}(\eta) = \begin{pmatrix} N_0(\eta) & N_1(\eta) \end{pmatrix}$. Thus, the first integral of the right-hand side of (D.1) reads:

$$\begin{aligned} \int_{\mathcal{C}} \left(\dot{\boldsymbol{\xi}}^*(s) : \boldsymbol{R}^{\xi} : \boldsymbol{\alpha}^{\xi} + \dot{\boldsymbol{\chi}}^*(s) \vdots \boldsymbol{R}^{\chi} \vdots \boldsymbol{\alpha}^{\chi} + \dot{\boldsymbol{\gamma}}^*(s) : \boldsymbol{R}^{\gamma} : \boldsymbol{\alpha}^{\gamma} \right) \Delta T(s)\, \mathrm{d}s &\approx \sum_{j=1}^{J} V_j^{*\top}\, f_j^{\mathrm{th}}\, \Delta T_j \\ \int_{\mathcal{C}} \left(\dot{\boldsymbol{\xi}}^*(s) : \boldsymbol{R}^{\xi} : \boldsymbol{\beta}^{\xi} + \dot{\boldsymbol{\chi}}^*(s) \vdots \boldsymbol{R}^{\chi} \vdots \boldsymbol{\beta}^{\chi} + \dot{\boldsymbol{\gamma}}^*(s) : \boldsymbol{R}^{\gamma} : \boldsymbol{\beta}^{\gamma} \right) \Gamma(s)\, \mathrm{d}s &\approx \sum_{j=1}^{J} V_j^{*\top}\, f_j^{\mathrm{eig}}\, \Gamma_j \end{aligned} \tag{D.30}$$

where f_j^{th} and f_j^{eig} are the following 24×2 matrices:

$$\begin{aligned} f_j^{\mathrm{th}} &= \int_0^1 l_j \left(B_j(\eta)^\top R^{\xi}\, \alpha^{\xi} + C_j(\eta)^\top R^{\chi}\, \alpha^{\chi} + D_j(\eta)^\top R^{\gamma}\, \alpha^{\gamma} \right) \widetilde{N}(\eta)\, \mathrm{d}\eta \\ &\approx \sum_{i=1}^{N_G} w_i^G\, l_j \left(B_j(\eta_i^G)^\top R^{\xi}\, \alpha^{\xi} + C_j(\eta_i^G)^\top R^{\chi}\, \alpha^{\chi} + D_j(\eta_i^G)^\top R^{\gamma}\, \alpha^{\gamma} \right) \widetilde{N}(\eta_i^G) \\ f_j^{\mathrm{eig}} &= \int_0^1 l_j \left(B_j(\eta)^\top R^{\xi}\, \beta^{\xi} + C_j(\eta)^\top R^{\chi}\, \beta^{\chi} + D_j(\eta)^\top R^{\gamma}\, \beta^{\gamma} \right) \widetilde{N}(\eta)\, \mathrm{d}\eta \\ &\approx \sum_{i=1}^{N_G} w_i^G\, l_j \left(B_j(\eta_i^G)^\top R^{\xi}\, \beta^{\xi} + C_j(\eta_i^G)^\top R^{\chi}\, \beta^{\chi} + D_j(\eta_i^G)^\top R^{\gamma}\, \beta^{\gamma} \right) \widetilde{N}(\eta_i^G) \end{aligned} \tag{D.31}$$

where α^{ξ} and β^{ξ} are 6×1 matrices, α^{χ} and β^{χ} are a 9×1 matrices, and α^{γ} and β^{γ} are 3×1

matrices such as:

$$\left\{\begin{array}{l}
\alpha^{\xi} = \left(\begin{array}{cccccc} \alpha^{\xi}_{tt} & \alpha^{\xi}_{nn} & \alpha^{\xi}_{bb} & \alpha^{\xi}_{tn} & \alpha^{\xi}_{tb} & \alpha^{\xi}_{nb} \end{array}\right)^{\top} \\
\alpha^{\chi} = \left(\begin{array}{cccccccccc} \alpha^{\chi}_{tnt} & \alpha^{\chi}_{nnt} & \alpha^{\chi}_{bnt} & \alpha^{\chi}_{tbt} & \alpha^{\chi}_{nbt} & \alpha^{\chi}_{bbt} & \alpha^{\chi}_{tnb} & \alpha^{\chi}_{nnb} & \alpha^{\chi}_{bnb} \end{array}\right)^{\top} \\
\alpha^{\gamma} = \left(\begin{array}{ccc} \alpha^{\gamma}_{t} & \alpha^{\gamma}_{n} & \alpha^{\gamma}_{b} \end{array}\right)^{\top} \\
\beta^{\xi} = \left(\begin{array}{cccccc} \beta^{\xi}_{tt} & \beta^{\xi}_{nn} & \beta^{\xi}_{bb} & \beta^{\xi}_{tn} & \beta^{\xi}_{tb} & \beta^{\xi}_{nb} \end{array}\right)^{\top} \\
\beta^{\chi} = \left(\begin{array}{cccccccccc} \beta^{\chi}_{tnt} & \beta^{\chi}_{nnt} & \beta^{\chi}_{bnt} & \beta^{\chi}_{tbt} & \beta^{\chi}_{nbt} & \beta^{\chi}_{bbt} & \beta^{\chi}_{tnb} & \beta^{\chi}_{nnb} & \beta^{\chi}_{bnb} \end{array}\right)^{\top} \\
\beta^{\gamma} = \left(\begin{array}{ccc} \beta^{\gamma}_{t} & \beta^{\gamma}_{n} & \beta^{\gamma}_{b} \end{array}\right)^{\top}
\end{array}\right. \tag{D.32}$$

Similarly, the second integral of the right-hand side of (D.1) reads:

$$\int_{\mathcal{C}} \left(\boldsymbol{f}^{\text{ext}}(s).\boldsymbol{v}^*(s) + \boldsymbol{m}^{\text{ext}}_n(s).\frac{\delta^n \overrightarrow{\boldsymbol{v}}^*(s)}{\delta n} + \boldsymbol{m}^{\text{ext}}_b(s).\frac{\delta^b \overrightarrow{\boldsymbol{v}}^*(s)}{\delta b} + \boldsymbol{m}^{\text{ext}}_{\times}(s).\frac{\delta^{\times} \overrightarrow{\boldsymbol{v}}^*(s)}{\delta n\, \delta b} \right) \mathrm{d}s \approx \sum_{j=1}^{J} {V_j^*}^{\top} f_j^{\text{ext}} \tag{D.33}$$

where f_j^{ext} is the following 24×1 matrix:

$$f_j^{\text{ext}} = \int_0^1 l_j P^{\top} N(\eta)^{\top} f^{\text{ext}}(\eta)\, \mathrm{d}\eta \approx \sum_{i=1}^{N_G} w_i^G\, l_j\, P^{\top} N(\eta_i^G)^{\top} f^{\text{ext}}(\eta_i^G) \tag{D.34}$$

where $f^{\text{ext}}(s)$ is the following 12×1 matrix:

$$f^{\text{ext}}(s) = \left(\begin{array}{cccccccccccc} f^{\text{ext}}_t & \frac{m^{\text{ext}}_{n,t}}{\delta n} & \frac{m^{\text{ext}}_{b,t}}{\delta b} & \frac{m^{\text{ext}}_{\times,t}}{\delta n\, \delta b} & f^{\text{ext}}_n & \frac{m^{\text{ext}}_{n,n}}{\delta n} & \frac{m^{\text{ext}}_{b,n}}{\delta b} & \frac{m^{\text{ext}}_{\times,n}}{\delta n\, \delta b} & f^{\text{ext}}_b & \frac{m^{\text{ext}}_{n,b}}{\delta n} & \frac{m^{\text{ext}}_{b,b}}{\delta b} & \frac{m^{\text{ext}}_{\times,b}}{\delta n\, \delta b} \end{array}\right)^{\top} \tag{D.35}$$

Considering that the last term in the weak form (D.1) applies to the ending points s_k (with $1 \leq k \leq K$) of the lines included in the domain, the corresponding virtual abscissa is $\eta = 0$ (resp. $\eta = 1$) for $s_k = s_{j_k 0}$ (resp. $s_k = s_{j_k 1}$) where j_k is the unique element containing the ending point s_k. Hence:

$$\sum_{k=1}^{K} \boldsymbol{F}^{\text{ext}}(s_k).\boldsymbol{v}^*(s_k) + \boldsymbol{M}^{\text{ext}}_n(s_k).\frac{\delta^n \overrightarrow{\boldsymbol{v}}^*(s_k)}{\delta n} + \boldsymbol{M}^{\text{ext}}_b(s_k).\frac{\delta^b \overrightarrow{\boldsymbol{v}}^*(s_k)}{\delta b} \approx \sum_{j=1}^{J} {V_j^*}^{\top} F_j^{\text{ext}} \tag{D.36}$$

where F_j^{ext} is the following 24×1 matrix:

$$F_j^{\text{ext}} = \left\{\begin{array}{ll} P^{\top} N(0)^{\top} F^{\text{ext}}(s_{j0}) & \text{if } \exists k \in \{1, \cdots, K\},\ s_k = s_{j0} \\ P^{\top} N(1)^{\top} F^{\text{ext}}(s_{j1}) & \text{if } \exists k \in \{1, \cdots, K\},\ s_k = s_{j1} \\ 0 & \text{else} \end{array}\right. \tag{D.37}$$

where $F^{\text{ext}}(s)$ is the following 12×1 matrix:

$$F^{\text{ext}}(s) = \left(\begin{array}{cccccccccccc} F^{\text{ext}}_t & \frac{M^{\text{ext}}_{n,t}}{\delta n} & \frac{M^{\text{ext}}_{b,t}}{\delta b} & \frac{M^{\text{ext}}_{\times,t}}{\delta n \delta b} & F^{\text{ext}}_n & \frac{M^{\text{ext}}_{n,n}}{\delta n} & \frac{M^{\text{ext}}_{b,n}}{\delta b} & \frac{M^{\text{ext}}_{\times,n}}{\delta n \delta b} & F^{\text{ext}}_b & \frac{M^{\text{ext}}_{n,b}}{\delta n} & \frac{M^{\text{ext}}_{b,b}}{\delta b} & \frac{M^{\text{ext}}_{\times,b}}{\delta n \delta b} \end{array}\right)^{\top} \tag{D.38}$$

The weak formulation (D.1) therefore reduces to:

$$\forall \overrightarrow{\boldsymbol{v}}^* \in \mathcal{V}^*,\ \sum_{j=1}^{J} {V_j^*}^{\top} K_j\, U_j = \sum_{j=1}^{J} {V_j^*}^{\top} \left(f_j^{\text{th}}\, \Delta T_j + f_j^{\text{eig}}\, \Gamma_j + f_j^{\text{ext}} + F_j^{\text{ext}} \right) \tag{D.39}$$

After standard assembly procedure one obtains (where brackets are used to denote assembled entities over all N_e elements of the mesh):

$$\forall\, [V]^* \in \mathbb{R}^{12N},\ [V]^{*\,\top}\, \widetilde{[K]}\ [U] = [V]^{*\,\top}\ \left[F^\mathrm{tot}\right] \tag{D.40}$$

Where:

$$\left[F^\mathrm{tot}\right] = \left[f^\mathrm{th}\right]^\top\ [\Delta T] + \left[f^\mathrm{eig}\right]^\top\ [\Gamma] + \left[f^\mathrm{ext}\right] + \left[F^\mathrm{ext}\right] \tag{D.41}$$

Since there are 12 DoF for each node, $[V]^*$ and $[U]$ are the assembled $12N \times 1$ virtual motion and solution displacement matrices in the global coordinate system, where N is the number of nodes in the mesh, $\widetilde{[K]}$ is the assembled $12N \times 12N$ stiffness matrix, $[\Delta T]$, $[\Gamma]$ are the assembled $12N \times 1$ temperature variation and additional state variable respectively, and $\left[f^\mathrm{th}\right]$, $[f^\mathrm{eig}]$, $[f^\mathrm{ext}]$ and $[F^\mathrm{ext}]$ are the assembled $12N \times 1$ force matrices.

In addition, let there be N_kin kinematic relations (e.g., with the build platform or between different beads), therefore there are only $N_\mathrm{dof} = 12N - N_\mathrm{kin}$ DoF in total. Consider $[U]_\mathrm{dof}$ of size $N_\mathrm{dof} \times 1$ the displacement components corresponding to these remaining DoF, and $[U]_\mathrm{kin}$ corresponding to the components fixed by the kinematic relations (and similarly for $[V]^*$) written in the form:

$$[U]_\mathrm{kin} = [C]_\mathrm{kin}\ [U]_\mathrm{dof} + [U]_0 \tag{D.42}$$

where $[C]_\mathrm{kin}$ is a known $N_\mathrm{kin} \times N_\mathrm{dof}$ matrix capturing the relationships between displacement components, and $[U_0]$ is a known $N_\mathrm{kin} \times 1$ matrix of imposed displacements. Thus, consider $\mathcal{V}^*_\mathrm{dof} \subset \mathbb{R}^{12N}$ the set of nodal virtual motions defined according to (9), which reads:

$$\mathcal{V}^*_\mathrm{dof} = \left\{[V]^* \in \mathbb{R}^{12N},\ [V]^*_\mathrm{kin} = 0\right\} \tag{D.43}$$

Thus, one cannot cancel $[V]^{*\,\top}$ from both sides in (D.40) as there are N_kin zero components in $[V]^*$. The system needs to be reduced, and in practice $12N \times N_\mathrm{kin}$ and $12N \times N_\mathrm{dof}$ matrices respectively denoted by $[L]_\mathrm{kin}$ and $[L]_\mathrm{dof}$ are introduced such as:

$$[U] = \begin{pmatrix} [L]_\mathrm{dof} & [L]_\mathrm{kin} \end{pmatrix} \begin{pmatrix} [U]_\mathrm{dof} \\ [U]_\mathrm{kin} \end{pmatrix} \tag{D.44}$$

Thus, using $[V]^*_\mathrm{kin} = 0$ the system (D.40) reduces to:

$$\forall\, [V]^*_\mathrm{dof} \in \mathbb{R}^{N_\mathrm{dof}},\ [V]^{*\,\top}_\mathrm{dof}\ [K]\ [U]_\mathrm{dof} = [V]^{*\,\top}_\mathrm{dof}\ [f]_\mathrm{dof} \tag{D.45}$$

where the $N_\mathrm{dof} \times N_\mathrm{dof}$ reduced global stiffness matrix has been introduced:

$$[K] = [L]^\top_\mathrm{dof}\, \widetilde{[K]}\ \left([L]_\mathrm{dof} + [L]_\mathrm{kin}\ [C]_\mathrm{kin}\right) \tag{D.46}$$

And where the modified $N_\mathrm{dof} \times 1$ force matrix accounting for kinematic relations and boundary conditions has been introduced:

$$[f]_\mathrm{dof} = [L]_\mathrm{dof}^{\top}\ \left(\left(\left[f^\mathrm{eig}\right] + \left[f^\mathrm{ext}\right]\right) - \widetilde{[K]}\ [L]_\mathrm{kin}\ [U]_0\right) \tag{D.47}$$

Eventually (D.45) reduces to:

$$[K]\ [U]_{\text{dof}} = [f]_{\text{dof}} \tag{D.48}$$

The linear system (D.48) is then solved to obtain nodal displacements $[U]_{\text{dof}}$, which enables to compute the remaining displacements $[U]_{\text{kin}}$ through the kinematic relations (D.42). In addition, stresses are computed at the Gauss points η_i^G in each element. This FEA has been implemented in Python [29].

Appendix E. Gradient of the objective function

One can rewrite (63) as follows:

$$\begin{cases} p^\dagger = & \underset{p\in\mathbb{R}^{24}}{\text{argmin}}\ J(p) + \epsilon\,\|p-p^0\|^2 \\ \text{s.t.} & [K]\,(p)\ [U]_{\text{dof}} - [f]_{\text{dof}}\,(p) = 0 \end{cases} \tag{E.1}$$

One can rewrite (64) as follows:

$$J(p) = \frac{1}{2}\sum_{j=1}^{N_{\text{e}}} l_j\ \left(\frac{1}{2}U_j^\top\ K_j^0(p)\,U_j - U_j^\top\ f_j^0(p) - \rho^{\text{3D}}\psi_j^{\text{3D}}\right)^2 \tag{E.2}$$

where N_{e} is the number of elements along the tangential direction, l_j is the j-th element length, U_j is the nodal displacement vector in the j-th element (defined by (D.26), which depends on p since it is a solution of (D.48)), and K_j^0 is the element stiffness matrix computed at the center of the j-th element, which reads:

$$K_j^0(p) = B_j^{0\top}\,R^\xi(p)\,B_j^0 + C_j^{0\top}\,R^\chi(p)\,C_j^0 \tag{E.3}$$

where B_j^0 and C_j^0 are defined in (D.16) and (D.20) and computed at the center of the j-th element. In addition f_j^0 is a force vector computed at the center of the j-th element as follows:

$$f_j^0(p) = B_j^{0\top}\,R^\xi(p)\,(\alpha^\xi\,\widetilde{N}^0\,\Delta T_j) \tag{E.4}$$

where $\widetilde{N}^0$ is the shape function vector computed at the center of the elements, and ΔT_j is the nodal temperature change vector in the j-th element. In addition, $\rho^{\text{3D}}\psi_j^{\text{3D}}$ is the free energy per unit length of the 3D model computed at the center of the bead section corresponding to the j-th element of the *QuadWire* mesh.

Nodal displacements in each element j are involved in (E.2), which is uneasy to use for the minimization procedure as the mechanical equation (D.48) involves the assembled nodal displacement $[U]_{\text{dof}}$ instead. Since independent beads are considered for the optimization (i.e., there are no kinematic relations between nodes of different beads) one can consider the matrix L_j relating nodal displacements in each element j and nodal displacements $[U]_{\text{dof}}$ in the entire domain so that for all j (with $1 \leq j \leq N_{\text{e}}$):

$$U_j = L_j\ [U]_{\text{dof}} \tag{E.5}$$

Hence the objective function rewrites as follows:

$$J(p) = \frac{1}{2}\sum_{j=1}^{N_{\text{e}}} l_j\ \left(\frac{1}{2}\,[U]_{\text{dof}}{}^\top\,L_j{}^\top\,K_j^0(p)\,L_j\ [U]_{\text{dof}} - [U]_{\text{dof}}{}^\top\,L_j{}^\top\,f_j^0(p) - \rho^{\text{3D}}\psi_j^{\text{3D}}\right)^2 \tag{E.6}$$

A gradient-based algorithm is used to solve the minimization problem (63). To do so, an adjoint problem is derived to compute the gradient composed of $\partial J(p)/\partial p_m$ with $1 \leq m \leq 24$. Consider the following Lagrangian:

$$\begin{aligned}\mathcal{L}\left(Q,y,p\right) &= \frac{1}{2}\sum_{j=1}^{N_\mathrm{e}} l_j \left(\frac{1}{2}\,Q^\top\,{L_j}^\top\,K_j^0(p)\,L_j\,Q - Q^\top\,{L_j}^\top\,f_j^0(p) - \rho^{3\mathrm{D}}\,\psi_j^{3\mathrm{D}}\right)^2 \\ &+ y^\top\left(\left[K\right](p)\,Q - \left[f\right]_{\mathrm{dof}}(p)\right)\end{aligned} \tag{E.7}$$

where Q is a dummy variable (which at optimality is equal to $[U]_{\mathrm{dof}}$), and y is the Lagrange multiplier or adjoint variable. The adjoint equation consists in finding a specific adjoint state $y^\dagger$ such as:

$$\frac{\partial \mathcal{L}}{\partial Q}\left(\left[U\right]_{\mathrm{dof}}, y^\dagger, p\right) = 0 \tag{E.8}$$

The adjoint equation therefore reduces to:

$$\left[K\right](p)^\top\,y^\dagger = -\sum_{j=1}^{N_\mathrm{e}} l_j\,\left(L_j{}^\top\,K_i^0(p)\,L_j\,\left[U\right]_{\mathrm{dof}} - L_j{}^\top\,f_j^0(p)\right)\,\lambda_j(p) \tag{E.9}$$

where the scalar coefficients $\lambda_j(p)$ read:

$$\lambda_j(p) = \frac{1}{2}\,{\left[U\right]_{\mathrm{dof}}}^\top\,{L_j}^\top\,K_j^0(p)\,L_j\,\left[U\right]_{\mathrm{dof}} - {\left[U\right]_{\mathrm{dof}}}^\top\,{L_j}^\top\,f_j^0(p) - \rho^{3\mathrm{D}}\,\psi_j^{3\mathrm{D}} \tag{E.10}$$

Considering $y^\dagger$ the solution of the adjoint problem (E.9) one obtains the successive derivatives of the objective function for $1 \leq m \leq 24$:

$$\begin{aligned}\frac{\partial J(p)}{\partial p_m} &= \sum_{j=1}^{N_\mathrm{e}} l_j\,\lambda_j(p)\left(\frac{1}{2}\,{\left[U\right]_{\mathrm{dof}}}^\top\,{L_j}^\top\,\frac{\partial K_j^0(p)}{\partial p_m}\,L_j\,\left[U\right]_{\mathrm{dof}} - {\left[U\right]_{\mathrm{dof}}}^\top\,{L_j}^\top\,\frac{\partial f_j^0(p)}{\partial p_m}\right) \\ &+ {y^\dagger}^\top\left(\frac{\partial\left[K\right](p)}{\partial p_m}\,\left[U\right]_{\mathrm{dof}} - \frac{\partial\left[f\right]_{\mathrm{dof}}(p)}{\partial p_m}\right)\end{aligned} \tag{E.11}$$

The application of (E.11) only necessitates to compute $\partial R^\xi(p)/\partial p_m$ and $\partial R^\chi(p)/\partial p_m$ which is obvious as p are the non-zero components of R^ξ and R^χ.

References

[1] A. Vasinonta, J. L. Beuth, M. Griffith, Process maps for predicting residual stress and melt pool size in the laser-based fabrication of thin-walled structures (2007).

[2] D. Weisz-Patrault, Fast simulation of temperature and phase transitions in directed energy deposition additive manufacturing, Additive Manufacturing 31 (2020) 100990.

[3] A. Edwards, D. Weisz-Patrault, E. Charkaluk, Analysis and fast modelling of microstructures in duplex stainless steel formed by directed energy deposition additive manufacturing, Additive Manufacturing 61 (2023) 103300.

[4] A. A. Rosli, R. K. Shuib, K. M. K. Ishak, Z. A. A. Hamid, M. K. Abdullah, A. Rusli, Influence of bed temperature on warpage, shrinkage and density of various acrylonitrile butadiene styrene (abs) parts from fused deposition modelling (fdm), in: AIP Conference Proceedings, volume 2267, AIP Publishing.

[5] G. Moelich, P. Kruger, R. Combrinck, A plastic shrinkage cracking risk model for 3d printed concrete exposed to different environments, Cement and Concrete Composites 130 (2022) 104516.
[6] E. R. Denlinger, M. Gouge, J. Irwin, P. Michaleris, Thermomechanical model development and in situ experimental validation of the laser powder-bed fusion process, Additive Manufacturing 16 (2017) 73–80.
[7] M. Biegler, B. Graf, M. Rethmeier, In-situ distortions in lmd additive manufacturing walls can be measured with digital image correlation and predicted using numerical simulations, Additive Manufacturing 20 (2018) 101–110.
[8] M. Boissier, G. Allaire, C. Tournier, Additive manufacturing scanning paths optimization using shape optimization tools, Structural and Multidisciplinary Optimization 61 (2020) 2437–2466.
[9] G. Allaire, L. Jakabčin, Taking into account thermal residual stresses in topology optimization of structures built by additive manufacturing, Mathematical Models and Methods in Applied Sciences 28 (2018) 2313–2366.
[10] Q. Chen, J. Liu, X. Liang, A. C. To, A level-set based continuous scanning path optimization method for reducing residual stress and deformation in metal additive manufacturing, Computer Methods in Applied Mechanics and Engineering 360 (2020) 112719.
[11] D. Weisz-Patrault, P. Margerit, A. Constantinescu, Residual stresses in thin walled-structures manufactured by directed energy deposition: In-situ measurements, fast thermo-mechanical simulation and buckling, Additive Manufacturing 56 (2022) 102903.
[12] P. Michaleris, Modeling metal deposition in heat transfer analyses of additive manufacturing processes, Finite Elements in Analysis and Design 86 (2014) 51–60.
[13] E. Neiva, S. Badia, A. F. Martín, M. Chiumenti, A scalable parallel finite element framework for growing geometries. application to metal additive manufacturing, International Journal for Numerical Methods in Engineering 119 (2019) 1098–1125.
[14] A. Özcan, S. Kollmannsberger, J. Jomo, E. Rank, Residual stresses in metal deposition modeling: discretizations of higher order, Computers & Mathematics with Applications 78 (2019) 2247–2266.
[15] S. D. Proell, W. A. Wall, C. Meier, A simple yet consistent constitutive law and mortar-based layer coupling schemes for thermomechanical macroscale simulations of metal additive manufacturing processes, Advanced Modeling and Simulation in Engineering Sciences 8 (2021) 24.
[16] S. Gaudez, D. Weisz-Patrault, K. A. Abdesselam, H. Gharbi, V. Honkimäki, S. van Petegem, M. V. Upadhyay, On the accuracy of temperature estimates from in operando x-ray diffraction measurements during additive manufacturing (2023).
[17] Y. Ueda, K. Fukuda, M. Tanigawa, New measuring method of 3-dimensional residual stresses based on theory of inherent strain, Journal of the Society of Naval Architects of Japan 1979 (1979) 203–211.
[18] L. Zhang, P. Michaleris, P. Marugabandhu, Evaluation of applied plastic strain methods for welding distortion prediction (2007).
[19] N. Keller, V. Ploshikhin, New method for fast predictions on residual stress and distortion of am parts, in: 2014 International Solid Freeform Fabrication Symposium, University of Texas at Austin.
[20] X. Liang, L. Cheng, Q. Chen, Q. Yang, A. C. To, A modified method for estimating inherent strains from detailed process simulation for fast residual distortion prediction of single-walled structures fabricated by directed energy deposition, Additive Manufacturing 23 (2018) 471–486.
[21] I. Setien, M. Chiumenti, S. van der Veen, M. San Sebastian, F. Garciandía, A. Echeverría, Empirical methodology to determine inherent strains in additive manufacturing, Computers & Mathematics with Applications 78 (2019) 2282–2295.
[22] C. Ghnatios, K. E. Rai, N. Hascoet, P.-A. Pires, J.-L. Duval, J. Lambarri, J.-Y. Hascoet, F. Chinesta, Reduced order modeling of selective laser melting: from calibration to parametric part distortion, International Journal of Material Forming 14 (2021) 973–986.
[23] M. Bellet, J. K. Tematio, Y. Zhang, The inherent strain method for additive manufacturing: critical analysis and new inherent strain rate method, in: IOP Conference Series: Materials Science and Engineering, volume 1281, IOP Publishing, p. 012001.
[24] M. A. Biot, General theory of three-dimensional consolidation, Journal of applied physics 12 (1941) 155–164.
[25] T. Naciri, A. Ehrlacher, A. Chabot, Interlaminar stress analysis with a new multiparticle modelization of multilayered materials (m4), Composites Science and Technology 58 (1998) 337–343.

[26] S. Forest, R. Sievert, Elastoviscoplastic constitutive frameworks for generalized continua, Acta Mechanica 160 (2003) 71–111.
[27] B. Halphen, Q. S. Nguyen, Sur les matériaux standard généralisés, Journal de mécanique 14 (1975) 39–63.
[28] P. Suquet, Q. Nguyen, P. Germain, Continuum thermodynamics, J. Appl. Mech 50 (1983) 101–1020.
[29] G. Van Rossum, F. L. Drake Jr, Python reference manual, Centrum voor Wiskunde en Informatica Amsterdam, 1995.
[30] R. Viano, P. Margerit, L. Preumont, D. Weisz-Patrault, QuadWire-Elastic (https://doi.org/10.5281/zenodo.10822309), Zenodo, 2024.
[31] P. C. Hansen, D. P. O'Leary, The use of the L-curve in the regularization of discrete ill-posed problems, SIAM J. Sci. Comput. 14 (1993) 1487–1503.
[32] Q. Zhu, K. Yu, H. Li, Q. Zhang, D. Tu, Rapid residual stress prediction and feedback control during fused deposition modeling of pla, The International Journal of Advanced Manufacturing Technology (2022) 1–12.